MAX-PLANCK-INSTITUT FÜR KOLLOID- UND GRENZFLÄCHENFORSCHUNG

Cesium-Mediated Porous Carbon Synthesis For Capacitive Energy Storage

Dissertation
zur Erlangung des akademischen Grades
doktor rerum naturalium
(Dr. rer. nat.)
im Fach Chemie
Physikalische und Theoretische Chemie

eingereicht an der
Mathematisch-Naturwissenschaftlichen Fakultät
Humboldt-Universität zu Berlin von
Jiaxin Li

Präsidentin der Humboldt-Universität zu Berlin
Prof. Dr. Julia von Blumenthal
Dekanin der Mathematisch-Naturwissenschaftlichen Fakultät
Prof. Dr. Caren Tischendorf

Gutachter/innen:

1. Prof. Dr. Philipp Adelhelm
2. Prof. Dr. Markus Antonietti
3. Prof. Dr. Nicola Pinna

Eingereicht am: 30.04.2024
Tag der mündlichen Prüfung: 03.07.2024

Contents

Abstract

Porous carbons are pivotal in capacitive energy storage, owing to their large surface area, tunable pore size, adjustable composition, high conductivity, and decent stability. Facile synthesis of high surface-area porous carbons with high yield is crucial for large-scale applications. Common methods involving activation and templating strategies are unsatisfactory due to the use of harsh chemicals and complex steps. An alternative approach, self-templating *via* direct pyrolysis of metallic organic salts, offers a facile strategy yielding porous carbons. However, the method often encounters low yields ($< 4\%$) and limited specific surface areas (< 2000 $m^2 \cdot g^{-1}$), attributed to low activity of metal cations (*e.g.,* K^+ or Na^+) in promoting the construction and activation of carbon frameworks. To tackle this problem, this thesis demonstrates huge potential of cesium (Cs) salts of carboxylic acids as self-templating precursors to simultaneously boost yield and surface areas of porous carbons and their significant applications in capacitive energy storage (**Chapter 1**).

Cesium acetate as a self-templating precursor for highly porous carbons. The simplest organic cesium salt, cesium acetate, is used as the sole self-templating precursor, producing porous carbons featuring high specific surface areas (1000−3000 $m^2 \cdot g^{-1}$), multiscale pore structures, pore volume approaching 2 $cm^3 \cdot g^{-1}$, and adjustable oxygen level (7−12 wt%), through the pyrolysis between 500 and 800 ºC. The unique role of cesium acetate is revealed as a carbon/oxygen source, physical template, and activating agent during the whole process. Finally, the resulting porous carbons showcase significant roles as CO_2 adsorbents and electrodes in supercapacitors (**Chapter 2**).

Cesium carboxylates as precursors for high-yield synthesis of highly porous carbons. Through the rational structural design of self-templating precursors, the carbon yields are increased to 25% while keeping high surface areas of around 3000 $m^2 \cdot g^{-1}$. Importantly, we shed light on the unconventional role of Cs species, which act as efficient electron injection and activating agents throughout the framework formation and pore development of carbon materials. Instead of a conventional etching process, Cs ion intercalation is identified as the primary activation mechanism for pore formation. The final porous carbons demonstrate significant roles as cathodes in both aqueous Zn-ion capacitors and aprotic Na-ion capacitors, showing high capacity and cycling stability (**Chapter 3**).

Rational design of porous carbons for Zn-ion capacitor cathodes. Uric acid is used as a mesopore enhancer of cesium acetate-derived carbons. By adjusting the mass ratio of uric acid and cesium acetate, porous carbons are obtained with varying pore sizes while maintaining comparable compositions and surface areas. Using these micro-mesoporous carbons as model materials allows for a systematic investigation into the impact of pore size on the electrochemical properties of Zn-ion capacitors. Supermicropores are identified as important for high capacity, while mesopores lead to good rate performance and cycling stability. Further comprehensive electrochemical analyses shed light on the charge storage mechanism of aqueous Zn-ion capacitors (**Chapter 4**).

Overall, this thesis will serve as an example of how a less explored element, Cs, can revolutionize conventional carbon science, leading to a facile synthetic process, low synthesis temperature, high carbon yield, large surface areas, and tunable porosities. The ease of synthesis and the diversity of carbon structures will bring new insights into carbon science, and unlock a multitude of application possibilities. Possible research directions are also presented, such as the investigation of synthetic mechanisms by advanced characterizations and the explorations of extensive metal species in porous carbon synthesis (**Chapter 5**).

Zusammenfassung

Poröse Kohlenstoffe sind aufgrund ihrer großen Oberfläche, ihrer einstellbaren Porengröße, ihrer guten Leitfähigkeit, ihrer einstellbaren Zusammensetzung und ihrer guten Stabilität von zentraler Bedeutung für die kapazitive Energiespeicherung. Die einfache Synthese von porösen Kohlenstoffen mit großer Oberfläche und hoher Ausbeute ist für großtechnische Anwendungen entscheidend. Herkömmliche Aktivierungs- und Schablonierungsverfahren sind aufgrund des Einsatzes aggressiver Chemikalien und komplexer Schritte nicht zufriedenstellend. Ein alternativer Ansatz, die Selbst-Templating-Methode durch direkte Pyrolyse von metallorganischen Salzen, bietet eine einfache Strategie zur Herstellung poröser Kohlenstoffe. Bei dieser Methode werden jedoch häufig geringe Ausbeuten (< 4 %) und begrenzte spezifische Oberflächen (< 2000 m^2·g^{-1}) erzielt, was auf die geringe Aktivität von Metallkationen (z. B. K$^+$ oder Na$^+$) bei der Förderung des Aufbaus und der Aktivierung von Kohlenstoffgerüsten zurückzuführen ist. Um dieses Problem zu lösen, wird in dieser Arbeit das enorme Potenzial von Cäsium (Cs)-Salzen von Carbonsäuren als selbsttemplierende Vorstufen zur gleichzeitigen Steigerung der Ausbeute und der Oberflächen von porösen Kohlenstoffen und deren bedeutende Anwendungen in der kapazitiven Energiespeicherung aufgezeigt (**Kapitel 1**).

Cäsiumacetat als selbsttemplierender Vorläufer für hochporöse Kohlenstoffe. Das einfachste organische Cäsiumsalz, Cäsiumacetat, wird als einziger selbsttemplierende Vorläufer verwendet, um durch Pyrolyse zwischen 500 und 800 °C poröse Kohlenstoffe mit hohen SSAs (1000−3000 m^2·g^{-1}), multiskaligen Porenstrukturen, einem Porenvolumen von annähernd 2 cm^3·g^{-1} und einem einstellbaren Sauerstoffgehalt (7−12 Gew.-%) herzustellen. Die einzigartige Rolle von Cäsiumacetat wird als Kohlenstoff-/Sauerstoffquelle, physikalische Vorlage und Aktivierungsmittel während des gesamten Prozesses deutlich. Schließlich zeigen die resultierenden porösen Kohlenstoffe eine bedeutende Rolle als CO$_2$-Adsorber und Elektroden in Superkondensatoren (**Kapitel 2**).

Cäsiumcarboxylate als Vorläufer für die hocheffiziente Synthese von hochporösen Kohlenstoffen. Durch ein rationales Strukturdesign der selbsttemplierenden Vorläufer wird die Kohlenstoffausbeute auf 25% erhöht, wobei eine hohe Oberfläche von etwa 3000 m^2·g^{-1} erhalten bleibt. Wichtig ist, dass wir die unkonventionelle Rolle von Cs-Spezies beleuchten, die während

der Gerüstbildung und Porenentwicklung von Kohlenstoffmaterialien als effiziente Elektroneninjektoren und Aktivierungsmittel fungieren. Anstelle des konventionellen Ätzprozesses wird die Einlagerung von Cs-Ionen als der primäre Aktivierungsmechanismus für die Porenbildung identifiziert. Die fertigen porösen Kohlenstoffe spielen eine wichtige Rolle als Kathoden sowohl in wässrigen Zn-Ionen-Kondensatoren als auch in aprotischen Na-Ionen-Kondensatoren und weisen eine hohe Kapazität und Zyklenstabilität auf (**Kapitel 3**).

Rationales Design von porösen Kohlenstoffen für Kathoden von Zn-Ionen-Kondensatoren. Harnsäure wird als Mesoporenverstärker für Cäsiumacetat-abgeleitete Kohlenstoffe verwendet. Durch Anpassung des Massenverhältnisses von Harnsäure und Cäsiumacetat erhält man poröse Kohlenstoffe mit unterschiedlichen Porengrößen bei vergleichbarer Zusammensetzung und Oberfläche. Die Verwendung dieser mikro-mesoporösen Kohlenstoffe als Modellmaterialien ermöglicht eine systematische Untersuchung der Auswirkungen der Porengröße auf die elektrochemische Leistung von Zn-Ionen-Kondensatoren. Es wurde festgestellt, dass Supermikroporen für eine hohe Kapazität wichtig sind, während Mesoporen zu einer höheren Leistung und Zyklenstabilität führen. Weitere umfassende elektrochemische Analysen geben Aufschluss über die Ladungsspeichermechanismen von wässrigen Zn-Ionen-Kondensatoren (**Kapitel 4**).

Insgesamt dient diese Arbeit als Beispiel dafür, wie ein weniger erforschtes Element, nämlich Cs, die konventionelle Kohlenstoffwissenschaft revolutionieren kann, indem es zu einem einfachen Syntheseverfahren, niedrigeren Synthesetemperaturen, großen Oberflächen und einstellbaren Porositäten führt. Die Einfachheit der Synthese und die Vielfalt der Kohlenstoffstrukturen werden neue Erkenntnisse über die Kohlenstoffsynthese bringen und eine Vielzahl von Anwendungsmöglichkeiten eröffnen. Es werden auch mögliche Forschungsrichtungen vorgestellt, wie z. B. die Untersuchung des Synthesemechanismus durch fortgeschrittene Charakterisierungen und die Erforschung umfangreicher Metallspezies in der porösen Kohlenstoffsynthese (**Kapitel 5**).

Chapter 1 Introduction to porous carbons for capacitive energy storage

1.1 Overview

Carbon is a unique element due to its versatile bonding capabilities by different orbital hybridizations (sp, sp^2, and sp^3), allowing for the formation of diverse carbon allotropes with distinct structures and properties. The most well-known carbon allotropes include diamond,[1] graphite,[2] fullerene,[3] graphene,[4] carbon nanotube,[5] hard carbon,[6,7] and amorphous porous carbon[8,9] (***Figure 1.1***). Recent discoveries, such as graphdiyne[10,11] and the covalent network of fullerenes,[12,13] have further expanded the range of known carbon allotropes. In addition, carbon atoms can also bond with other atoms with similar or very different electronegativity, most notably hydrogen, boron, nitrogen, oxygen, phosphorus, and sulfur, forming a majority of organic compounds. The introduction of heteroatoms into carbon structures alters the electronic structures and functional properties of carbon materials.[14] Further, the functionalization of carbon materials can be expanded by incorporating metal species, unlocking new possibilities for their applications.

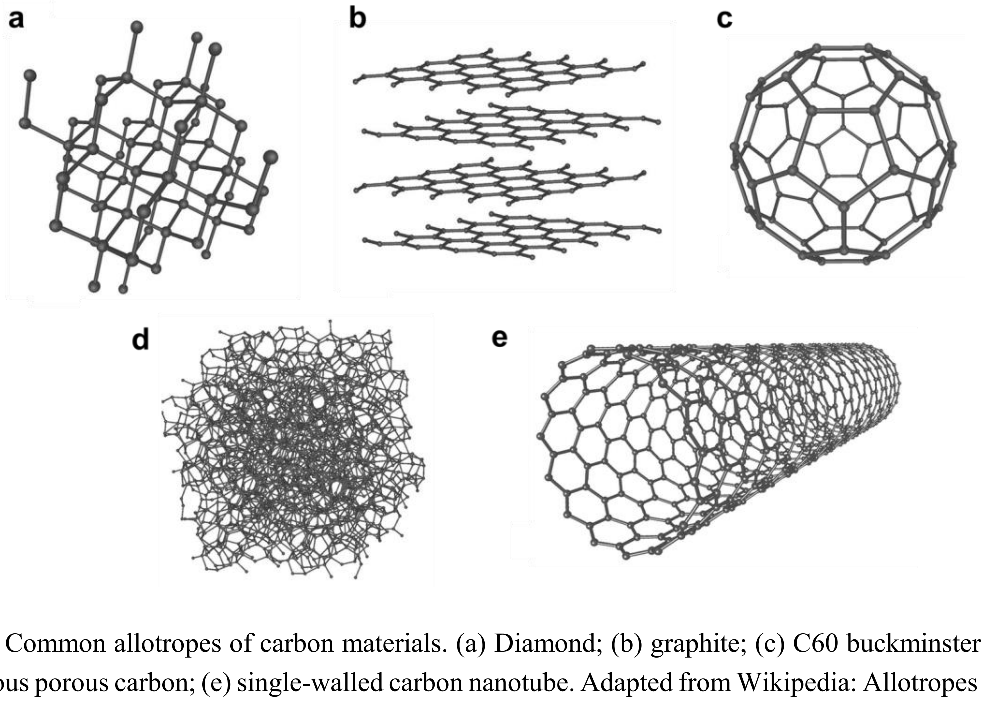

Figure 1.1. Common allotropes of carbon materials. (a) Diamond; (b) graphite; (c) C60 buckminsterfullerene; (d) amorphous porous carbon; (e) single-walled carbon nanotube. Adapted from Wikipedia: Allotropes of carbon.

Carbon materials have fundamentally revolutionized materials science and now play a vital role in various fields of modern society, such as energy storage and conversion, sensing, and information technology,[15–20] benefiting from their diverse structures and tunable properties. Among the big carbon family, amorphous porous carbon materials stand out as an important sp^2-rich carbon allotrope with large specific surface area (SSA), tunable porosity, rich surface chemistry, decent stability, and facile synthesis. They have exhibited diverse applications in gas storage/separation, water/air treatment, sensing, and energy storage and conversion. In particular, porous carbons occupy a key position in electrochemical energy storage, serving as electrodes in supercapacitors,[21,22] hybrid metal-ion capacitors,[23–25] metal-air batteries, metal-ion batteries,[7,26] metal-sulfur batteries,[27,28] and emerging novel devices.[29]

To this end, various synthetic strategies have been proposed, in which metal-based chemicals have a significant impact on the establishment of covalent networks and the formation of pore structures. Controlled synthesis of porous carbonaceous materials with desired structures and properties is constantly pursued and requires further innovation in carbon synthesis strategies. Besides, the rational design of porosities and compositions of porous carbons is also crucial to achieving high-performance energy storage devices and helping understand energy storage mechanisms.

1.2 Synthesis strategies of porous carbons

The unique properties of porous carbons are linked with their nanoporous structures. Generally, nanopores are classified into three categories according to their pore sizes: micropores (pore width < 2 nm), mesopores (pore width of 2–50 nm), and macropores (pore width > 50 nm) based on the International Union of Pure and Applied Chemistry (IUPAC) definition.[30] Many synthetic strategies have been proposed to introduce pores into porous carbon networks, most notably activation and templating approaches.[31]

1.2.1 Activation

The activation strategies include physical and chemical activation strategies, typically yielding microporous carbon materials with high porosity and large specific surface area (named activated carbon) and used as adsorbents in gaseous or liquid adsorption.[32] The most common carbon sources of activated carbon on a commercial scale include wood, anthracite bitumen charcoal, lignite, peat shells, and coconut shells. Physical activation is a two-step process involving the pyrolysis of carbon precursors in an inert atmosphere, followed by activation in oxidizing gases like CO_2 and H_2O within a temperature range of 800–1100 °C. It is worth mentioning that the physical activation also relies on the chemical etching process to create pores in the carbon structure. Chemical activation, on the other hand, involves the reaction between carbon and chemical reagents (*e.g.,* KOH, NaOH, H_3PO_4, or $ZnCl_2$) at a temperature range of 400 to 900 °C. In chemical activation, a large amount of chemical activation agents is mixed with carbon precursors or carbon, and these agents etch the carbon materials at high temperatures. Chemical activation offers several advantages over physical activation, including the ability to operate at lower temperatures, shorter processing times, and higher carbon efficiency. However, one drawback of chemical activation is the need for repeated washings to remove activators, which could potentially cause pollution.

1.2.2 Templating

While the activation strategy can introduce abundant pores into carbon networks, it often gives low carbon yields due to pore creation at the expense of carbon atoms (etching). In contrast, the templating method creates pore structures without sacrificing carbon yields, by using various templating agents (structure-directing agents) during carbonization,[33,34] such as hard templates, soft templates, or salt templates to exert precise control over pore structures. This strategy often leads to ordered and uniform nanostructures, which cannot be achieved by activation methods.

The **hard-templating** route is a direct approach involving the creation of pore structures from presynthesized hard templates, such as anodic alumina, silica colloidal crystals, and zeolites.[34,35] This method included the following steps: (a) synthesis of templating agents with controlled pore structures, (b) infiltration of templates with carbon precursors through wet impregnation, melt-infiltration, or chemical vapor deposition, (c) crosslinking and carbonization of the organic precursors within the confined nanospace of templating agent (*e.g.,* 1D channels, 2D space, or 3D connected pores), and (d) removal of the templating agent (typically by hydrofluoric acid) (***Figure 1.2a***). The resulting carbon materials inherit the shape and size of nanospace occupied by the host templates. The structure and connectivity of generated pores can be adjusted by the structures of the applied templates.

The **soft-templating method** relies on the self-assembly of micelles of surfactants or amphiphilic block co-polymers as templates (organic directing agents) for the generation of porous structures, mostly driven by van-der-Waals and Coulomb interaction forces, followed by stabilization of precursor framework by polymerization and carbonization of polymer precursors to produce ordered mesoporous carbons (***Figure 1.2b***).[36,37] The morphology and size of mesopores are adjustable by controlling the size, composition, and concentration of templating agents or the composition or polymerization degree of precursor. In most cases, the soft templating strategies result in meso- or macroporosity but few micropores and limited surface areas. Compared to the hard templating strategy, the soft templating strategy eliminates the presynthesis of mesoporous silica template and the template removal using NaOH or hydrogen fluoride solution. However, it still suffers from several disadvantages including complex multistep processes, low self-assembly rate, and less choice of raw materials and final products.

In 2013, the Antonietti group first proposed a **salt-templating** strategy using eutectic mixtures of $ZnCl_2$ and alkali metal halides as solvents and templating agents.[38] The salt-templating method generally involves three simple steps: (a) mixing salts and carbon precursors in a mass ratio of 1−20, (b) carbonizing the mixture at temperatures between 400 and 1000 °C in Ar or N_2, and (c) removing salts by water or diluted acid (***Figure 1.2c***). Metal halides are the most commonly used molten salts (such as $LiCl/ZnCl_2$, $NaCl/ZnCl_2$, and $KCl/ZnCl_2$) due to their low melting points, high stability, reusability, and good solubility for carbon precursors. The melting points of salts (***Table 1.1***) should be lower than the onset of crosslinking of precursor to ensure the complete dissolution of precursors in the salts and the formation of homogeneous carbon products.

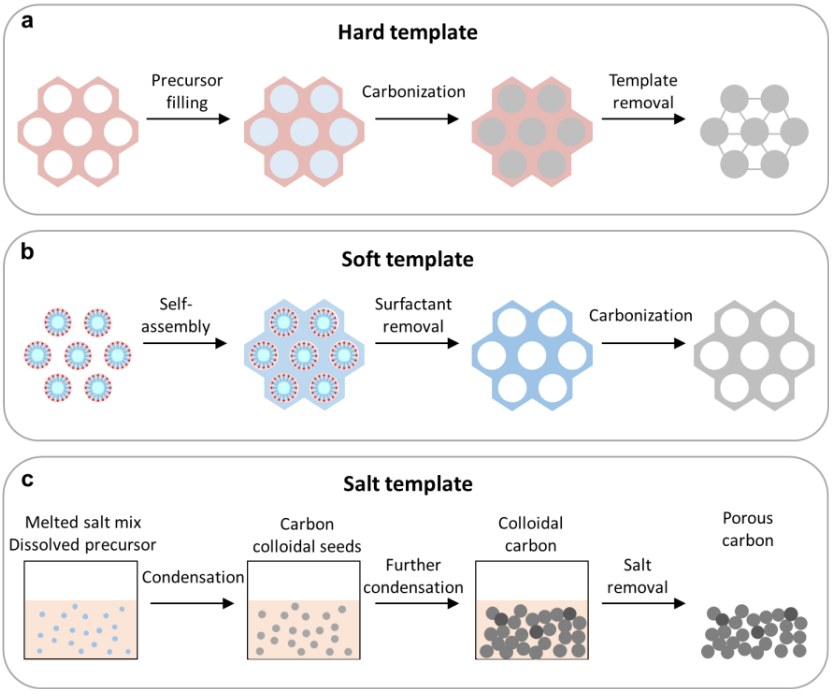

Figure 1.2. Schemes of synthetic process of porous carbons by (a) hard templating, (b) soft templating, and (c) salt-templating methods.

Table 1.1. Melting points (T_m) of metal chlorides and eutectic mixtures of two metal chlorides.

Salts	T_m (°C)	Eutectic salt mixtures	Molar ratio	T_m (°C)
$CaCl_2\cdot 6H_2O$	30	$SnCl_2/KCl$	0.50/0.50	180
$SnCl_2\cdot 2H_2O$	38	$ZnCl_2/KCl$	0.54/0.46	230
$MgCl_2\cdot 4H_2O$	115	$ZnCl_2/NaCl$	0.68/0.32	260
$MgCl_2\cdot 6H_2O$	117	$ZnCl_2/LiCl$	0.78/0.22	275
$CaCl_2\cdot 2H_2O$	175	$KCl/LiCl$	0.41/0.59	353
$MgCl_2\cdot 2H_2O$	167	$KCl/NaCl$	0.49/0.51	657
$SnCl_2$	247			
$CaCl_2\cdot H_2O$	260			
$ZnCl_2$	290			
$LiCl$	605			
$MgCl_2$	714			
KCl	770			
$CaCl_2$	772			
$NaCl$	801			

The salts act as a reaction medium and pore-forming agents during condensation. The pore formation is mainly based on a liquid templating process, where the pore size corresponds to the sizes of ion pairs, salt clusters, and their percolation structures. In the case of high salt-to-precursor mass ratios (> 10), the process can resemble a sol-gel synthesis, leading to aerogel-like carbons. Micropores are formed from ion pairs or nanosized salt clusters remaining within the carbon particles, and the interconnected meso-/macroporosity comes from the phase separation of the carbonizing phase from the molten salt phase. For low salt-precursor ratios, the dispersed salt droplets within a continuous carbon phase function as molecular templates for micropores, giving rise to microporous carbons.

Salt-templating strategies offer several advantages: (a) potential to use a wide range of carbon sources, such as ionic liquids, nucleobases, carbohydrates, or polymers, (b) easily controlled carbon structures by adjusting salt type, precursor, salt-to-precursor ratio, synthetic temperature, and additive, (c) high carbon yields (> 10 wt%) and high SSAs of 1000–3000 $m^2\cdot g^{-1}$, and (d) the possibility to introduce high content heteroatoms into carbon networks, such as N, S and B, in contrast to activation strategy that usually leads to the depletion of material functionalities.

1.2.3 Self-templating

The activation and templating strategies usually involve the use of harsh chemicals and time- and energy-consuming steps. Self-templating represents a simple and sustainable synthetic strategy to obtain porous carbons by direct pyrolysis of metal-containing organic precursors.

Metal-organic salt-derived carbon. K or Na citrates or carboxylates have shown potential as all-in-one self-templating precursors for porous carbon synthesis.[39–42] During heating, the organic species in these salts rapidly condense into the carbonaceous frameworks, and the *in situ* formed K or Na carbonates and oxides serve as *in situ* formed templates or etching agents for the formation of porous networks. However, the reported K or Na organic salts typically suffer from low carbon yields (< 4%) and limited SSAs (< 2000 $m^2 \cdot g^{-1}$). This is possible because K and Na salts exploited in these cases have a minor impact on the formation and activation of carbon networks.

Metal-organic framework-derived carbon. In recent years, metal-organic frameworks (MOFs), a kind of crystalline coordination compound comprising metal ions and organic ligands, have been used as templates or precursors for functional carbon materials synthesis.[43,44] In 2007, Xu and co-workers pioneered the use of furfuryl alcohol as a carbon precursor and MOF-5 as a template, resulting in nanoporous carbon with a high SSA of 2872 $m^2 \cdot g^{-1}$ at 1000 ºC in Ar atmosphere.[45] The predominant organic components of MOFs allow for the synthesis of carbon materials *via* direct pyrolysis of MOFs (***Figure 1.3***),[46,47] such as a commercially available zeolitic imidazolate framework (ZIF-8).

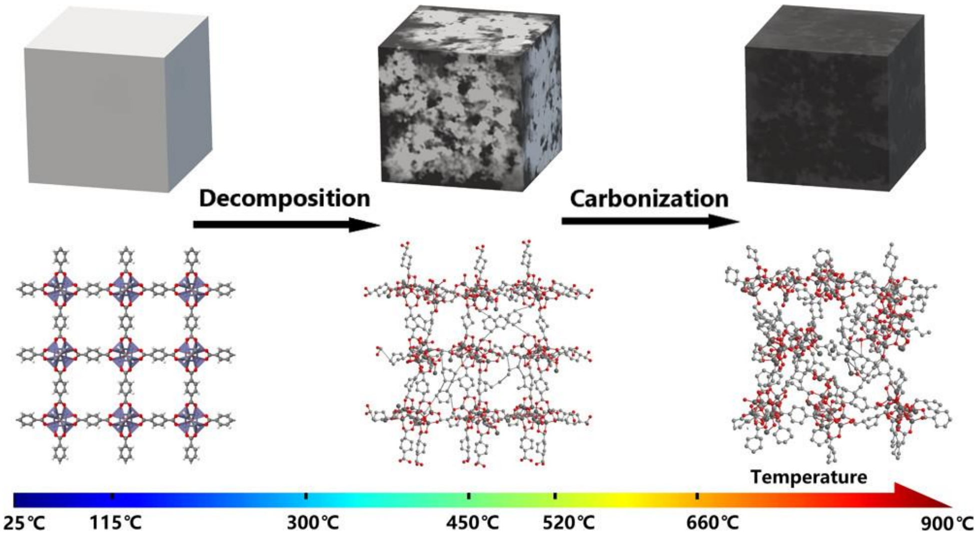

Figure 1.3. Scheme of the synthetic process of MOF-derived porous carbons. Request with permission.[46] Copyright 2018, ACS Publications.

The carbon materials could retain morphologies, pore networks, and heteroatoms like N, S, P, and B from MOF precursors. The structures and compositions of carbon materials are adjustable by varying metal ions and bridging ligands of MOFs or introducing additives. Despite the advantages in facile preparation and unique properties, it is essential to note that MOF-derived carbons face challenges of low yields since the typical metal ions like Zn cannot catalyze the condensation of organic species, giving low carbon yields. Meanwhile, the organic ligands of MOF are much more expensive, compared with biomass precursors, which largely increases production cost and hinders industrial applications of MOF-derived carbons.

Carbide-derived carbons (CDC) constitute a large family of carbon materials derived from carbide precursors, such as Al_4C_3, B_4C, BaC_2, CaC_2, Cr_3C_2, Fe_3C, Mo_2C, MoC, Nb_2C, NbC, SiC, SrC_2, Ta_2C, TaC, Ti_2AlC, Ti_3AlC_2, Ti_3SiC_2, TiC, VC, W_2C, WC, and ZrC.[48] CDC is produced through the selective extraction of metal or metalloid atoms from the carbide lattice by thermal decomposition or halogenation, leaving behind nanoporous carbons with a 50 to 80% open pore volume.[48] Chlorination is the most cost-effective and scalable method for CDC synthesis. Atomic-level pore control in CDC is achieved by exploiting the host carbide lattice as a template, permitting controlled layer-by-layer metal extraction by optimizing the chlorination parameters. Generally, CDCs have a narrow pore size distribution in the range of 0.5 to 3 nm and a SSA up to 2000 $m^2 \cdot g^{-1}$. This ease of tunability in narrow pore size allows for experimental determination of the optimal pore size for gas adsorption and energy storage applications.[49–51] Besides, CDC has a higher conductivity than activated carbons from organic precursors with similar SSA or pore structure owing to its lack of oxygen or hydrogen in its carbon network.

1.3 Metal species in porous carbon synthesis

1.3.1 The role of metal species

In the above synthetic methods, metal-based chemicals, including metallic hydroxides, carbonates, oxides, or halides, have been widely used and demonstrated significant influences on the structures of the final carbon materials. The specific roles encompass the following aspects.

1.3.1.1 Reaction medium

In the molten salt synthesis of porous carbon materials, the salts or multi-component salt systems initially serve as stable high-temperature reaction media for precursors, oligomers, and polymers. These salts provide higher temperatures (300–1000 ºC, ***Table 1.1***) than conventional liquid organic solvents (below 300 ºC). To serve as a reaction medium, these salt systems should exhibit lower melting points than the onset of pyrolysis/condensation of precursors, and negligible vapor pressure capable of withstanding carbonization temperatures. The carbon precursor dissolves in the salt melt before decomposition, and the miscibility between organic phase and salt phase should be maintained throughout the carbonization process. The progression of carbon source from the precursor to carbon is similar to a sol-gel process, where the molten salt acts as a reaction medium that prevents the collapse of polymeric/carbonaceous frameworks.

Eutectic mixtures of $ZnCl_2$ and alkali chlorides[38,52,53] or $SnCl_2$ with low melting points,[54,55] have been extensively explored for this purpose. With much lower melting points than their anhydrous salts, the hydrates of $MgCl_2$ and $CaCl_2$ also act as solvents for carbon precursors before they dehydrate and recrystallize.[56] The melting points of mixtures comprising the salt hydrates and carbon precursor can be further reduced due to the formation of deep eutectic mixtures. Compared with solid-state reactions, this liquid medium reaction allows for faster mass transfer, shorter reaction times, lower reaction temperatures, and precise temperature control for the synthetic process, facilitating easy adjustment of product properties. The salt also acts as a templating agent influencing the morphology and porosity of carbon materials, a topic to be discussed later.

1.3.1.2 Promote condensation

In the salt templating strategy, the presence of molten salts can prevent the sublimation, evaporation, and decomposition of small molecular precursors, stabilize reactive intermediates formed during the condensation process, and accelerate the crosslinking and condensation of organic species to form covalent networks. For example, pyrolysis of small organic molecules like adenine cannot yield any carbonaceous matter due to their high volatility at increased temperatures. The introduction of salt melt inhibits the evaporation of volatile species due to interactions between precursors and $ZnCl_2$ salts. Besides, $ZnCl_2$, $CaCl_2$, and $MgCl_2$ act as dehydrating agents, enhancing the crosslinking of molecular precursors for higher yields.

Some transition metals, such as Co, Fe, and Cr, can enhance the thermal stability of molecular precursors and assist the formation of thermally stable polymeric intermediates during carbonization, resulting in a higher carbon yield.[57] The authors believe that the transition metal ions with vacant d orbitals accept lone pair electrons of N atoms in molecular precursors, can enhance the thermal stability of organic molecules, and prevent their sublimation at relatively low temperatures. During carbonization, the molecular precursor could survive until the temperature of *ca.* 200 °C at which cobalt catalyzed the thermal transformation of the molecular precursor into a stable polymeric intermediate that finally was converted to carbon materials at high temperature. Recently, it has also been reported that Sn^{2+} can trigger reductive deoxygenation and concomitant condensation/cross-linking of oxo-carbon precursors due to the strong interaction between Sn^{2+} ions and oxygen, to be discussed more in the next section.[55]

1.3.1.3 Create pores

Metal-based chemicals have a significant impact on pore formation through etching, intercalation, or templating effects. Using metal hydroxides to etch the established carbonaceous matter is a well-recognized strategy to produce porous carbons with high surface areas and abundant micropores, attributed to a combination of physical activation, chemical activation (etching), and carbon lattice expansion by metallic K intercalation, to be discussed in detail later.

The use of metallic oxides or their precursors (*e.g.*, TiO_2, Al_2O_3, MgO, or CaO, ZnO) serve as templating agents to introduce mesoporous structures into carbon networks. Generally, these metal oxides are stable at the carbonization and activation temperatures (< 800 ºC) which cannot be reduced through carbothermal reduction reactions. The sizes and volumes of mesopores are adjustable by the selection of templating agents. Besides serving as hard templates, ZnO or MgO also etch carbon surfaces, increasing SSAs and microporous structures.

The use of a salt template has emerged as a sustainable strategy for synthesizing porous carbon. Beyond its role as solvent as discussed above, the ion pairs and salt clusters also act as effective molecular templates, influencing the size and volume of nanopore structures. The mesoporous carbons obtained from salt-melt synthesis often present disordered and connected pore structures. Additionally, some reactive salt melts, like nitrates, also increase the porosity in the carbonaceous matter.[57]

1.3.1.4 Catalyze graphitization

Carbons with a graphitic structure are valued due to their high thermal and electronic conductivity and chemical stability. Notably, certain transition metals, such as iron (Fe) and nickel (Ni), exhibit high catalytic efficiency in the structural transformation of amorphous carbon into well-ordered graphitic structures at lower temperatures (700−900 ºC) compared to traditional graphite synthesis (> 2000 ºC). Typically, the synthesis involves mixing an organic precursor (*e.g.,* small organic molecules, synthetic polymers, and biomass) with catalyst particles (*e.g.,* iron precursors such as ferrocene, iron nitrate, iron acetate or iron chloride) and pyrolyzing the mixtures in an inert atmosphere.[58] During the heating process, organic precursors condense forming amorphous carbon, while the iron precursor decomposes, initially forming iron oxide and subsequently transforming into iron or iron carbide by carbothermal reduction. These metal particles play a key role in driving the graphitization of amorphous carbon.

The mechanism behind catalytic graphitization remains debated. One proposed theory is dissolution-precipitation, where iron particles dissolve carbon atoms until reaching supersaturation, causing the precipitation of graphitic carbon from the particle.[59] This theory explains the high activity for graphitization observed in certain metals with high carbon solubility, such as iron and nickel. In many instances, the formation of tubular nanostructure suggests that catalyst particles move through the amorphous carbon matrix during graphitization, possibly driven by the dissolution and precipitation of carbon. An alternative hypothesis suggests that the crucial factor for graphitization lies in the formation of metastable carbides, which can decompose into more thermodynamically stable metal species and precipitate graphitic carbon.[60]

1.3.2 Specific examples

As demonstrated in the previous section, metal-based chemicals play multiple roles in porous carbon synthesis based on the activation and templating approaches, influencing the final structures of porous carbon materials. In this section, practical examples of metal-based chemicals are presented, shedding light on the fundamental physical and chemical mechanisms of their involvement in these processes.

1.3.2.1 Alkali metals

Alkali metal hydroxides, KOH in particular, are used as powerful activation agents to access porous carbons with ultrahigh surface areas (around 3000 $m^2 \cdot g^{-1}$) and narrow micropore size distributions.[61] The activation process can be carried out after or simultaneously with the carbonization process. In the formal case, non-porous carbon materials (char, cokes, or coals) are pre-synthesized by pre-carbonization of biomass in an inert atmosphere (Ar or N_2). Subsequently, KOH is mixed with carbonaceous matter with a mass ratio of 2−10 and subjected to treatment at temperatures of 600 to 950 °C. Alternatively, carbon precursors can be mixed directly with KOH for simultaneous carbonization and activation. Finally, all K species are removed by acidic solutions and water to obtain porous carbons.

This activation process involves many simultaneous or consecutive reactions, some of which are presented in ***Equation 1–9*** below.[62,63] At around 400 °C, KOH dehydrates and transforms into K_2O (***Equation 1***). The generated H_2O reacts with C, releasing H_2, CO, and CO_2 (***Equations 2*** and ***3***), while the generated CO_2 further reacts with KOH producing K_2CO_3. Complete consumption of KOH occurs at around 600 °C (***Equation 4***). Then the initially formed K_2CO_3 completely decomposes into K_2O and CO_2 at temperatures between 700 and 800 °C (***Equation 5***). At this temperature range, carbon is etched by CO_2 releasing CO (***Equation 6***), while K_2CO_3 and K_2O can be reduced by carbon to form metallic K at above 700 °C (***Equations 7*** and ***8***).

$$2KOH \rightarrow K_2O + H_2O\ (400\text{–}600\ ^{\circ}C) \tag{1}$$

$$C + H_2O \rightarrow CO + H_2\ (400\text{–}600\ ^{\circ}C) \tag{2}$$

$$CO + H_2O \rightarrow CO_2 + H_2\ (400\text{–}600\ ^{\circ}C) \tag{3}$$

$$K_2O + CO_2 \rightarrow K_2CO_3\ (400\text{–}600\ ^{\circ}C) \tag{4}$$

$$K_2CO_3 \rightarrow K_2O + CO_2\ (700\text{–}800\ ^{\circ}C) \tag{5}$$

$$CO_2 + C \rightarrow 2CO\ (700\text{–}800\ ^{\circ}C) \tag{6}$$

$$K_2CO_3 + 2C \rightarrow 2K + 3CO\ (> 700\ ^{\circ}C) \tag{7}$$

$$K_2O + C \rightarrow 2K + CO\ (> 700\ ^{\circ}C) \tag{8}$$

The development of large surface areas and high microporosity in carbon is a result of synergistic effects, including (a) chemical activation: etching of carbon frameworks through redox reactions between K species (carbonate or oxide) and carbon, as illustrated in ***Figure 1.4*** and described by ***Equation 5***; (b) physical activation: the formation of CO_2 and H_2O contributes to the development of porosity, as shown in ***Equation 2*** and ***6***; (c) metallic K intercalation: the formation of K metal above 700 °C inserts into the graphitic layers of carbon matrix, opening slit pores. The actual activation mechanism is complex, influenced by multiple variables, including the selection of carbon precursors and experimental parameters (temperature, KOH/precursor ratio). The overall behavior of NaOH and KOH is similar, but the activation of NaOH requires higher temperatures (> 600 °C) and produces lower porosity than KOH.[63] Recently, CsOH has proved to be an even most powerful activation agent, leading to larger volume expansion and higher SSAs of carbon materials than those from K. This was linked with a lower formation energy of Cs graphite intercalation compound than K and a lower melting point of Cs_2O (490 ºC) than K_2O (740 ºC).[64]

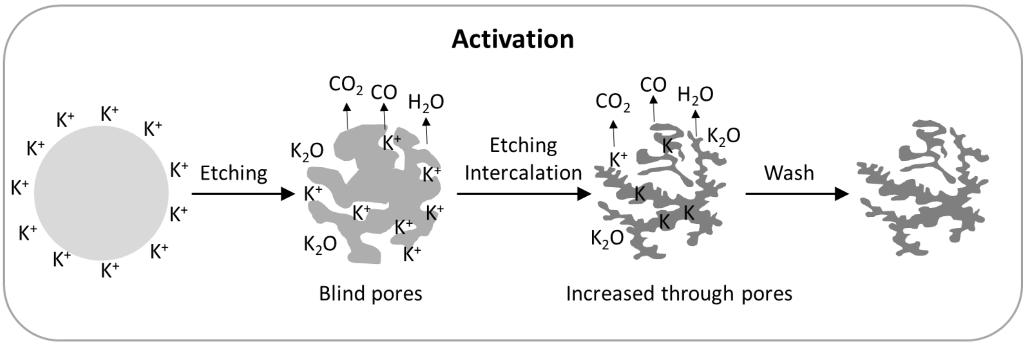

Figure 1.4. Scheme of the synthetic process of activated carbon by KOH etching.

As discussed earlier, the mixtures of **alkali metal chlorides** and $ZnCl_2$ have been widely used in the synthesis of porous carbons since the melting points of single salts (LiCl, NaCl, or KCl) are also too high to act as solvents and porogens. These salt mixtures have lower melting points (230-275 ºC) than $ZnCl_2$ (290 ºC), being favorable for dissolution and condensation of molecular precursors in the liquid medium. Further, the selection of alkali ions can influence the morphology and pore structure of final carbon materials (***Figure 1.5a***).[38] For example, when using ionic liquids as the precursor, the eutectic mixture $LiCl/ZnCl_2$ results in microporous carbons (SSA of 1200–1700 $m^2 \cdot g^{-1}$, V_{N2}=0.6–2.75 $cm^3 \cdot g^{-1}$), implying the role of salt as molecular template (ion pairs or little salt clusters). In comparison, $NaCl/ZnCl_2$ gives the product with supermicropores and small mesopores (SSA of 1400–1700 $m^2 \cdot g^{-1}$, V_{N2}=0.6–2.07 $cm^3 \cdot g^{-1}$), indicating larger salt clusters as templates during condensation. Macroporous carbon with spherical morphology and interstitial pores are obtained when $KCl/ZnCl_2$ is used (SSA of 1100–1800 $m^2 \cdot g^{-1}$, V_{N2}=0.56–1.70 $cm^3 \cdot g^{-1}$). These different pore structures/morphologies were linked to the different melting temperatures of the eutectic mixtures. The lower the melting temperature, the more pronounced demixing occurs in earlier phases of the condensation reactions, leading to bigger salt clusters or even continuous salt as templates for larger pore sizes.

Changing the ratio of alkali salt and $ZnCl_2$ can tune the morphology, pore structure, or even composition of carbon materials. A small excess of alkali metal chloride over the eutectic mixture causes the demixing of the carbonizing phase and salt phase and enlarges the formed carbon nanopores. At a large excess, solid particles of alkali metal chloride, coexisting with the molten salt, act as hard templates for macropores. For instance, pyrolysis of adenine (molecular precursor) in an eutectic NaCl/$ZnCl_2$ mixture (33 mol% NaCl) produces a micro- and mesoporous carbon with a high SSA of 2900 $m^2 \cdot g^{-1}$ and a pore volume of 3.0 $cm^3 \cdot g^{-1}$ (***Figure 1.5b***).[65] Increasing NaCl content from 33 mol% to 80 mol% enlarges the nanopores, giving more large mesopores and new macropores. Meantime, the pore volume increases and achieves the maximum value of 5.2 $cm^3 \cdot g^{-1}$ at 60 mol% of NaCl while the SSA decreases from 3000 to 1750 $m^2 \cdot g^{-1}$. With 50–80 mol% of NaCl, the undissolved NaCl particles act as a hard template to create macropores. The nitrogen content, determined by combustion analysis, follows an opposite trend to the total pore volume. This is ascribed to increased decomposition of N species in an open pore system. Similarly, using glucose as a model precursor, the increase in KCl content in the KCl/$ZnCl_2$ eutectic mixture (KCl: 42 mol%) gives larger pores, rising pore volume, and a decrease of SSA from 2160 to 960 $m^2 \cdot g^{-1}$ from the hard templating effect of solid KCl.[66]

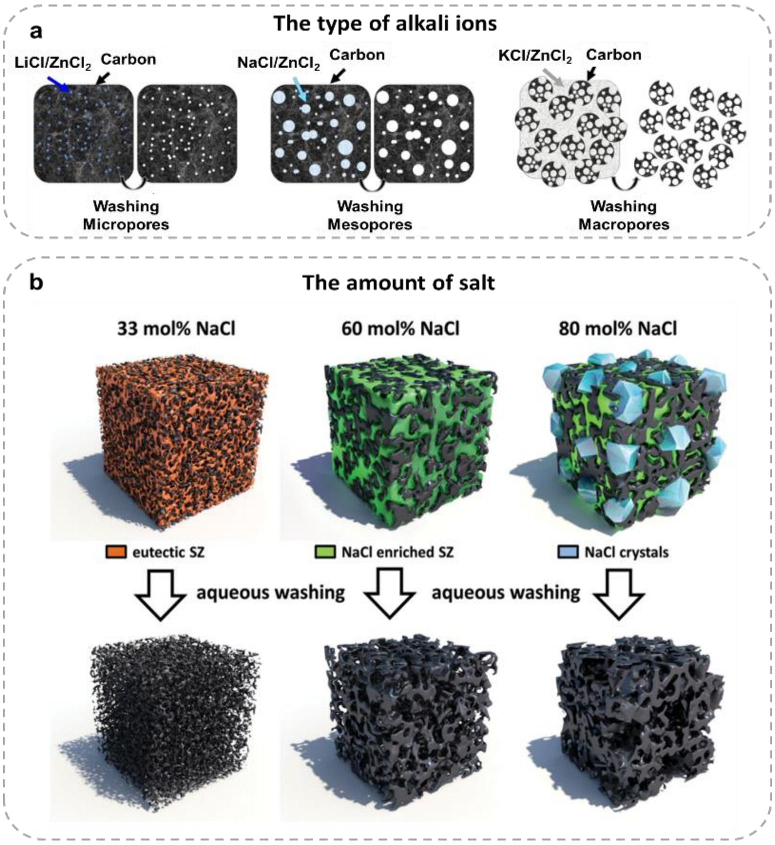

Figure 1.5. Schematic illustration of the influences of (a) types and (b) amounts of alkali salts on the porous carbon structure. Reproduced with permission from Ref.[38, 65] Copyright 2013 and 2016, WILEY-VCH.

The eutectic mixtures of KCl/LiCl (KCl: 41 mol%, T_m=353 °C) and KCl/NaCl (KCl: 49 mol%, T_m=657 °C) have also been used in the porous carbon synthesis despite their higher melting points compared to the onset of decomposition of molecular precursors. When using KCl/LiCl mixture, the carbon materials typically exhibit the morphology of nanosheets from various carbon precursors instead of colloidal particles observed in the low-melting-point salt melt synthesis. Introducing a mixture of sugar and $LiNO_3/K_2SO_4$ into KCl/LiCl salt mixture produces highly porous N- or S- doped carbons. In this process, KCl/LiCl serves as a chemically inert solvent, diluting the concentration of reactive salts to prevent explosions.[57] Using a KCl/NaCl mixture with a higher melting point serves as a hard template, yielding sponge-like carbons with large pores below 657 °C. Additionally, these salts function as a sealing layer for the formed carbonaceous matter to hinder the release of organic volatiles and favor self-activation reactions between CO_2 and carbon.

1.3.2.2 Alkali earth metals

Alkali earth metal oxides, such as MgO and CaO, function as templating agents in the synthesis of porous carbons.[67] Apart from MgO itself, various Mg-containing compounds like Mg acetate, Mg citrate, Mg gluconate, Mg hydroxyl-carbonate, or $Mg(NO_3)_2$ can be used as MgO precursors.[68] The pyrolysis of these Mg-containing compounds leads to the formation of nano-sized MgO within the carbon matrix at around 600 °C. The use of MgO as a template offers remarkable advantages: (a) the size and volume of pores in the resulting carbons can be adjusted by selecting Mg-containing starting materials and precursors, and (b) the template MgO can be easily removed by a diluted acid.[68] These carbons exhibit a rich mesopore structure with high surface areas to 2000 $m^2 \cdot g^{-1}$, favorable for applications in energy storage.[69] For example, cellulose-derived carbon templated with MgO delivered a high reversible capacity of 793 $mAh \cdot g^{-1}$ as anodes for Li-ion batteries.[69] Further treatment of MgO-templated carbon at 1000−1500 °C results in the conversion of open pores to closed pores, giving hard carbons with Na storage capacity of 450 $mAh \cdot g^{-1}$.[68] Similar observations hold for Ca carbonate and acetate.[70]

Mg or Ca chloride hydrates, such as $MgCl_2 \cdot 6H_2O$ (T_m=118 °C) and $CaCl_2 \cdot 2H_2O$ (T_m=175 °C), have been used as combined solvents and porogens for porous carbon synthesis. These salt hydrates present much lower melting points compared to their anhydrous forms (772 °C for $MgCl_2$ and 708 °C for $CaCl_2$), making them good reaction media for the dissolution of precursors and the homogeneous condensation of organic compounds before they lose water and recrystallize, provided the presence of water is not detrimental to the process. During thermal treatment, these salt hydrates undergo dehydration (water evaporation), intermediate crystallization, subsequent melting, and recrystallization, finally creating solid templates for the formation of mesoporosity. The melting and removal of crystal water from salt hydrates overlap, leading to dynamic formation and depletion of solid salt throughout the condensation process. Moreover, the interactions between the carbonaceous phase and salt phase can further complicate these processes, potentially influencing the final properties of the synthesized porous carbon material. Understanding and controlling these interactions are crucial for tailoring the morphology, pore structure, and compositions of resulting carbon materials for specific applications.

For example, pyrolysis of adenine and $MgCl_2 \cdot 6H_2O$ yields N-doped carbons exhibiting a special anisotropic tubular porosity, a SSA of 2780 $m^2 \cdot g^{-1}$, and a pore volume up to 3.86 $cm^3 \cdot g^{-1}$.[54] The hydrogen bonding between adenine and $MgCl_2$ hydrates stabilizes specific crystal facets and promotes unidirectional crystal growth (***Figure 1.6***). As the temperature rises, the organic phase undergoes condensation and solidification, while the dehydration and decomposition of salts are delayed. The carbonizing phase surrounds the fiber-shaped salt, preserving the one-dimensional configuration of the intermediate salt phase, ultimately yielding porous carbons showing tubular aligned channels and highly porous structure. A similar highly parallel tubular structure was also observed with adenosine as a precursor.[71]

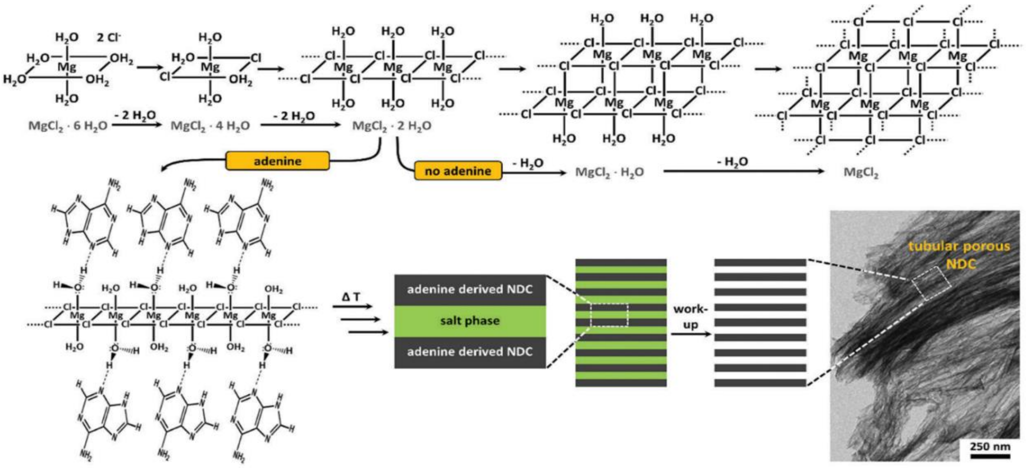

Figure 1.6. Schematic illustration of the secondary templating model during the synthesis of adenine-derived N-doped carbons obtained with $MgCl_2 \cdot 6H_2O$ as reaction medium the influence of alkali salt on the porous carbon structure. Reproduced from Ref. [54] with permission from the Royal Society of Chemistry.

$CaCl_2 \cdot 2H_2O$ has also been used for porous carbon synthesis. For instance, the use of ribose and adenine as precursors along with $CaCl_2 \cdot 2H_2O$ as a template results in the formation of oxygen-rich carbon nitrides with oxygen and nitrogen contents of 12 and 20 wt%, respectively, which remain stable from 600 to 800 °C.[56] During thermal treatment, ribose and $CaCl_2 \cdot 2H_2O$ form a supramolecular eutectic complex *via* hydrogen bonding at temperatures below 300 °C as a homogeneous starting mixture. $CaCl_2 \cdot 2H_2O$ catalyzes the dehydration and condensation of ribose, accelerating the formation of carbonaceous matter. Meantime, $CaCl_2$ hydrates gradually lose crystalized water, and the formed $CaCl_2$ recrystallizes at 500–700 °C, serving as a hard template contributing to the formation of mesoporous structures. It is noteworthy that the walls of these mesopores consist of onion-like packed bent graphitic layers of N, O-doped carbons. This method has proven effective in forming mesoporous structures when utilizing various aromatic compounds with hydroxyl groups as carbon precursors.

1.3.2.3 Transition metals

Anhydrous **$ZnCl_2$** has been widely utilized in both organic synthesis and porous carbon synthesis due to its unique properties to facilitate diverse chemical processes. In organic synthesis, it acts as a Lewis acid catalyst, effectively accepting electron pairs from other molecules and facilitating various reactions,[72–74] even at an industrial scale. In porous carbon synthesis, anhydrous $ZnCl_2$ is a conventional chemical activation agent during the carbonization and activation process of biomass-derived materials.[75,76] In this process, $ZnCl_2$ initially acts as a dehydration agent, catalyzes the polymerization of molecular precursors, and promotes the carbonization of organic species, thereby increasing the carbon yield. Additionally, $ZnCl_2$ serves as a molecular template, creating microporosity within the carbon structure by forming nanoscopic salt clusters within the carbon particles, while preventing the contraction of carbon frameworks.[75]

In the salt-templating strategy, anhydrous $ZnCl_2$ is used as a combined solvent and template (structural directing agent), especially when molecular precursors like nucleobases are used.[52,77] During synthesis, these carbon precursors or oligomers remain stable at the melting temperatures of $ZnCl_2$ (280 °C) or its eutectic salt mixtures (< 280 °C), and dissolve in or are miscible with the molten salt(s) before condensation. This use of $ZnCl_2$ as a solvent allows for lower condensation temperature and homogeneous product structures than the bulk synthesis. Besides, the molten $ZnCl_2$ acts as liquid templates for the formation of micropores, as they are used as activation agents.

Finally, considering the boiling point of pure $ZnCl_2$ of 732 °C, $ZnCl_2$ could start evaporation at around 500 ºC and dramatically evaporates above 700 ºC. This evaporation will cause an intensive enhancement in the volume of micropores, especially increasing synthetic temperature from 700 to 800 ºC. For example, the carbonaceous products show virtually no surface area at 500 ºC, similar SSAs of 850 $m^2 \cdot g^{-1}$ at 600 and 700 ºC, but a remarkable SSA increase at 800 ºC (1982 $m^2 \cdot g^{-1}$).[78] The increase of SSA at 800 ºC is ascribed to the combination of $ZnCl_2$ vapor pressure (named as "popcorn effect" by Kossmann and coworkers) and rupture of covalent networks. Note that the final products still need to be washed with diluted acids or water to remove $ZnCl_2$ despite this evaporation.

Recently, Zhao et al. reported that **Mn^{2+}** can influence the structure of hard carbon for higher Na storage ability.[79] The possible mechanism includes: (a) Mn^{2+} is coordinated with cellulose to capture oxygen-containing functional group at 200–400 ºC; (b) Mn^{2+} bridges the short-range disordered carbon layer at 400–800 ºC, enabling the removal of oxygen-containing defects and conversion from sp^3 to sp^2 carbon; and (c) Mn^{2+} catalyzes the graphitization process, allowing the rearrangement of carbon layers forming nano-graphite domains and carbon micropores at high temperatures of 800–1400 ºC. The use of $MnCl_2$ during synthesis leads to a suitable carbon layer spacing (0.36–0.40 nm) for Na ion intercalation. In contrast, the use of Fe, Co, and Ni leads to a smaller spacing (around 0.34 nm) close to the graphite carbon, which is unfavorable for Na ion intercalation, and Cu as a catalyst result in many defects on the carbon surface.

1.3.2.4 p-block metals

The conventional selection of salt melts for carbon synthesis has mainly focused on s-block (LiCl, NaCl, or KCl) and d-block metal chlorides ($ZnCl_2$), with limited exploration of p-block metals. Density function theory calculations have demonstrated that the p-orbital of p-block metals can interact with the p-orbital of oxygen, facilitating charge transfer between them.[80] Recently, **$SnCl_2$**, a p-block metal chloride, has been reported as a non-innocent salt melt medium to synthesize nanoporous carbons.[55] The use of $SnCl_2$ as a salt melt shows distinct advantages: (a) the eutectic mixture of $SnCl_2$ and KCl (4:1 mass ratio) possesses a very low melting point (180 °C), making it favorable for low-temperature synthesis, (b) the high affinity of Sn for oxygen facilitates the extraction of oxygen from oxygen-rich precursor (red carbon), leading to the formation of extended 2D structures composed exclusively of sp^2 carbons and conjugated oxygen species at mild temperatures as low as 300 °C, (c) the transition from Sn(II) to Sn(IV) facilitates the reductive deoxygenation and condensation of carbon precursors, forming carbon materials with low oxygen content, and (d) the rapid condensation of precursor and the formation of SnO_2 nanoparticles contribute to the formation of stable porous networks, with almost overlapped adsorption isotherms observed between 400 and 800 °C.

1.4 Rational design of porous carbons for capacitive energy storage

Capacitive energy storage offers the advantages of high power density, long lifespan, and good safety, but is hindered by low energy density. High-surface-area porous carbons serve as important electrodes in devices based on capacitive energy storage, such as supercapacitors and hybrid ion capacitors. This section will present the basics of electrochemical capacitors and design strategies of porous carbons for capacitive energy storage.

1.4.1 Basics of electrochemical capacitors

Supercapacitors are a kind of high-power energy storage devices that store energy at electrode-electrolyte interfaces. The capacitance of the electrochemical interfaces has traditionally been divided into two distinct types: electric double-layer capacitance (EDLCs) and pseudocapacitance. EDLC is formed by ion adsorption and desorption processes through electrostatic forces on a high surface area electrode, mostly porous carbons without involving faradaic reactions.[81] In comparison, pseudocapacitive charge storage involves charge transfer or partial charge transfer across the electrochemical interface, producing both faradaic and non-faradaic currents on electrode surfaces. The typical pseudocapacitive materials include metal oxides, metal hydroxides, or conducting polymers. Unlike batteries, where diffusion limitations in the electrode materials are dominant, the charge storage process in a supercapacitor is dominated by a surface-controlled process, thus providing high power capability and cyclic stability but low energy density compared with batteries. The energy density (E) depends on the specific capacitance (F) of electrode materials and overall cell voltage (V), described by the equation of $E=1/2CV^2$.[82] The energy density can be enhanced by increasing the capacitance of porous electrodes or building asymmetric capacitors to widen the potential gap between electrodes.

Zn-ion capacitor (ZIC) is a novel hybrid electrochemical energy storage device comprising a Zn anode, a porous carbon cathode, and an aqueous electrolyte.[25,83–85] Zn metal is a promising anode in aqueous electrolytes due to its high stability in air and aqueous solutions, safety, low cost, high theoretically specific capacity of 820 $mAh\cdot g^{-1}$, and a low redox potential of −0.76 *vs.* standard hydrogen electrode. In the ZIC system, the energy is stored/released by Zn plating/stripping at the anode and either EDLC or pseudocapacitance process at the porous cathode. The low redox potential of Zn anode allows aqueous ZICs to achieve higher cell voltages (1.6–1.8 V) compared to symmetrical supercapacitors (around 1 V). This, combined with the high theoretical capacity of Zn anode, results in higher energy densities of ZICs than conventional supercapacitors. Meanwhile, the rapid, reversible capacitive charge storage process at the porous carbon cathode brings higher power density and cycling stability of ZICs compared to conventional batteries. All of the above characteristics make ZIC a viable alternative or complement to supercapacitors and batteries in scenarios demanding high power and energy densities.

Despite the potential of ZICs, their practical application is hindered by their low specific capacities (< 150 $mAh\cdot g^{-1}$) and a comparatively short life span (< 100,000 cycles) due to the unfavorable design of porous cathodes and electrolytes. It is crucial to design porosities and compositions of cathode materials for effective ion storage and transfer. Optimization of electrolyte composition is also essential to expand the voltage window and inhibit parasitic reactions. Addressing the low utilization and limited stability of the Zn anode can be achieved through the design of anode interfacial layers or electrolyte systems. Besides, current studies mainly focus on developing new cathode materials for higher device performance but lack insights into the fundamental charge-discharge processes. Key questions, including the types of charge carriers within cathode pores (proton or Zn^{2+}), the respective contributions of proton and Zn^{2+}, and the influence of electrode structure (porosity and composition) on ion sorption and dynamics, remain unanswered.

Na-ion capacitors typically comprise a battery-type electrode, a capacitor-type electrode, and an organic electrolyte.[23,24] Battery-type electrodes, such as graphite, hard carbon, or layered structures, featured ordered carbon structures that promote faradaic-type energy storage for high energy density output. The capacitor-type electrodes offer large surface areas and open pore volumes to enhance power density. The use of organic electrolytes allows for higher cell voltages and energy density, as opposed to aqueous electrolytes. A typical Na-ion capacitor involves hard carbon as the anode and porous carbon as the cathode in an electrolyte including 1 M $NaClO_4$ in ethylene carbonate, dimethyl carbonate, and ethyl methyl carbonate of 1:1:1 vol%.[86,87] Na-ion capacitors offer notable advantages, including higher energy density than EDLCs and higher power density than Na-ion batteries. To optimize overall device performance, it is crucial to design anodes capable of withstanding high current density and high-capacity cathodes. This requires a thoughtful structural design of surface area, pore size distribution, and ordering of carbon structure.

1.4.2 Porosity

Porosity plays a crucial role in designing a porous carbon material for capacitive-type devices. Different pore characteristics, such as surface area, pore size distribution, pore connectivity, and pore shape, are expected depending on the specific roles of materials in the device and the type of electrolytes. Generally, it is assumed that the capacitance of EDLC follows that of a parallel-plate capacitor (***Equation 9***):

$$C = \frac{\varepsilon_r \varepsilon_0 A}{d} \text{ or } C/A = \frac{\varepsilon_r \varepsilon_0}{d} \tag{9}$$

where ε_r is the relative permittivity of the electrolyte, ε_0 is the permittivity of vacuum, A is electrode surface area accessible to electrolyte ions, and d is the effective thickness of the electric double layer (the Debye length). The equation shows that the capacitance C is proportional to A and is inversely proportional to d. Increasing A allows for more charge storage, while a smaller effective thickness of the electric double layer (d) means that the charge can be stored more densely.

It is expected and indeed observed that a large **surface area** (A) provides enough ion adsorption/reaction sites for charge storage.[51,88] However, this C-A linearity is based on the following two assumptions: (a) all the surface area accessed by N_2 or Ar is also available for electrolyte ions, and (b) the micropore surface area has the same electro-adsorption behavior as those of mesopore and external surface area. Despite these assumptions, the capacitance is not linearly proportional to the total surface area.[89] This discrepancy arises from several considerations. Firstly, the surface area available to Ar or N_2 molecules at 87 or 77 K is not equal to the surface area available for electrolyte ions to charge storage. The smallest pore size measured by Ar or N_2 (kinetic diameter: 0.34 nm for Ar, 0.36 nm for N_2)[90] may be smaller than the diameter of electrolyte ions. Secondly, challenges such as incomplete wetting of porous electrodes and non-equilibrium charge/discharge rates also influence the utilization of pores. In these cases, the increase in surface area cannot always lead to larger capacitance.

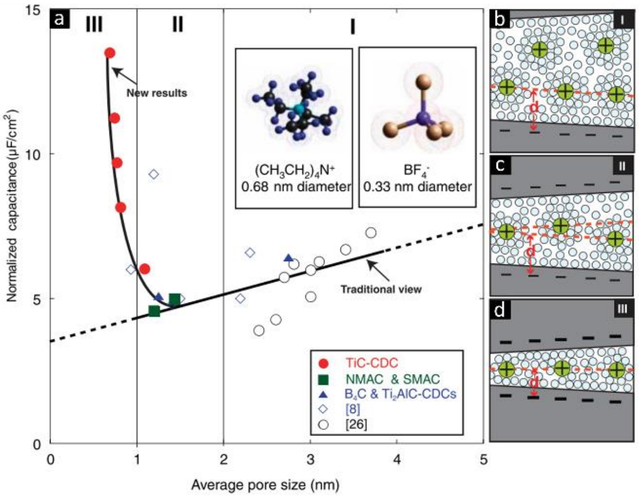

Figure 1.7. (a) Dependence of specific capacitance normalized by BET-SSA for the carbons with the same electrolytes on the average pore size. The normalized capacitance decreases with decreasing pore size while increasing below a critical value. When the pore size becomes large enough to accommodate diffuse charge layers, the capacitance would approach a constant value. (b–d) Schemes of solvated ions inside pores with distance between adjacent pore walls (b) larger than 2 nm, (c) between 1 and 2 nm, and (d) less than 1 nm. Reproduced with permission.[51] Copyright 2006, the American Association for the Advancement of Science.

On the other hand, the contributions from **micropore**, **mesopore**, and **macropore** to the double-layer capacitance are different, possibly related to variations in solvation structures of electrolyte ions and the availability of functional groups in confined situations. The **pore size distributions** should be designed to maximize the electrode surface accessible to electrolyte ions. Traditionally, pores smaller than the solvated ions are believed to not contribute to energy storage and larger pores are required to maximize specific capacitance.[51] However, in 2006, Gogotsi and co-workers reported an anomalous capacitance increase in carbon with subnanometer pores compared with other carbon materials with pore sizes above 2 nm (***Figure 1.7***).[51] This phenomenon is ascribed to the partial desolvation of electrolyte ions and the distortion of solvation shells in subnanometer pores, allowing for a closer approach of ion centers to the electrode surface.

Huang further constructed a universal model to describe the contribution of different pores to capacitance, considering pore curvature (***Figure 1.8***). This model proves applicable to a diverse carnage of carbon materials (activated carbon, template carbon, and CDC) and electrolytes (organic, aqueous, and ionic liquid electrolytes). In this model, macropores are large enough to ignore pore curvature, thus allowing for the use of a conventional EDLC model. For a mesopore with a cylindrical shape, solvated counterions enter and approach the pore wall, forming an electric double-cylinder capacitor. The capacitance is described by ***Equations 10*** and ***11***:

$$C = \frac{2\pi\varepsilon_r\varepsilon_0 L}{\ln(b/a)} \tag{10}$$

$$C/A = \frac{\varepsilon_r\varepsilon_0}{b\ln[\frac{b}{b-d}]} \tag{11}$$

in which L is the pore length and b and a are the radii of the outer and inner cylinders, respectively. For micropores, the solvated/desolvated counterions line up along the pore axis to form an electric wire-in-cylinder capacitor. The capacitance is calculated by ***Equation 12***.

$$C/A = \frac{\varepsilon_r\varepsilon_0}{b\ln[b/a_0]} \tag{12}$$

in which a_0 is the radius of solvated cations. In this model, d is not the determining factor for capacitance but a_0. For the carbon materials with multimodal pores, the capacitance can be calculated by ***Equation 13***.

$$C = \sum_i \frac{\varepsilon_{r,micro}\varepsilon_0 A_{i,micro}}{b_i\ln(b_i/a_0)} + \sum_j \frac{\varepsilon_{r,meso}\varepsilon_0 A_{j,meso}}{b_j\ln[b_j/(b_j-d)]} + \sum_k \frac{\varepsilon_{r,macro}\varepsilon_0 A_{k,macro}}{d} \tag{13}$$

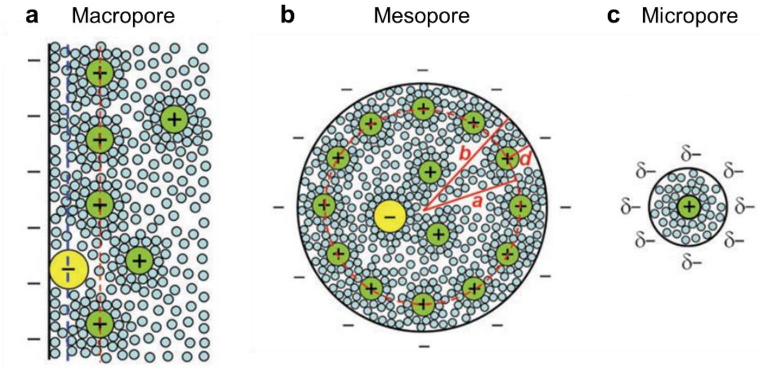

Figure 1.8. Schematic diagrams of (a) an EDLC formed at the carbon/electrolyte interface in which the inner and outer Helmholtz planes are represented by blue and red dashed lines, respectively. Cations are solvated by solvent molecules; (b) a negatively charged mesopore with solvated cations approaching the pore wall to form an electric double-cylinder capacitor with radii b and a for the outer and inner cylinders, respectively, separated by a distance d; (c) a negatively charged micropore of radius b with solvated cations of radius a_0 lining up to form an electric wire-in-cylinder capacitor. Reproduced with permission.[92] Copyright 2008, Wiley-VCH.

The author also observed that organic ions tend to desolvate before entering subnanometer pores, whereas aqueous electrolyte ions can retain their hydration shell in subnanometer pores. In general, the capacitances decrease at increasing current densities, attributed to the ionic diffusion process.

The decrease is more pronounced in microporous carbon than mesoporous carbon, which is ascribed to the solvation/desolvation process of ions, typically for organic electrolytes in micropores. In the aqueous electrolytes, the charge carriers are hydrated, exhibiting large hydrated ionic sizes and strong interaction with surrounding water molecules (large hydration enthalpy) (***Table 1.2***), making the mobility and diffusion of ions in confined pores more difficult. It is reported that large charge carriers may undergo a partial dehydration process when entering small carbon pores.[93,94]

Table 1.2. Selected ionic sizes and thermodynamic characteristics of electrolyte ions.

Ions	Bare ionic sizes (nm)[a]	Number of water molecules in the hydration shell (n)[a, b]	Hydrated ionic sizes (nm)[a]	Hydration free energy (kJ·mol^{-1})[c]
H^+	0.060	12.0	0.564	–1050
Li^+	0.120	5.2	0.764	–475
Na^+	0.190	3.5	0.716	–365
K^+	0.266	2.6	0.662	–295
Cs^+	0.338	2.1	0.658	–250
Zn^{2+}	0.148	9.6	0.860	–1955
Mg^{2+}	0.130	10.0	0.856	–1830
Al^{3+}	0.100	20.4	0.950	–4525
NO_3^-	0.528	2.0	0.670	–300
SO_4^{2-}	0.580	3.1	0.758	–1080

Note: [a] The sizes/diameters of bare and hydrated ions and the number of water molecules in the hydration shell are obtained from Ref.[95] [b] The number of water molecules in both the first and second solvent shells of ions is considered. [c] The hydration-free energies of related ions are obtained from Ref.[96]

While extensive studies exist on how porosity influences supercapacitors, systematic discussions on this issue in Zn-ion capacitors have been limited and yielded controversial conclusions. For example, Wang *et al.* believed that the transport of $Zn(H_2O)_6^{2+}$ is hindered in micropores due to its large hydration size (0.86 nm) and large hydration enthalpy (–1955 kJ·mol^{-1}), while mesopores increase ion accessibility and utilization of active sites.[97,98] However, in this study,[97] the microporous carbon has a much lower SSA (1274 m^2·g^{-1}) than the mesoporous carbon (3553 m^2·g^{-1}). The microporous carbon has a higher normalized capacity by SSA than the mesoporous one. Namely, the performance difference is more related to the large SSA difference than the pore size. Additionally, the used samples present different compositions, particularly in terms of nitrogen (13.57 at% *vs.* 2.67 at%)[97] and oxygen content (5.2 at% *vs.* 14.8 at%),[98] which also significantly influence device performance. In addition to pore structure, the large differences in SSA and elemental composition among comparison samples can also contribute to the final performance but are rarely discussed in the above studies.

On the other hand, different from the viewpoint above those larger pores bring better performance, Ma *et al.* believed that matching ion sizes (hydrated Na, Zn, or Al ions) and pore sizes of electrode materials leads to higher spatial charge density (550 $C \cdot cm^{-3}$) and volume energy density (165 $Wh \cdot L^{-1}$). Zhao *et al.* also further proposed that ultramicropores are favorable for the desolvation of Zn ions for higher capacitance.[99] This view is similar to the desolvation phenomenon of solvated ions when entering subnanometer pores in supercapacitors reported by Gogotsi *et al.*

1.4.3 Surface functionalization

Capacitive electrodes store charges on the carbon surface, but the initial carbons may perform poorly in energy storage applications due to limited interaction with electrolytes and sluggish interfacial processes. Therefore, it is crucial to modify the surface chemistry of carbon to enhance performance, in addition to optimizing porosity. Surface modification has the potential to drastically alter the physical and electrochemical properties of carbon materials. In general, porous carbons can be functionalized through methods such as heteroatom doping or constructing composites where carbon entraps nanoparticles/atoms or molecules, even without covalent bonding. Here, we primarily focus on the former.

Adding surface groups (*e.g.,* O, N, B, and P) to porous carbons allows for the modification of surface wettability and reactivity of porous carbons, possibly inducing a specific “chemistry” towards guest species.[100–102] The direct carbonization of heteroaromatic precursors can ensure more uniform distributions of functional groups in the bulk materials and avoid pore blocking.[103,104] Post-treatment of carbon materials with heteroatom-containing chemicals (*e.g.,* nitride acid, O_2, or urea) mainly introduces functional groups on the carbon surface.[105] The specific roles of heteroatoms in energy storage devices are discussed below.

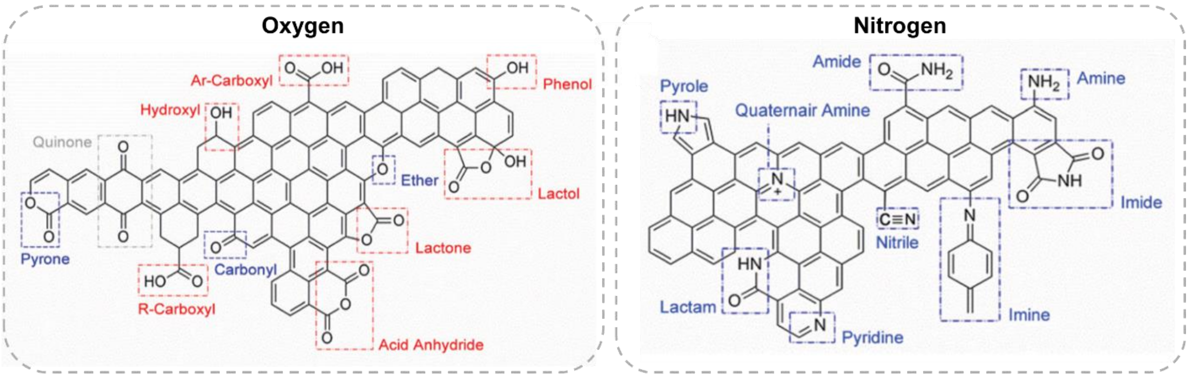

Figure 1.9. Common functional groups in carbon networks due to the presence of heteroatoms. (a) Oxygen and (b) nitrogen. Basic and acid functionalities indicated in blue and red. Reproduced with permission.[112] Copyright 2013, RSC Publishing.

Oxygen is an inevitable element in carbon materials. Both the type and content of oxygen-containing functional groups significantly influence the physical and electrochemical properties of porous carbons (***Figure 1.9***). First, specific hydrophilic oxygen groups, such as hydroxyl and carboxyl groups enhance the polarity and wettability of carbon pores, increasing pore accessibility in aqueous electrolytes.[106,107] Secondly, certain oxygen groups can adsorb solvent molecules and accelerate desolvation of electrolyte ions, facilitating their rapid entry into micropores.[108] Thirdly, some groups create additional pseudocapacitance through reversible faradaic reactions, thereby increasing the overall device capacitance. For example, basic functional groups like carbonyl and quinone react with protons in acidic aqueous solutions (***Equation 14***), while acidic groups like phenol and carboxyl react with hydroxyl ions in basic aqueous solutions (***Equation 15–17***).[109] However, these groups make limited contributions to neutral electrolytes.

$$>C{=}O + H^+ + e^- \rightleftharpoons >C\text{-}OH \tag{14}$$

$$>C\text{-}OH + OH^- \rightleftharpoons >C{=}O + H_2O + e^- \tag{15}$$

$$-COOH + OH^- \rightleftharpoons -COO^- + H_2O \tag{16}$$

$$>C{=}O + OH^- \rightleftharpoons >COOH + e^- \tag{17}$$

The mentioned properties could contribute to increased capacitance and rate capability. However, it is important to note that excessively high oxygen content leads to reduced electrode conductivity, clogged or collapsed micropores, and increased ionic transport resistance, thus deteriorating device performance such as capacitance, rate, and cycling stability.

Nitrogen is a widely explored heteroatom with promising results in electrochemical energy storage (***Figure 1.9***). Similarly, the introduction of electron-rich N into carbon networks can supply more electrons to the delocalized π-system of carbon networks (graphitic N, pyridine N, pyrrolic N) for higher electrical conductivity.[105] Secondly, these polar N groups exhibit better affinity to aqueous electrolytes, favoring the wetting of electrodes and ion diffusion into the electrode, leading to enhanced capacitance and rate performance of supercapacitors and Zn-ion capacitors.[110,111] Thirdly, certain N groups serve as active sites to provide additional faradic pseudo-capacitance (***Figure 1.10***). In acidic electrolytes, N-induced defects can increase the capacitance by hosting more protons, facilitating ion mobility and interfacial charge transport.[101]

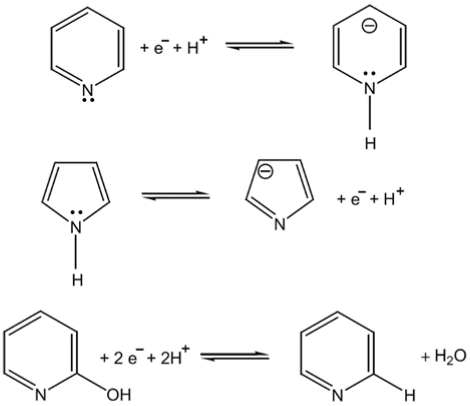

Figure 1.10. Possible redox reactions involving pyridinic, pyrrolic, and pyridone-type N species. Reproduced with permission.[105] Copyright 2015, RSC Publishing.

Phosphorus (P), possessing the same number of valence electrons and a larger atomic radius than N, shows similar chemical properties but stronger electron-donating capability than N. Therefore, P doping can increase the electrical conductivity of electrode materials and accelerate the desolvation of hydrated Zn ions for higher performance in Zn-ion capacitors.[99] **Boron** (B) is easily doped into the carbon lattice due to its comparable electronic structure and size with carbon. With three valence electrons, boron enters the carbon lattice by substituting carbon at the trigonal sites and acts as an electron acceptor, promoting charge transfer between neighboring carbons and favoring oxygen chemisorption on the carbon surface.[113]

1.5 Major challenges

1.5.1 Understand synthetic mechanism

In current carbon research, a broad spectrum of carbons is synthesized using diverse starting materials and synthetic strategies. Traditionally, porous carbon synthesis has been considered somewhat of a “black-box” process, where various reactants are put in a container to heat, mysteriously yielding magical black powders showing significant effects in diverse applications. The term "carbonization" has been frequently, perhaps excessively, employed to describe this complex process. The chemical or physical processes governing the formation of covalent networks and pore structures remain empirical and unclear. **Transforming these black-box processes into solid-state organic chemistry holds promises for achieving more controlled carbon synthesis, with higher yield and the precise tuning of compositions and porosities for particular applications.** This requires knowledge of carbon materials, organic chemistry, polymer chemistry, and even electrochemistry.

1.5.2 Increase carbon yield

While carbon yield significantly influences the industrial applications of porous carbons, it has not been sufficiently emphasized and is seldom reported in recent research literatures. This lack of emphasis is primarily attributed to the prevalent issue of low carbon yields, often below 10%, especially for carbons with high SSAs exceeding 2000 $m^2 \cdot g^{-1}$. Certain carbon types, such as those derived from MOFs or metal-organic salts, exhibit low yields due to a stronger tendency for carbon atoms to escape rather than incorporate into the carbon networks. Addressing this challenge necessitates the exploration of new synthetic strategies to enhance carbon yields. Meantime, it is worthwhile to mention that these unforgotten yield data may hold important insights into the synthetic mechanism of porous carbons, which should be carefully recorded and analyzed.

1.5.3 Lower synthesis temperature

Currently, synthesizing ordered graphite structures (2500–3000 ^{o}C) or hard carbon (1000–1500 ^{o}C) typically demands very high temperatures due to the limited carbon atom mobility in their covalently bonded layers.[6,114] Obtaining porous carbons requires temperatures between 800 and 1000 ^{o}C for precursor condensation (decomposition of heteroatom-containing groups), pore network development, or Zn template evaporation. Notably, such high synthetic temperatures pose challenges in terms of reaction equipment, electricity consumption, production cost, and environmental impact. Meanwhile, the synthetic process becomes less controlled at high temperatures. Consequently, there is a continual pursuit of low-temperature synthesis, driving advancements in precursor or catalyst designs.

1.5.4 Remove metal residual

While the carbonized products are washed multiple times with diluted acid or water at the end of synthesis, there are still residual metals in the final carbon products. This is particularly evident when using nitrogen-rich carbon precursor and $ZnCl_2$, owing to Lewis acid-base interactions between Zn^{2+} and terminal N sites. For example, using 1,2-dicyanobenzene as a precursor and $LiCl/ZnCl_2$ as a combined solvent and porogen leads to a carbon product after washing with 5.66 wt% N and 1.33 wt% residual coordinated Zn, as measured by inductively coupled plasma-optical emission spectroscopy.[115] X-ray photoelectron ray spectra reveal even higher N (13.61%) and Zn (2.95%) content. The dominant N sites are pyridinic and pyrrolic, indicating abundant terminal sites due to Zn-N bonds.

The presence of residual metals may be beneficial or harmful depending on the specific applications. For example, using the residual metals, Fellinger and co-workers developed a facile and mild synthesis strategy to achieve metal coordination of active-site imprinted nitrogen-doped porous carbons.[115] By exchanging Mg with Fe, Zn, or Co, they proved that $Zn\text{-}N_x$ sites are inactive for oxygen reduction reaction, while Fe and Co show strong performance enhancement. On the other hand, it is essential to note that even trace amounts of metal may contribute to the final performance in specific applications like catalysis, but it is difficult to determine the individual contributions from metal or carbon. Arbitrarily attributing the combined result of metal and carbon solely to the presence of carbon is irresponsible and may give misleading conclusions.

1.5.5 Understand structure-performance relationship

While numerous porous carbons have been created for emerging novel energy storage devices, the understanding of how specific structural features like pore size or surface chemistry impact device performance remains elusive. This limitation arises from the lack of ideal model materials only differing in one parameter while keeping others constant. For example, developing a series of porous carbons that differ only in pore sizes while maintaining identical SSAs and chemical compositions would provide valuable insights into the role of pore size in energy storage.

Maintaining identical preparation and testing methods is crucial to analyzing the influences of structural differences, requiring strict consistency in electrode loading, thickness, or electrolyte dosage across all experiments.

1.6 Outline of this thesis

Based on the above considerations, this thesis will develop a facile and innovative synthetic strategy for porous carbon materials by initially applying the “Cs effect” from organic chemistry to carbon science and present a renewed understanding of the role of Cs on condensation and activation of carbon materials. The obtained Cs-mediated porous carbons will be explored in capacitive energy storage, with a highlight on the influence of pore size and surface chemistry on capacitive energy storage.

Self-templating is a facile strategy for synthesizing porous carbons through direct pyrolysis of metallic organic salts. However, the method often encounters low yields (< 4%) and limited specific surface areas (< 2000 $m^2 \cdot g^{-1}$), attributed to the low activity of regular metal cations (*e.g.,* K^+ or Na^+) in promoting the construction and activation of carbon frameworks. To simultaneously boost yield and surface areas of porous carbon materials, this thesis will demonstrate the huge potential of organic Cs salt, cesium acetate, as a self-templating precursor, and the promising applications of porous carbons in CO_2 adsorption and supercapacitor. Importantly, this thesis will help to understand and rationally tailor material by organic solid-state chemistry (**Chapter 2**).

Facile synthesis of high-surface-area porous carbon with a high yield is crucial for large-scale applications. Despite the importance of carbon yields in both fundamental study and practical production, they are rarely reported and analyzed in many studies. By rational design of molecular precursors, this work increases carbon yield while keeping high specific surface areas. A nonconventional electron injection and ion intercalation mechanism will be presented to explain the simultaneous boost in carbon yield and surface area. The final porous carbon materials find important applications in Zn and Na-ion capacitors (**Chapter 3**).

Capacitive energy storage systems are known for high power and long cyclicity. Carbonaceous materials stand out as promising capacitive materials due to their large specific surface area, abundant porosities, and high stability. While pore structure impacts the electrochemical behaviors of Zn-ion capacitors, the exact mechanism by which pore size influences device performance and charge storage mechanism remains unclear, due to the absence of good model materials for systematical analysis. This thesis will address this gap by presenting a facile synthesis strategy to obtain model materials for cathodes of Zn-ion capacitors, aiming to unravel the effect of porosity on practical devices (**Chapter 4**).

Overall, this thesis will serve as an example of how the less explored element, Cs, can revolutionize conventional carbon science, leading to a facile synthetic process, lower synthesis temperature, large surface areas, and tunable porosities. The ease of synthesis and the diversity of carbon structures will bring new insights into carbon synthesis, and unlock a multitude of application possibilities. Possible research directions are also presented, such as the understanding of synthetic mechanisms by advanced characterizations and the explorations of extensive metal species in porous carbon synthesis (**Chapter 5**).

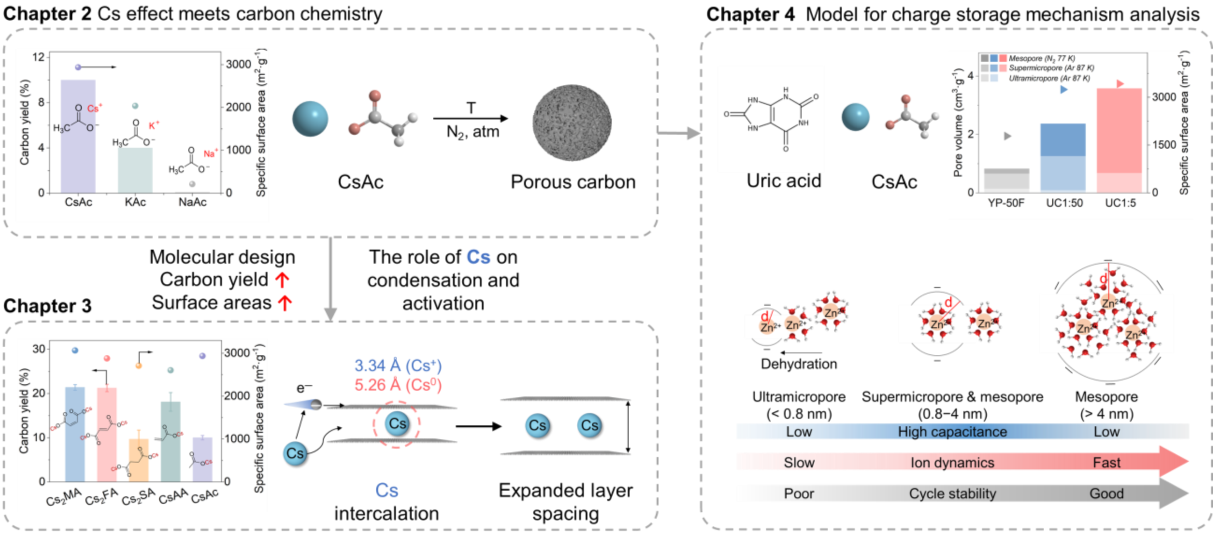

Figure 1.11. Graphical overview of the outline of this thesis.

Reference

[1] N. Yang, S. Yu, J. V. MacPherson, Y. Einaga, H. Zhao, G. Zhao, G. M. Swain, X. Jiang, *Chem. Soc. Rev.* **2019**, *48*, 157.

[2] H. Zhang, Y. Yang, D. Ren, L. Wang, X. He, *Energy Storage Mater.* **2021**, *36*, 147.

[3] T. Xu, W. Shen, W. Huang, X. Lu, *Mater. Today Nano* **2020**, *11*, 100081.

[4] M. F. El-Kady, Y. Shao, R. B. Kaner, *Nat. Rev. Mater.* **2016**, *1*, 16033.

[5] Y. Jang, S. M. Kim, G. M. Spinks, S. J. Kim, *Adv. Mater.* **2020**, *32*, 1902670.

[6] L. Xie, C. Tang, Z. Bi, M. Song, Y. Fan, C. Yan, X. Li, F. Su, Q. Zhang, C. Chen, *Adv. Energy Mater.* **2021**, *11*, 2101650.

[7] L. F. Zhao, Z. Hu, W. H. Lai, Y. Tao, J. Peng, Z. C. Miao, Y. X. Wang, S. L. Chou, H. K. Liu, S. X. Dou, *Adv. Energy Mater.* **2021**, *11*, 2002704.

[8] B. Zheng, X. Lin, X. Zhang, D. Wu, K. Matyjaszewski, *Adv. Funct. Mater.* **2020**, *30*, 1907006.

[9] L. Wang, X. Hu, *Chem. - An Asian J.* **2018**, *13*, 1518.

[10] X. Gao, H. Liu, D. Wang, J. Zhang, *Chem. Soc. Rev.* **2019**, *48*, 908.

[11] Y. Fang, Y. Liu, L. Qi, Y. Xue, Y. Li, *Chem. Soc. Rev.* **2022**, *51*, 2691.

[12] F. Pan, K. Ni, T. Xu, H. Chen, Y. Wang, K. Gong, C. Liu, X. Li, M. L. Lin, S. Li, X. Wang, W. Yan, W. Yin, P. H. Tan, L. Sun, D. Yu, R. S. Ruoff, Y. Zhu, *Nature* **2023**, *614*, 95.

[13] E. Meirzadeh, A. M. Evans, M. Rezaee, M. Milich, C. J. Dionne, T. P. Darlington, S. T. Bao, A. K. Bartholomew, T. Handa, D. J. Rizzo, R. A. Wiscons, M. Reza, A. Zangiabadi, N. Fardian-Melamed, A. C. Crowther, P. J. Schuck, D. N. Basov, X. Zhu, A. Giri, P. E. Hopkins, P. Kim, M. L. Steigerwald, J. Yang, C. Nuckolls, X. Roy, *Nature* **2023**, *613*, 71.

[14] M. Antonietti, M. Oschatz, *Adv. Mater.* **2018**, *30*, 1706836.

[15] Z. Yang, J. Ren, Z. Zhang, X. Chen, G. Guan, L. Qiu, Y. Zhang, H. Peng, *Chem. Rev.* **2015**, *115*, 5159.

[16] X. Fu, L. Xu, J. Li, X. Sun, H. Peng, *Carbon* **2018**, *139*, 1063.

[17] L. Li, L. Wang, T. Ye, H. Peng, Y. Zhang, *Small* **2021**, *17*, 2005015.

[18] L. Wang, F. Wan, Y. Xu, S. Xie, T. Zhao, F. Zhang, H. Yang, J. Zhu, J. Gao, X. Shi, C. Wang, L. Lu, Y. Yang, X. Yu, S. Chen, X. Sun, J. Ding, P. Chen, C. Ding, F. Xu, H. Yu, H. Peng, *Nat. Nanotechnol.* **2023**, *18*, 1085.

[19] L. Ye, M. Liao, K. Zhang, M. Zheng, Y. Jiang, X. Cheng, C. Wang, Q. Xu, C. Tang, P. Li, Y. Wen, Y. Xu, X. Sun, P. Chen, H. Sun, Y. Gao, Y. Zhang, B. Wang, J. Lu, *Nature* **2024**, *626*, 313.

[20] M. M. Shulaker, G. Hills, N. Patil, H. Wei, H. Y. Chen, H. S. P. Wong, S. Mitra, *Nature* **2013**, *501*, 526.

[21] Q. Wang, J. Yan, Z. Fan, *Energy Environ. Sci.* **2016**, *9*, 729.

[22] F. Béguin, V. Presser, A. Balducci, E. Frackowiak, *Adv. Mater.* **2014**, *26*, 2219.

[23] P. Cai, K. Zou, X. Deng, B. Wang, M. Zheng, L. Li, H. Hou, G. Zou, X. Ji, *Adv. Energy Mater.* **2021**, *11*, 2003804.

[24] K. Subramanyan, M. L. Divya, V. Aravindan, *J. Mater. Chem. A* **2021**, *9*, 9431.

[25] D. Zhang, L. Li, Y. Gao, Y. Wu, J. Deng, *ChemElectroChem* **2021**, *8*, 1541.

[26] J. Kim, M. S. Choi, K. H. Shin, M. Kota, Y. Kang, S. Lee, J. Y. Lee, H. S. Park, *Adv. Mater.* **2019**, *31*, 1803444.

[27] C. Wu, Y. Lei, L. Simonelli, D. Tonti, A. Black, X. Lu, W. H. Lai, X. Cai, Y. X. Wang, Q. Gu, S. L.

Chou, H. K. Liu, G. Wang, S. X. Dou, *Adv. Mater.* **2022**, *34*, 2108363.

[28] A. S. Alzahrani, M. Otaki, D. Wang, Y. Gao, T. S. Arthur, S. Liu, D. Wang, *ACS Energy Lett.* **2021**, *6*, 413.

[29] Q. Lu, Y. Jie, X. Meng, A. Omar, D. Mikhailova, R. Cao, S. Jiao, Y. Lu, Y. Xu, *Carbon Energy* **2021**, *3*, 957.

[30] M. Thommes, K. Kaneko, A. V. Neimark, J. P. Olivier, F. Rodriguez-Reinoso, J. Rouquerol, K. S. W. Sing, *Pure Appl. Chem.* **2015**, *87*, 1051.

[31] J. Lee, J. Kim, T. Hyeon, *Adv. Mater.* **2006**, *18*, 2073.

[32] Z. Heidarinejad, M. H. Dehghani, M. Heidari, G. Javedan, I. Ali, M. Sillanpää, *Environ. Chem. Lett.* **2020**, *18*, 393.

[33] W. Li, J. Liu, D. Zhao, *Nat. Rev. Mater.* **2016**, *1*, 16023.

[34] H. Nishihara, T. Kyotani, *Adv. Mater.* **2012**, *24*, 4473.

[35] C. Liang, Z. Li, S. Dai, *Angew. Chem. Int. Ed.* **2008**, *47*, 3696.

[36] Y. Deng, J. Wei, Z. Sun, D. Zhao, *Chem. Soc. Rev.* **2013**, *42*, 4054.

[37] W. Shou, R. Guo, H. Pan, D. D. Gang, *Dekker Encycl. Nanosci. Nanotechnology, Third Ed.* **2015**, 1.

[38] N. Fechler, T. P. Fellinger, M. Antonietti, *Adv. Mater.* **2013**, *25*, 75.

[39] M. Sevilla, A. B. Fuertes, *ACS Nano* **2014**, *8*, 5069.

[40] H. Peng, S. Qi, Q. Miao, R. Zhao, Y. Xu, G. Ma, Z. Lei, *J. Power Sources* **2021**, *482*, 228993.

[41] B. Yan, H. Huang, X. Qin, S. Xiu, J. Choi, D. Ko, T. Chen, W. Zhang, B. Quan, G. Diao, X. Jin, Y. Piao, *ACS Appl. Energy Mater.* **2021**, *4*, 13735.

[42] S. Wang, J. Miao, B. Ren, Y. Xu, Z. Tian, L. Zhang, Z. Liu, *J. Alloys Compd.* **2022**, *920*, 165946.

[43] J. Ren, Y. Huang, H. Zhu, B. Zhang, H. Zhu, S. Shen, G. Tan, F. Wu, H. He, S. Lan, X. Xia, Q. Liu, *Carbon Energy* **2020**, *2*, 176.

[44] A. Han, B. Wang, A. Kumar, Y. Qin, J. Jin, X. Wang, C. Yang, B. Dong, Y. Jia, J. Liu, X. Sun, *Small Methods* **2019**, *3*, 1800471.

[45] B. Liu, H. Shioyama, T. Akita, Q. Xu, *J. Am. Chem. Soc.* **2008**, *130*, 5390.

[46] A. Li, Y. Tong, H. Song, X. Chen, *J. Phys. Chem. C* **2018**, *122*, 17278.

[47] W. Chaikittisilp, M. Hu, H. Wang, H. S. Huang, T. Fujita, K. C. W. Wu, L. C. Chen, Y. Yamauchi, K. Ariga, *Chem. Commun.* **2012**, *48*, 7259.

[48] V. Presser, M. Heon, Y. Gogotsi, *Adv. Funct. Mater.* **2011**, *21*, 810.

[49] Y. Gogotsi, A. Nikitin, H. Ye, W. Zhou, J. E. Fischer, B. Yi, H. C. Foley, M. W. Barsoum, *Nat. Mater.* **2003**, *2*, 591.

[50] Y. Gogotsi, R. K. Dash, G. Yushin, T. Yildirim, G. Laudisio, J. E. Fischer, *J. Am. Chem. Soc.* **2005**, *127*, 16006.

[51] J. Chmiola, G. Yushin, Y. Gogotsi, C. Portet, P. Simon, P. L. Taberna, *Science* **2006**, *313*, 1760.

[52] J. Kossmann, D. Piankova, N. V. Tarakina, J. Heske, T. D. Kühne, J. Schmidt, M. Antonietti, N. López-Salas, *Carbon* **2021**, *172*, 497.

[53] J. Kossmann, M. L. O. Sánchez-Manjavacas, J. Brandt, T. Heil, N. López-Salas, J. Albero, *Chem. Commun.* **2022**, *58*, 4841.

[54] J. Pampel, A. Mehmood, M. Antonietti, T. P. Fellinger, *Mater. Horizons* **2017**, *4*, 493.

[55] X. Zheng, Z. Tian, R. Bouchal, M. Antonietti, N. López-Salas, M. Odziomek, *Adv. Mater.* **2023**, 2311575.

[56] C. Li, E. Lepre, M. Bi, M. Antonietti, J. Zhu, Y. Fu, N. López-Salas, *Adv. Sci.* **2023**, *10*, 2300526.

[57] X. Liu, M. Antonietti, *Adv. Mater.* **2013**, *25*, 6284.

[58] R. D. Hunter, J. Ramírez-Rico, Z. Schnepp, *J. Mater. Chem. A* **2022**, *10*, 4489.

[59] Q. Yan, J. Li, X. Zhang, E. B. Hassan, C. Wang, J. Zhang, Z. Cai, *J. Nanoparticle Res.* **2018**, *20*, 223.

[60] H. Yoshida, S. Takeda, T. Uchiyama, H. Kohno, Y. Homma, *Nano Lett.* **2008**, *8*, 2082.

[61] J. Wang, S. Kaskel, *J. Mater. Chem.* **2012**, *22*, 23710.

[62] M. A. Lillo-Ródenas, D. Cazorla-Amorós, A. Linares-Solano, *Carbon* **2003**, *41*, 267.

[63] E. Raymundo-Piñero, P. Azaïs, T. Cacciaguerra, D. Cazorla-Amorós, A. Linares-Solano, F. Béguin, *Carbon* **2005**, *43*, 786.

[64] H. J. Lee, D. Ko, J. S. Kim, Y. Park, I. Hwang, C. T. Yavuz, J. W. Choi, *ChemNanoMat* **2021**, *7*, 150.

[65] J. Pampel, T. P. Fellinger, *Adv. Energy Mater.* **2016**, *6*, 1502389.

[66] J. Pampel, C. Denton, T. P. Fellinger, *Carbon* **2016**, *107*, 288.

[67] T. Morishita, T. Tsumura, M. Toyoda, J. Przepiórski, A. W. Morawski, H. Konno, M. Inagaki, *Carbon* **2010**, *48*, 2690.

[68] A. Kamiyama, K. Kubota, D. Igarashi, Y. Youn, Y. Tateyama, H. Ando, K. Gotoh, S. Komaba, *Angew. Chem. Int. Ed.* **2021**, *60*, 5114.

[69] C. Zhu, T. Akiyama, *Green Chem.* **2016**, *18*, 2106.

[70] S. Gu, Y. Wang, D. Zhang, M. Xiong, H. Gu, Z. Xu, *Chemosphere* **2022**, *289*, 133148.

[71] C. Li, Z. Song, M. Liu, E. Lepre, M. Antonietti, J. Zhu, J. Liu, Y. Fu, N. López-Salas, *Energy Environ. Mater.* **2024**, e12695.

[72] T. M. Lipińska, S. J. Czarnocki, *Org. Lett.* **2006**, *8*, 367.

[73] J. Sun, L. Wang, S. Zhang, Z. Li, X. Zhang, W. Dai, R. Mori, *J. Mol. Catal. A Chem.* **2006**, *256*, 295.

[74] D. B. Bankar, R. R. Hawaldar, S. S. Arbuj, M. H. Moulavi, S. T. Shinde, S. P. Takle, M. D. Shinde, D. P. Amalnerkar, K. G. Kanade, *RSC Adv.* **2019**, *9*, 32735.

[75] M. Molina-Sabio, F. Rodríguez-Reinoso, *Colloids Surfaces A Physicochem. Eng. Asp.* **2004**, *241*, 15.

[76] Z. Yue, C. L. Mangun, J. Economy, *Carbon* **2002**, *40*, 1181.

[77] J. Kossmann, R. Rothe, T. Heil, M. Antonietti, N. López-Salas, *J. Colloid Interface Sci.* **2021**, *602*, 880.

[78] J. Kossmann, T. Heil, M. Antonietti, N. López-Salas, *ChemSusChem* **2020**, *13*, 6643.

[79] J. Zhao, X. X. He, W. H. Lai, Z. Yang, X. H. Liu, L. Li, Y. Qiao, Y. Xiao, L. Li, X. Wu, S. L. Chou, *Adv. Energy Mater.* **2023**, *13*, 2300444.

[80] T. Wang, X. Cao, H. Qin, L. Shang, S. Zheng, F. Fang, L. Jiao, *Angew. Chem. Int. Ed.* **2021**, *60*, 21237.

[81] C. Chen, J. Feng, J. Li, Y. Guo, X. Shi, H. Peng, *Chem. Rev.* **2023**, *123*, 613.

[82] Y. Wang, Y. Song, Y. Xia, *Chem. Soc. Rev.* **2016**, *45*, 5925.

[83] J. Yin, W. Zhang, N. A. Alhebshi, N. Salah, H. N. Alshareef, *Adv. Energy Mater.* **2021**, *11*, 2100201.

[84] L. Dong, W. Yang, W. Yang, Y. Li, W. Wu, G. Wang, *J. Mater. Chem. A* **2019**, *7*, 13810.

[85] D. Sui, M. Wu, K. Shi, C. Li, J. Lang, Y. Yang, X. Zhang, X. Yan, Y. Chen, *Carbon* **2021**, *185*, 126.

[86] K. Wang, F. Sun, Y. Su, Y. Chen, J. Gao, H. Yang, G. Zhao, *J. Mater. Chem. A* **2021**, *9*, 23607.

[87] R. Fei, H. Wang, Q. Wang, R. Qiu, S. Tang, R. Wang, B. He, Y. Gong, H. J. Fan, *Adv. Energy Mater.* **2020**, *10*, 2002741.

[88] D. Lozano-Castelló, D. Cazorla-Amorós, A. Linares-Solano, S. Shiraishi, H. Kurihara, A. Oya, *Carbon* **2003**, *41*, 1765.

[89] H. Shi, *Electrochim. Acta* **1996**, *41*, 1633.

[90] K. A. Cychosz, R. Guillet-Nicolas, J. García-Martínez, M. Thommes, *Chem. Soc. Rev.* **2017**, *46*, 389.

[91] J. Chmiola, C. Largeot, P. L. Taberna, P. Simon, Y. Gogotsi, *Angew. Chem. Int. Ed.* **2008**, *47*, 3392.

[92] J. Huang, B. G. Sumpter, V. Meunier, *Chem. - A Eur. J.* **2008**, *14*, 6614.

[93] S. Fleischmann, Y. Zhang, X. Wang, P. T. Cummings, J. Wu, P. Simon, Y. Gogotsi, V. Presser, V. Augustyn, *Nat. Energy* **2022**, *7*, 222.

[94] H. Ma, H. Chen, M. Wu, F. Chi, F. Liu, H. Cheng, C. Li, L. Qu, *Angew. Chem. Int. Ed.* **2020**, *59*, 14541.

[95] E. R. Nightingale, *J. Phys. Chem.* **1959**, *63*, 1381.

[96] Y. Marcus, *J. Chem. Soc., Faraday Trans.* **1993**, *89*, 713.

[97] L. Wang, M. Peng, J. Chen, T. Hu, K. Yuan, Y. Chen, *Adv. Mater.* **2022**, *34*, 2203744.

[98] W. Jian, W. Zhang, X. Wei, B. Wu, W. Liang, Y. Wu, J. Yin, K. Lu, Y. Chen, H. N. Alshareef, X. Qiu, *Adv. Funct. Mater.* **2022**, *32*, 2209914.

[99] C. Zhao, Y. Lin, Q. Lin, Q. Liu, Y. Liu, Z. Liu, A. Ying, *Energy Storage Mater.* **2023**, *58*, 332.

[100] F. Wei, Y. Zeng, Y. Guo, J. Li, S. Zhu, S. Gao, H. Zhang, X. He, *Chem. Eng. J.* **2023**, *468*, 143576.

[101] M. Yang, Z. Zhou, *Adv. Sci.* **2017**, *4*, 1600408.

[102] C. Esen, E. Scoppola, Z. Song, E. Senokos, H. Zschiesche, D. Cruz, I. Lauermann, N. V Tarakina, M. Antonietti, P. Giusto, *Adv. Sci.* **2024**, 2310196.

[103] A. Stein, Z. Wang, M. A. Fierke, *Adv. Mater.* **2009**, *21*, 265.

[104] H. Wang, Y. Shao, S. Mei, Y. Lu, M. Zhang, J. K. Sun, K. Matyjaszewski, M. Antonietti, J. Yuan, *Chem. Rev.* **2020**, *120*, 9363.

[105] Y. Deng, Y. Xie, K. Zou, X. Ji, *J. Mater. Chem. A* **2015**, *4*, 1144.

[106] C. Qiu, L. Jiang, Y. Gao, L. Sheng, *Mater. Des.* **2023**, *230*, 111952.

[107] G. Franklin, E. M. Halim, C. Merlet, P. L. Taberna, P. Simon, *Electrochim. Acta* **2023**, *465*, 142944.

[108] S. Yang, X. Liu, X. Zhang, S. Tang, *J. Phys. Condens. Matter* **2021**, *33*, 445201.

[109] J. Yin, W. Zhang, W. Wang, N. A. Alhebshi, N. Salah, H. N. Alshareef, *Adv. Energy Mater.* **2020**, *10*, 2001705.

[110] X. Shi, J. Xie, F. Yang, X. Cao, Y. Yu, Q. Liu, X. Lu, *Angew. Chem. Int. Ed.* **2022**, *61*, e202214773.

[111] R. Yan, M. Antonietti, M. Oschatz, *Adv. Energy Mater.* **2018**, *8*, 1800026.

[112] F. De Clippel, M. Dusselier, S. Van De Vyver, L. Peng, P. A. Jacobs, B. F. Sels, *Green Chem.* **2013**, *15*, 1398.

[113] D. W. Wang, F. Li, Z. G. Chen, G. Q. Lu, H. M. Cheng, *Chem. Mater.* **2008**, *20*, 7195.

[114] Y. Chu, J. Zhang, Y. Zhang, Q. Li, Y. Jia, X. Dong, J. Xiao, Y. Tao, Q. H. Yang, *Adv. Mater.* **2023**, *35*, 2212186.

[115] D. Menga, F. Ruiz-Zepeda, L. Moriau, M. Šala, F. Wagner, B. Koyutürk, M. Bele, U. Petek, N. Hodnik, M. Gaberšček, T. P. Fellinger, *Adv. Energy Mater.* **2019**, *9*, 1902412.

Chapter 2 Cesium acetate as a self-templating precursor for porous carbons[1]

2.1 Facile synthesis of porous carbon by self-templating strategy

Crafting highly porous carbons simply and efficiently is essential for their broad-scale applications. Currently, they are primarily synthesized by activation or templating strategies.[1,2] The activation strategy is rather complex and time-consuming, involving the etching of carbon materials with abundant corrosive agents (*e.g.,* K and Na hydroxides) or high-temperature gaseous media (*e.g.,* CO_2, O_2, and H_2O), typically resulting in microporous carbon.[3,4] In contrast, mesostructured carbon is predominantly obtained through soft or hard templating methods.[5–7] However, these methods have drawbacks, such as the complex template synthesis (*e.g.,* SBA-15) or the need for template removal using harsh chemicals (*e.g.,* hydrofluoric acid). Self-templating strategy offers a promising method for the synthesis of porous carbon by direct calcination of single metal-containing precursors (*e.g.,* metal citrate and carboxyl salts).[8–11] Nonetheless, these reported K, Na, or Zn-containing precursors suffer from low carbon yields (< 4%) and limited SSAs (< 2000 $m^2 \cdot g^{-1}$). This is primarily due to the minor impact of K, Na, or Zn salts used in these cases on the formation and activation of carbon networks.

In contrast, Cs salts can be effective in facilitating the formation of polymeric and subsequent carbon networks and also demonstrate superior activation properties compared with K, Na, and Zn.[12–15] Actually, the phenomenon known as the "Cs effect" is a well-established term in organic chemistry, describing milder reaction conditions and higher carbon yields in the presence of Cs^+.[16–18] The mechanism behind this effect is largely empirical and not thoroughly understood. Many explanations attribute the enhanced performance to the larger ionic radius of Cs^+ (***Figure 2.1***), thus to its larger polarizability and reduced tendency to ion-pairing in solution. This renders Cs^+ a more efficient catalyst for nucleophilic substitutions compared to K^+ or Na^+. In addition, Cs salts, such as Cs_2CO_3, are crucial for C-H activation and C-H/C-O biaryl coupling, increasing yields threefold compared with K_2CO_3 as a catalyst.[19] Therefore, the effect is not solely related to the increased basicity of Cs species compared with K or Na. These characteristics make Cs organic

---

[1] Results of this chapter are adapted from the original work with permission of the authors: Jiaxin Li, Janina Kossmann, Ke Zeng, Kun Zhang, Bingjie Wang, Christian Weinberger, Markus Antonietti, Mateusz Odziomek, Nieves López-Salas, When High-Temperature Cesium Chemistry Meets Self-Templating: Metal Acetates as Building Blocks of Unusual Highly Porous Carbons, *Angew. Chem. Int. Ed.* **2023**, *135*, e202217808

compounds particularly promising as carbon material precursors. Changing K or Na organic salts to Cs is promising to enhance carbon yields and SSAs simultaneously.

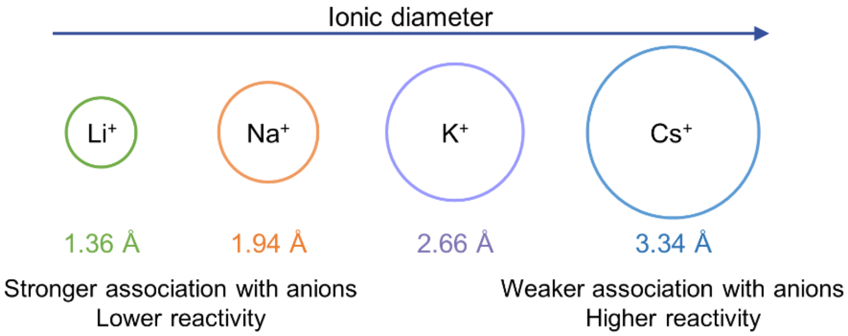

Figure 2.1. Schematic illustrating the influence of ionic sizes of alkali ions on their association degree with anions and reactivity.

Although cesium acetate (CsAc) has already been used in synthesizing carbon materials, it was solely regarded as a porogen.[20] The authors described the formation of highly porous carbons without considering the possibility that CsAc itself acts as a carbon atom donor in the carbon lattice. Motivated by these above facts, we assumed that the "Cs effect" could be exploited for constructing covalent networks and explored this possibility during the condensation of the simplest organic cesium salt, CsAc.

Chapter 2 introduces the synthesis of porous carbons featuring high SSAs (1000−3000 $m^2 \cdot g^{-1}$), multiscale pore structures, and adjustable oxygen level (7−12 wt%) using CsAc as the sole self-templating precursor. Subsequently, this chapter elucidates the synthesis mechanism governing the construction of carbon framework and the development of pores during CsAc pyrolysis and emphasizes the pivotal role of Cs in these processes. Finally, this chapter showcases the applications of resulting porous carbons as CO_2 adsorbents and electrodes in supercapacitors.

2.2 Structures and microstructures of CsAc-derived carbon materials

In a typical procedure, porous carbons are obtained by heating CsAc to temperatures of 500 to 800 °C in a nitrogen atmosphere, followed by acid washings to remove the remaining Cs species (***Figure 2.2***). The carbon yields of the resulting carbonaceous materials range from 15 to 10% between 500 and 800 °C, surpassing those obtained from previously reported organic metal precursors.[8–11]

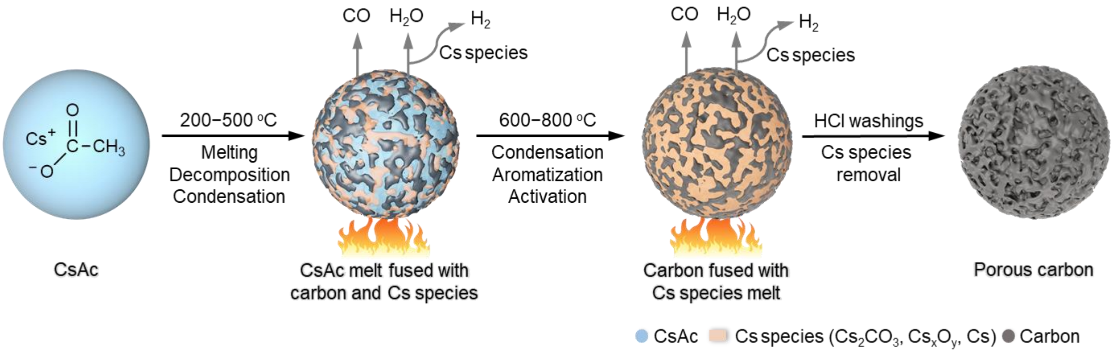

Figure 2.2. Facile synthesis of porous carbons with CsAc as the sole self-templating precursor.

Scanning electron microscopic (SEM) images (***Figure 2.3a−c***) show that the carbon products consist of primary colloidal particles (100−200 nm in size), which either fuse or tightly stack together to grape-like aggregates forming three-dimensional networks with colloidal interconnected voids measuring between 0.5 and 2.0 µm. This specific morphology is often but not always observed in salt melt synthesis of porous carbons, especially when precursors can dissolve in the ionic melt before condensation takes place and subsequently experience homogeneous nucleation to form carbonaceous materials from the salt melt.[21−23] Notably, in our method, there is no need for precursor dissolution since CsAc first melts and decomposes homogeneously. Transmission electron micrographs (TEM) of the products obtained between 500 and 700 °C (***Figure 2.3d−f***) depict the interconnected colloidal particles. In comparison, CsAc800 exhibits smooth surfaces probably because the molten Cs species preferentially etch away irregularities outside the colloidal particles.

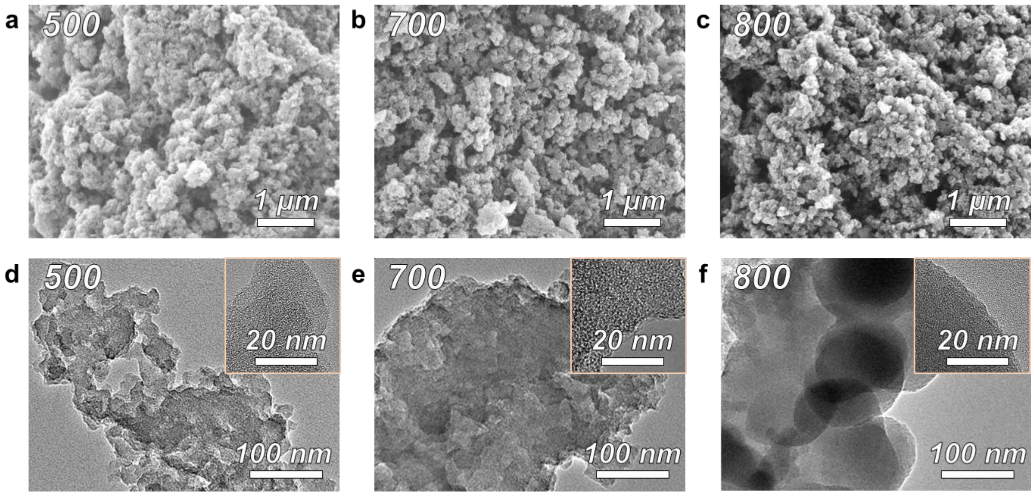

Figure 2.3. Morphologies of porous carbons obtained at 500, 700, and 800 °C. (a−c) SEM and (d−f) TEM images.

The pore structure of synthesized carbons was further evaluated through N_2 sorption measurements at 77 K. All sorption isotherms exhibit a rapid N_2 uptake at low relative pressures ($P/P_0 < 0.1$), indicating the presence of significant volumes of micropores (***Figure 2.4a***).[24,25] At higher relative pressures, the isotherms of products calcined between 600 and 800 °C show the features of Type II isotherm, characteristic of a gradual increase in N_2 adsorption without reaching a distinct plateau near P/P_0 of 0.9. The Type II isotherm is indicative of large mesopores and/or macropores. Furthermore, CsAc800 exhibits a steeper uptake in the relative pressure range from 0.3 to 0.6, suggesting the formation of small mesopores. As detailed in ***Table 2.1***, the samples demonstrate gradually increasing Brunauer-Emmett-Teller (BET) SSAs of 1015, 1534, 1983, and 2242 $m^2 \cdot g^{-1}$ at 450, 500, 600, and 700 °C, reaching up to 2936 $m^2 \cdot g^{-1}$ at 800 °C. The pore size distributions calculated using quenched solid density functional theory (QSDFT) adsorption equilibrium kernels are illustrated in ***Figure 2.4b***. All the samples exhibit multiscale porous structures comprising large micropores (pore width of 1−2 nm), small mesopores (pore width of 2−4 nm), and large mesopores (pore width of 20−40 nm). Notably, CsAc450 has a pore volume of 0.53 $cm^3 \cdot g^{-1}$, indicating effective construction and activation of carbon frameworks at a mild temperature. The pore volume increases to 0.90, 1.13, 1.29, and 1.89 $cm^3 \cdot g^{-1}$ at 500, 600, 700, and 800 °C, respectively. The obtained carbons are micropore-dominated below 800 °C, while CsAc800 owns comparable micropore and mesopore volumes (0.99 and 0.90 $cm^3 \cdot g^{-1}$).

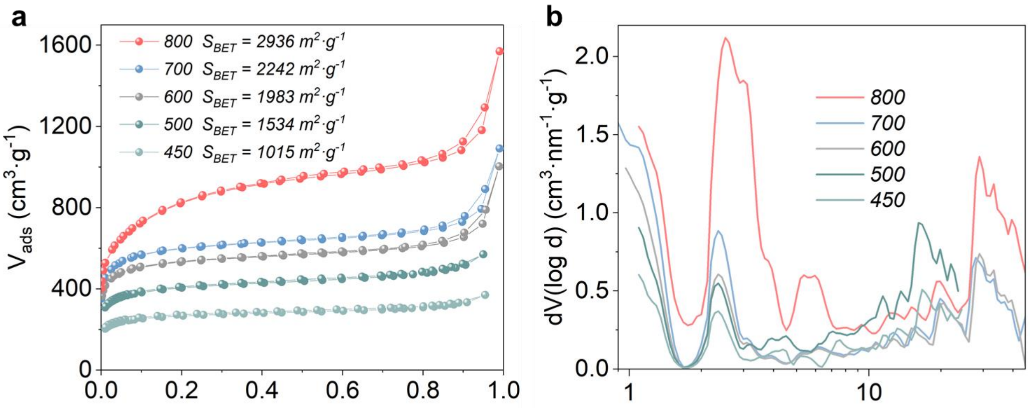

Figure 2.4. (a) N_2 sorption isotherms at 77 K; (b) pore size distributions of CsAc-derived porous carbons between 450 and 800 °C.

Table 2.1. Compositions and porosities of porous carbons obtained from CsAc between 450 and 800 °C.

T (°C)	C[a] (wt%)	H[a] (wt%)	O[a] (wt%)	Cs[b] (wt%)	S_{BET}[c] ($m^2 \cdot g^{-1}$)	$V_{1-2\ nm}$[d] ($cm^3 \cdot g^{-1}$)	$V_{2-50\ nm}$[d] ($cm^3 \cdot g^{-1}$)	V_T[e] ($cm^3 \cdot g^{-1}$)	CO_2 uptake[f] ($mmol \cdot g^{-1}$)	Carbon yield[g]
450	85.5	2.5	12.3	0.2	1015	0.33	0.17	0.53	3.80	15
500	86.2	1.4	12.2	0.2	1534	0.53	0.34	0.90	5.97	14
600	88.0	1.0	11.0	0.2	1983	0.64	0.49	1.13	8.71	13
700	88.7	0.9	9.2	0.1	2242	0.73	0.56	1.29	6.82	12
800	91.2	0.5	6.8	0.1	2936	0.99	0.90	1.89	7.21	10

[a] Chemical compositions were determined from elemental combustion analysis (C, H, O). [b] Metal contents were assessed from ICP−OES. The contents of C/H, O, and Cs were measured by different modes or methods, so the sum of mass ratios of these elements may not always equal 100%. [c] SSAs were determined by the multipoint BET model applied to N_2 adsorption isotherms at 77 K in the P/P_0 range from 0.05 to 0.25. [d] Micropore and mesopore volumes were calculated from N_2 adsorption/desorption isotherms at 77 K using the QSDFT model. [e] Total pore volumes were estimated from the volume adsorbed at P/P_0 approximately equal to 0.90. [f] The maximum CO_2 uptake capacity was obtained at 273 K and 100 kPa. [g] The carbon yields were calculated by dividing the mass of carbon products by that of acetate in the CsAc.

The chemical structures of the obtained carbons after washing were also carefully examined. The amount of Cs is below 0.1 wt% for all products according to the results of inductively coupled plasma optical emission spectroscopy (ICP−OES) measurements. Elemental combustion analyses reveal that the samples exhibit adjustable oxygen contents (6.8−12.5 wt%) (***Table 2.1***), indicating the role of acetates as carbon and oxygen sources. The oxygen content remains stable between 450 and 600 °C and decreases at higher temperatures (> 700 °C) due to the elimination of C=O by cesium-etching. X-ray diffraction (XRD) pattern of CsAc450 depicts one broad and low-intensity (002) diffraction peak centered at approximately 24° indicating the presence of graphitic stacking structures (***Figure 2.5a***). The (002) peak shifts to a higher angle from 450 to 600 °C and returns back to a lower angle for 800 °C sample. This indicates that the structure condenses firstly to smaller interlayer distances and then back to larger ones. Raman spectra exhibit D (~1350 cm^{-1}) and G (~1580 cm^{-1}) bands (***Figure 2.5b***), typically associated with disordered and ideal graphitic vibrations of carbonaceous materials. The overlapped D and G bands are characteristic of poorly ordered carbon structures, often present in highly porous, bent carbons with asymmetric heteroatom substitution. This observation is consistent with XRD results.

The infrared spectra further probe the surface chemical functionalities of the obtained carbons (***Figure 2.5c***). CsAc450 exhibits a broad peak at around 1700 cm^{-1} attributed to the vibrations of C=O groups, a broad peak at around 1600 cm^{-1} related to the stretching of C=C groups in the conjugated carbon networks, and a broad peak between 1400 and 950 cm^{-1} related to the stretching vibrations of C-O and bending vibration of C-H bonds. As the temperature increases, the signals of C=O, C-O, and C-H regions gradually weaken and vanish at 800 °C, indicating the formation of an extended conjugated structure in the carbon frameworks. X-ray photoelectron survey spectra (XPS) (***Figure 2.5d***) reveal that the carbons have two significant O 1s and C 1s peaks, consistent with the results of elemental combustion analysis. Further deconvolution of high-resolution C 1s spectra (***Figure 2.5e***) indicates that the presence of C=C (~284.6 eV), C-O (~286.4 eV), and C=O (~288.8 eV) groups in the carbons. No noticeable intensity changes in the above groups are observed at higher temperatures. The O 1s spectra of CsAc450 contain C=O (~531.8 eV, O doubly bonded to sp^2 carbon) and C-O groups (~533.3 eV, O singly bonded to sp^2 or sp^3 carbon) (***Figure 2.5f***). With increasing temperature, the peak intensity of the C-O group increases significantly compared with C=O group, suggesting the conversion of C=O to C-O on the carbon surfaces. This indicates a substantial increase in electron deficiency in the final material at higher temperatures.

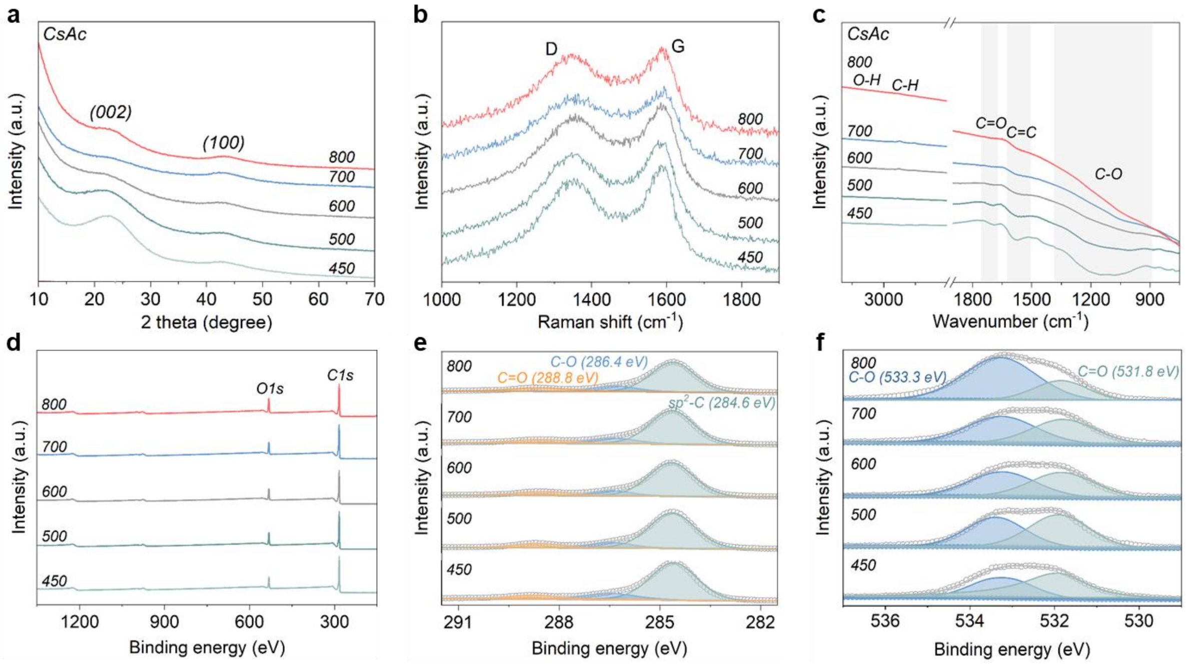

Figure 2.5. Chemical structures of CsAc-derived porous carbons between 450 and 800 °C. (a) XRD patterns; (b) Raman spectra; (c) infrared spectra; (d) X-ray photoelectron survey spectra; (e, f) high-resolution C 1s and O 1s X-ray photoelectron spectra.

2.3 Thermodynamic transformation of CsAc

To explain the formation mechanism of porous carbons, we investigated the pyrolysis process of CsAc using thermogravimetric analysis (TGA) coupled with the mass spectrometer (MS) and *in situ* XRD. TGA-MS curves (***Figure 2.6***) show CsAc undergoes a significant mass loss of approximately 31% at 390 °C, accompanied by the release of a substantial amount of hydrogen

(H_2, m/z=2) and water (H_2O, m/z=18). This indicates the rapid condensation of organic species and the formation of carbonaceous matter, phenomena also observed during biomass pyrolysis.[26] Acetates have been reported to decompose into acetone and further into ketene and methane at high temperatures.[27] Therefore, the ionic currents at m/z=58, 43, 42, 16, and 15 are attributed to acetone (CH_3COCH_3), acetate fragment ($CH_3CO\cdot$), ketene (CH_2CO), methane (CH_4), and methyl fragment ($CH_3\cdot$), respectively. Ketenes are highly reactive and rapidly polymerize, forming polyketone chains that further cross-link towards carbonaceous frameworks.[28,29] The cross-linking process generates the observed water molecules. The formation of H_2 is also likely favored by the elimination of water reacting with the *in situ* formed metallic Cs. No obvious mass loss and gas formation are observed between 520 and 640 °C, pointing at minor chemical evolution of carbon networks in this temperature range. The second sharp mass loss takes place from 650 to 810 °C with H_2 and CO evolution, indicating an intensive activation process by Cs species (*e.g.,* Cs_2CO_3, Cs oxides, or metal). The sharp mass drops below 25% of the initial mass observed at 800 °C is associated with the evaporation of molten Cs carbonate and oxides and Cs metal (boiling point of metallic Cs: 671 °C) with the helium flow.

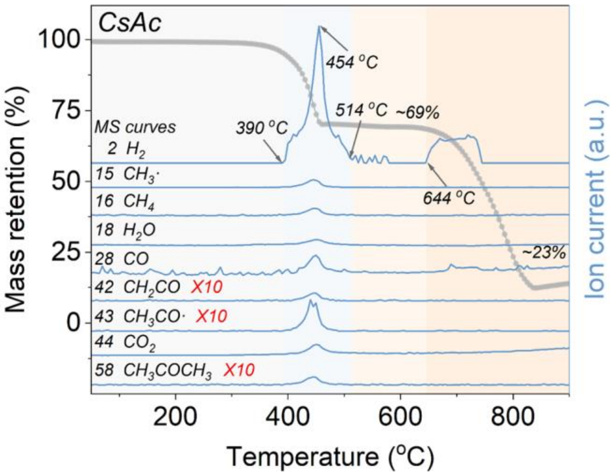

Figure 2.6. TGA-MS curves of CsAc under helium.

In situ XRD patterns of CsAc indicate that CsAc melts at around 200 °C, with all the peaks weakening or disappearing at 200 °C (***Figure 2.7***). The decomposition of CsAc is signaled by the appearance of sharp peaks ascribed to Cs_2CO_3 at 450 °C, in agreement with the results of TGA-MS. These diffraction peaks weaken from 450 to 700 °C and completely disappear at 800 °C, which is ascribed to the melting, decomposition, or evaporation of *in situ* formed Cs_2CO_3 at higher temperatures. The broad hump at around 18° is related to the Kapton window of the high-temperature chamber. During the cooling stage, several peaks appear below 700 °C owing to the recrystallization of Cs carbonate or oxides.

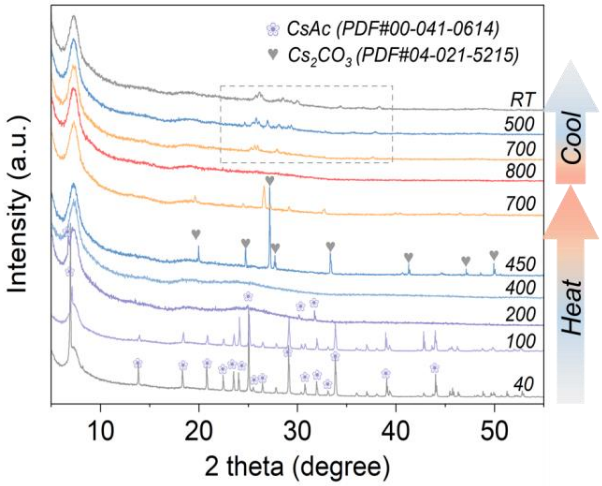

Figure 2.7. *In situ* XRD patterns of CsAc under helium.

2.4 Synthesis mechanism analysis

Based on the analysis above, we can summarize the formation process of porous carbon from the pyrolysis of CsAc as follows. CsAc undergoes decomposition, yielding ketene, ketonic species, and Cs_2CO_3 in the range of 400−450 °C (***Figure 2.8a***). The active ketenes promptly polymerize into polyketones,[28,29] which continue to undergo cross-linking, cyclization, and aromatization, forming oxygen-rich carbonaceous networks at temperatures as low as 450 °C (***Figure 2.8b***). The fast condensation of organic species and aromatization of carbonaceous networks generate a large amount of H_2 between 400 and 450 °C. It is worth mentioning that these processes can be accelerated by Cs^+ and CO_3^{2-} ions, promoting the formation of carbonaceous networks instead of decomposition, releasing gaseous products from the reaction medium. For example, Cs^+ and CO_3^{2-} ions can coordinate with oxygen functional groups like carbonyl groups and the acidic alkyl hydrogen of polyketone chains, accelerating the elimination of these functional groups and the formation of a fused ring intermediate framework. Besides, Cs^+ ions can also stabilize the polyketone moieties by favoring their enolate form and catalyzing intra- and inter-molecular crosslinking and aromatization reactions. This is particularly facilitated by the larger atomic sizes of Cs than K, Na, and Li. In addition to ketene, the acetone condensation is considered an alternative pathway contributing to carbon frameworks.

It is worth mentioning that the whole process of carbon network construction and Cs_2CO_3 formation takes place in homogenous molten salt because CsAc melts already below 200 °C (***Figure 2.8c***). This is favorable for the homogeneity of the final products. Besides, the carbonaceous matter and Cs species are simultaneously generated and kept in close contact, allowing the *in situ* nucleating Cs_2CO_3 to act as a templating and activation agent. Abundant porosity has been formed at this stage. At around 500−600 °C, the generated Cs_2CO_3 melts and decomposes into Cs oxides and Cs metal, all of which can function as activating agents to increase the number of open micropores. At 800 °C, the increased melting and volatilization of Cs species and activation reactions further open micro- and mesopores. Some possible activation reactions involving Cs species are present in ***Table 2.2***, based on standard Gibbs free energy calculations. Corresponding data for K species are also calculated for comparison.[30] While the activation reactions with K are also thermodynamically feasible, those reactions with Cs are kinetically more favorable due to effective contact and fast mass transfer between molten Cs species and carbon.

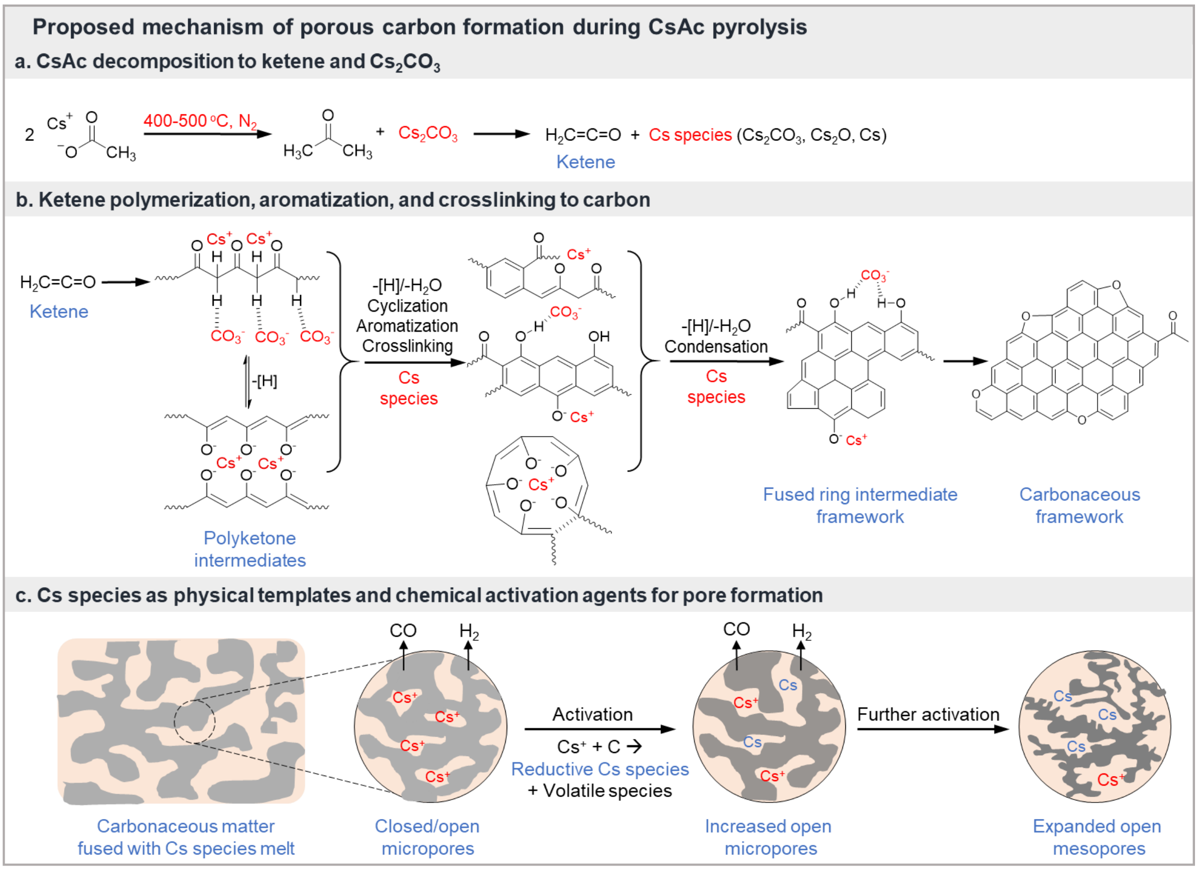

Figure 2.8. Proposed mechanism of porous carbon formation during CsAc pyrolysis.

Table 2.2. Standard Gibbs free energy calculations of possible activation reactions.

Reactions	Gibbs free energy (kJ·mol^{-1})					
	600 K	700 K	800 K	900 K	1000 K	1100 K
Cs_2CO_3 + -CH_2- → Cs_2O + 2CO + H_2	29.73	2.69	39.59	−2.26	−43.39	/
Cs_2CO_3 + 2-CH_2- → 2Cs + 3CO + 2H_2	−220.80	−265.40	−309.28	−352.70	−406.99	/
Cs_2O + -CH_2- → 2Cs + CO + H_2	−250.53	−268.09	−348.87	−350.44	−363.59	−768.08
CO_2 + -CH_2- → 2CO + H_2	57.60	36.18	14.62	−7.19	−29.23	−51.46
K_2CO_3 + -CH_2- → K_2O + 2CO + H_2	13.82	−14.08	−41.46	−68.46	−95.04	−68.55
K_2CO_3 + 2-CH_2- → 2K + 3CO + 2H_2	−223.03	−268.87	−313.99	−358.60	−402.65	−345.28
K_2O + -CH_2- → 2K + CO + H_2	−236.85	−254.79	−272.52	−290.13	−307.61	−276.73

To summarize, in the process of porous carbon formation, CsAc combines several important roles: (a) carbon/oxygen source, (b) condensation catalyst, (c) *in situ* formed physical template, and (d) activating agent. Cs^+ ions enable the synergetic and efficient progression of condensation and activation of carbonaceous frameworks, being responsible for the creation of highly porous structures. Compared with previous synthesis strategies of porous carbons (*e.g.,* carbonization-activation, template-assisted carbonization, and combined methods), this strategy is highly facile and efficient to reach ultrahigh SSAs without the need for expensive or harsh chemicals and tedious process.

To illustrate the distinct Cs effect in the structural evolution of acetate, the common metal acetates were also pyrolyzed and washed. The carbon derived from NaAc at 800 °C exhibits a negligible yield of 0.1% and a considerably low SSA of 212 m^2·g^{-1} and no carbonaceous material was obtained after pyrolysis of LiAc and Zn(Ac)$_2$ (***Figure 2.9***), indicating their incomparable properties with CsAc. In comparison, KAc-derived carbons show a lower yield (4%), SSA (2038 m^2·g^{-1}), and pore volume (0.96 cm^3·g^{-1}) than that from CsAc at 800 °C.

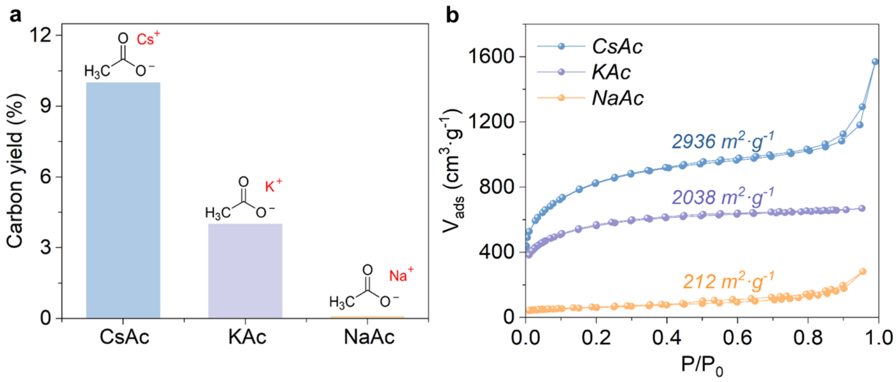

Figure 2.9. Carbon yields and N_2 sorption isotherms at 77 K of porous carbons obtained from the pyrolysis of CsAc, KAc, and NaAc as the sole self-templating precursor at 800 °C.

The specific catalytic effect of Cs species, superior to K or Na, is well recognized in organic chemistry and referred to as the “Cs effect” as mentioned before.[16–18] The effect is typically attributed to the larger ionic radius and higher polarizability of Cs^+ ions than other homologous ions (***Table 2.3***). These characteristics make Cs^+ ions more efficient catalysts for processes like nucleophilic substitution and C-H activation than K^+ and Na^+ ions.[19,31] These reactions are also crucial for the condensation of organic species to form carbonaceous networks. The formed rigid carbon frameworks further support the formation of nanopores, important for achieving high SSAs. Besides, the low melting points of Cs species also guarantee the filtration of molten Cs species into porous carbonaceous scaffolds for efficient activation, contributing to high SSAs. For instance, the melting point of Cs_2CO_3 is 610 °C, much lower than that of K_2CO_3 (891 °C) and Na_2CO_3 (851 °C) (***Table 2.3***). In comparison, the poor contact and sluggish mass transfer between solid K or Na salts and carbons hinder the activation process between 600 and 800 °C. Therefore, higher yields and higher SSAs can be simultaneously achieved in the presence of a Cs-based precursor.

Table 2.3. Properties of Li/Na/K/Cs and their carbonates and oxides.

Items	Li	Na	K	Cs
Atomic radius (Å)	1.52	1.86	2.31	2.62
Ionic radius (Å)	0.68	0.97	1.33	1.67
Electronic polarizability (10^{-24} cm^3)	0.029	0.179	0.83	2.42
Melting points of metal acetates (°C)	286	324	292	194
Melting points of metals (°C)	180	98	64	29
Boiling points of metals (°C)	1340	883	759	671
Melting points of carbonates (°C)	723	851	891	610
Melting points of oxides (°C)	Li_2O 1720	Na_2O 917	K_2O 740	Cs_2O 490
	Li_2O_2 450	Na_2O_2 460	K_2O_2 490	Cs_2O_2 594
			K_2O_3 430	Cs_2O_3 502
			KO_2 380	CsO_2 600

2.5 Applications in CO_2 capture and supercapacitor electrode

The high micropore volume and adjustable oxygen content of porous carbons prompt an exploration of their CO_2 capture performance (***Figure 2.10a***). CsAc500 exhibits a CO_2 adsorption capacity of 6.0 mmol·g^{-1} at 273 K and 100 kPa, with the value increasing to 8.7 mmol·g^{-1} for CsAc600, 6.8 mmol·g^{-1} for CsAc700, and 7.2 mmol·g^{-1} for CsAc800 (***Figure 2.10b***). At 298 K, the adsorption capacity decreases to 4.1−4.7 mmol·g^{-1} due to the exothermic nature of the adsorption process (***Figure 2.10c***). Based on the adsorption isotherms at 273 K and 298 K, the isosteric heats of adsorption (Q_{st}) are determined within the range of 15 to 30 kJ·mol^{-1} calculated by the Clausius-Clapeyron equation (***Figure 2.10d***), indicating *van der Waals* interactions between CO_2 and carbon. The Q_{st} values are comparable to the typical values (20−30 kJ·mol^{-1}) for porous carbons and lower than those of metal-organic frameworks (25−50 kJ·mol^{-1}) or zeolites (30−60 kJ·mol^{-1}).[32] A low Q_{st} value can help reduce energy consumption in the regeneration of adsorbent. The samples below 600 °C present higher Q_{st} values at low uptakes (< 2 mmol·g^{-1}) than those at high temperatures, explained by their rich surface oxygen functional groups.

In comparison to reported CO_2 adsorbents such as porous carbons,[33–37] metal-organic frameworks,[38–41] zeolites,[42] and porous organic polymers,[43–45] our materials show remarkable CO_2 capacities, reaching up to 38 wt% of carbon itself under ambient conditions, while avoiding the use of complex precursors and tedious synthesis (***Figure 2.10e***). The notable adsorption capacity is rationally ascribed to high ultramicropore volumes (pore width < 0.7 nm), known for their affinity towards CO_2 owing to the stronger interaction between CO_2 and two adjacent pore walls.[46,47] In addition, the large amounts of mesopores promote CO_2 diffusion to micropores.[48] Besides textural properties, the oxygen functional groups also contribute to an increased affinity for CO_2.[46,49,50] CsAc600 achieves the highest CO_2 uptake, possibly due to its balanced combination of high micropore volume and still high oxygen content. The adsorption amount remains stable over five adsorption/desorption cycles at 273 K (***Figure 2.10f***), demonstrating good stability and reusability. Furthermore, such high CO_2 uptake is not just favorable for CO_2 sorption but also holds significance for CO_2 conversion in electro-synthesis or metal-CO_2 batteries.[51]

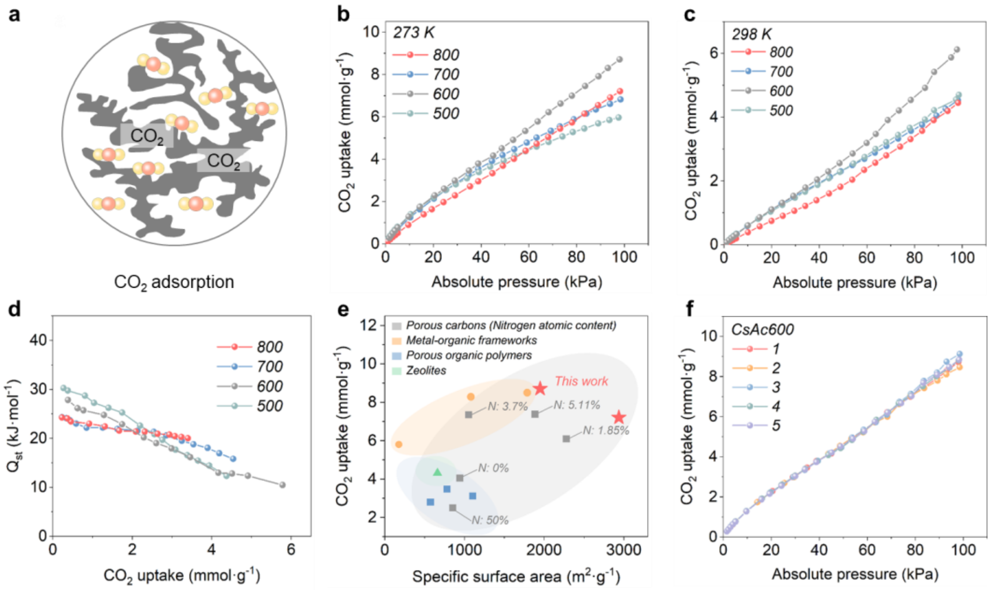

Figure 2.10. CO_2 sorption of CsAc-derived porous carbons between 500 and 800 °C. (a) Scheme; (b, c) CO_2 adsorption isotherms at 273 and 298 K; (d) isosteric heat values of CO_2 adsorption; (e) SSA and CO_2 uptake comparison with reported adsorbents; (f) CO_2 adsorption isotherms at 273 K of CsAc600 for five cycles.

The high SSAs, multiscale porosities, and oxygen groups in porous carbons are also favorably used for energy storage in supercapacitors based on ion sorption on the carbon surface. The energy-storage behaviors of porous carbons were evaluated in two-electrode symmetric supercapacitors using 1 M H_2SO_4 aqueous electrolyte in Swagelok cells. Cyclic voltammetry curves of the samples exhibit quasi-rectangular shapes (***Figure 2.11a***), indicative of the contribution of electric double-layer capacitances at electrode-electrolyte interfaces. Galvanostatic charge-discharge tests show that CsAc800 exhibits a high specific capacitance and rate performance (313 $F\cdot g^{-1}$ at 0.1 $A\cdot g^{-1}$, 90 $F\cdot g^{-1}$ at 10 $A\cdot g^{-1}$) (***Figure 2.11b***). No discernible internal resistance drop is observed in the charge-discharge curves, indicating effective interfacial charge transfer. The high specific capacitance of CsAc800 is rationally ascribed to its large SSA and the presence of supremicropores and small mesopores. The micropores provide rich adsorption sites for electrolyte ions, whereas mesopores accommodate a large volume of electrolyte ions for effective ion diffusion. The device finally demonstrates a specific energy of 11 $Wh\cdot kg^{-1}$ at 25 $W\cdot kg^{-1}$. At a high specific power of 2,500 $W\cdot kg^{-1}$, a specific energy of 5 $Wh\cdot kg^{-1}$ can still be retained. Finally, CsAc800 shows good cycling stability at 10 $A\cdot g^{-1}$, with 94.7% capacitance retention after 10, 000 cycles (***Figure 2.11c***).

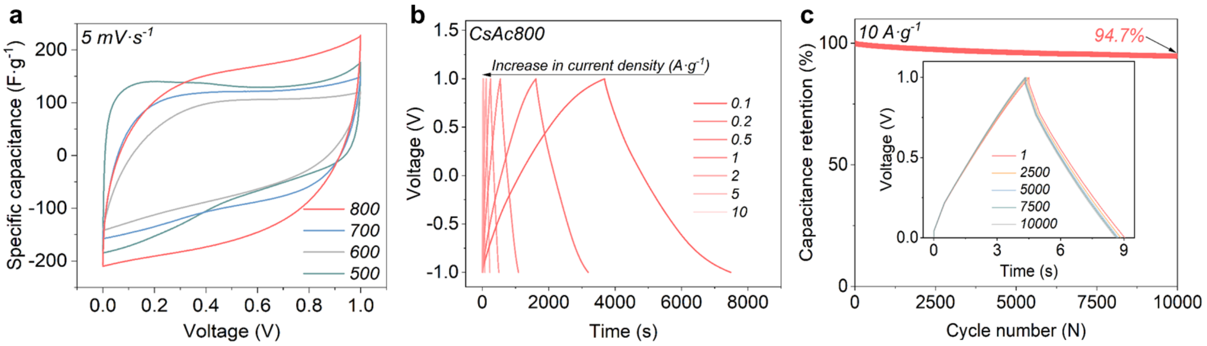

Figure 2.11. (a) CV curves at 5 $mV\cdot s^{-1}$; (b) charge-discharge curves at various current densities of CsAc800; (c) capacitance retention over 10,000 cycles of CsAc800 at 10 $A\cdot g^{-1}$. Inset image, the selected charge-discharge curves at selected cycles.

To summarize, this chapter presents a straightforward and robust approach for producing porous carbons with decent carbon yields, high SSAs, large pore volumes, rich pore structures, and surface oxygen functionalities by one-step thermal treatment of CsAc. Importantly, we have clarified that CsAc serves as a unique precursor that decomposes to presumably ketenes/ketones acting as carbon/oxygen source and Cs species as *in situ* formed templating and activating agents. The carbonaceous frameworks are rapidly constructed and activated by *in situ* generated Cs species embedded within the frameworks, leading to high-SSAs porous carbons that have demonstrated tremendous potential for CO_2 adsorption and energy storage. This method is industrially feasible due to the use of a simple precursor and facile steps. It is also easy to extend the synthesis to various heteroatom-rich porous carbons by introducing appropriate second precursors containing heteroatoms like nitrogen, phosphorus, sulfur, or boron. We also believe that Cs species can be easily recovered and transformed into CsAc again, making the process more sustainable and economical. Overall, this chapter may provide new insights into carbon science by applying the Cs effect and a still rare solid organic chemistry.

Reference

[1] W. Tian, H. Zhang, X. Duan, H. Sun, G. Shao, S. Wang, *Adv. Funct. Mater.* **2020**, *30*, 1909265.

[2] J. Yin, W. Zhang, N. A. Alhebshi, N. Salah, H. N. Alshareef, *Small Methods* **2020**, *4*, 1900853.

[3] J. Wang, S. Kaskel, *J. Mater. Chem.* **2012**, *22*, 23710.

[4] S. Yu, H. Wang, C. Hu, Q. Zhu, N. Qiao, B. Xu, *J. Mater. Chem. A* **2016**, *4*, 16341.

[5] A. Kamiyama, K. Kubota, D. Igarashi, Y. Youn, Y. Tateyama, H. Ando, K. Gotoh, S. Komaba, *Angew. Chem. Int. Ed.* **2021**, *60*, 5114.

[6] J. Liu, T. Yang, D. W. Wang, G. Q. Lu, D. Zhao, S. Z. Qiao, *Nat. Commun.* **2013**, *4*, 2798.

[7] L. Peng, H. Peng, Y. Liu, X. Wang, C. Te Hung, Z. Zhao, G. Chen, W. Li, L. Mai, D. Zhao, *Sci. Adv.* **2021**, *7*, eabi7403.

[8] M. Sevilla, A. B. Fuertes, *ACS Nano* **2014**, *8*, 5069.

[9] B. Yan, H. Huang, X. Qin, S. Xiu, J. Choi, D. Ko, T. Chen, W. Zhang, B. Quan, G. Diao, X. Jin, Y. Piao, *ACS Appl. Energy Mater.* **2021**, *4*, 13735.

[10] H. Peng, S. Qi, Q. Miao, R. Zhao, Y. Xu, G. Ma, Z. Lei, *J. Power Sources* **2021**, *482*, 228993.

[11] S. Wang, J. Miao, B. Ren, Y. Xu, Z. Tian, L. Zhang, Z. Liu, *J. Alloys Compd.* **2022**, *920*, 165946.

[12] K. Okada, N. Yamamoto, Y. Kameshima, A. Yasumori, *J. Colloid Interface Sci.* **2003**, *262*, 179.

[13] J. Zhou, Z. Li, W. Xing, H. Shen, X. Bi, T. Zhu, Z. Qiu, S. Zhuo, *Adv. Funct. Mater.* **2016**, *26*, 7955.

[14] L. Zhu, Y. Li, J. Zhang, X. Gan, Q. Li, T. Tang, Y. Chen, J. Zhu, N. Guo, L. Wang, S. Zhang, *Appl. Surf. Sci.* **2023**, *638*, 158051.

[15] Y. Liu, H. Cui, J. Xu, J. Shi, W. Wang, N. Yan, J. Zou, S. You, *Chem. Phys. Lett.* **2023**, *826*, 140655.

[16] T. Flessner, S. Doye, *J. fuer Prakt. Chemie* **1999**, *341*, 186.

[17] C. Galli, *Org. Prep. Proced. Int.* **1992**, *24*, 285.

[18] G. Dijkstra, W. H. Kruizinga, R. M. Kellogg, *J. Org. Chem.* **1987**, *52*, 4230.

[19] H. Xu, K. Muto, J. Yamaguchi, C. Zhao, K. Itami, D. G. Musaev, *J. Am. Chem. Soc.* **2014**, *136*, 14834.

[20] N. Fechler, G. A. Tiruye, R. Marcilla, M. Antonietti, *RSC Adv.* **2014**, *4*, 26981.

[21] N. Fechler, T. P. Fellinger, M. Antonietti, *Adv. Mater.* **2013**, *25*, 75.

[22] J. Kossmann, R. Rothe, T. Heil, M. Antonietti, N. López-Salas, *J. Colloid Interface Sci.* **2021**, *602*, 880.

[23] J. Kossmann, M. L. Ortíz Sánchez-Manjavacas, H. Zschiesche, N. V. Tarakina, M. Antonietti, J. Albero, N. López-Salas, *J. Mater. Chem. A* **2022**, *10*, 6107.

[24] K. A. Cychosz, R. Guillet-Nicolas, J. García-Martínez, M. Thommes, *Chem. Soc. Rev.* **2017**, *46*, 389.

[25] M. Thommes, K. Kaneko, A. V. Neimark, J. P. Olivier, F. Rodriguez-Reinoso, J. Rouquerol, K. S. W. Sing, *Pure Appl. Chem.* **2015**, *87*, 1051.

[26] B. Babinszki, E. Jakab, V. Terjék, Z. Sebestyén, G. Várhegyi, Z. May, A. Mahakhant, L. Attanatho, A. Suemanotham, Y. Thanmongkhon, Z. Czégény, *J. Anal. Appl. Pyrolysis* **2021**, *155*, 105069.

[27] F. O. Rice, R. E. Vollrath, *Proc. Natl. Acad. Sci.* **1929**, *15*, 702.

[28] S. Rat, A. Chavez-Sanchez, M. Jerigová, D. Cruz, M. Antonietti, *ACS Appl. Polym. Mater.* **2021**, *3*, 2588.

[29] S. M. Mitchell, K. A. Niradha Sachinthani, R. Pulukkody, E. B. Pentzer, *ACS Macro Lett.* **2020**, *9*, 1046.

[30] D.-I. B. Rumpf, *Thermochemical Data of Pure Substances*, **1997**.

[31] A. Banerjee, M. W. Kanan, *ACS Cent. Sci.* **2018**, *4*, 606.

[32] G. Singh, J. Lee, A. Karakoti, R. Bahadur, J. Yi, D. Zhao, K. Albahily, A. Vinu, *Chem. Soc. Rev.* **2020**, *49*, 4360.

[33] A. C. Dassanayake, M. Jaroniec, *J. Mater. Chem. A* **2017**, *5*, 19456.

[34] C. Chen, H. Huang, Y. Yu, J. Shi, C. He, R. Albilali, H. Pan, *Chem. Eng. J.* **2018**, *353*, 584.

[35] J. Kossmann, D. Piankova, N. V. Tarakina, J. Heske, T. D. Kühne, J. Schmidt, M. Antonietti, N. López-Salas, *Carbon* **2021**, *172*, 497.

[36] W. Cai, J. Ding, Y. He, X. Chen, D. Yuan, C. Chen, L. Cheng, W. Du, H. Wan, G. Guan, *Energy and Fuels* **2021**, *35*, 8857.

[37] A. Altwala, R. Mokaya, *Energy Adv.* **2022**, *1*, 216.

[38] C. Wang, L. Li, J. G. Bell, X. Lv, S. Tang, X. Zhao, K. M. Thomas, *Chem. Mater.* **2015**, *27*, 1502.

[39] B. Liu, S. Yao, X. Liu, X. Li, R. Krishna, G. Li, Q. Huo, Y. Liu, *ACS Appl. Mater. Interfaces* **2017**, *9*, 32820.

[40] L. Yang, X. Cui, Y. Zhang, Q. Wang, Z. Zhang, X. Suo, H. Xing, *ACS Sustain. Chem. Eng.* **2019**, *7*, 3138.

[41] L. Lei, Y. Cheng, C. Chen, M. Kosari, Z. Jiang, C. He, *J. Colloid Interface Sci.* **2022**, *612*, 132.

[42] R. Kodasma, J. Fermoso, A. Sanna, *Chem. Eng. J.* **2019**, *358*, 1351.

[43] S. K. Das, X. Wang, Z. Lai, *Micropor. Mesopor. Mater.* **2018**, *255*, 76.

[44] S. K. Das, X. Wang, M. M. Ostwal, Y. Zhao, Y. Han, Z. Lai, *Chem. Eng. Sci.* **2016**, *145*, 21.

[45] H. Ma, H. Ren, X. Zou, S. Meng, F. Sun, G. Zhu, *Polym. Chem.* **2014**, *5*, 144.

[46] S. Khodabakhshi, M. Taddei, J. A. Rudd, M. J. McPherson, Y. Niu, R. E. Palmer, A. R. Barron, E. Andreoli, *Carbon* **2021**, *173*, 989.

[47] Z. Zhang, Z. P. Cano, D. Luo, H. Dou, A. Yu, Z. Chen, *J. Mater. Chem. A* **2019**, *7*, 20985.

[48] V. Presser, J. McDonough, S. H. Yeon, Y. Gogotsi, *Energy Environ. Sci.* **2011**, *4*, 3059.

[49] D. Saha, M. J. Kienbaum, *Microporous Mesoporous Mater.* **2019**, *287*, 29.

[50] Y. Liu, J. Wilcox, *Environ. Sci. Technol.* **2012**, *46*, 1940.

[51] J. Li, K. Zhang, Y. Zhao, C. Wang, L. Wang, L. Wang, M. Liao, L. Ye, Y. Zhang, Y. Gao, B. Wang, H. Peng, *Angew. Chem. Int. Ed.* **2021**, *134*, e202114612.

Chapter 3 Cesium carboxylates as precursors for high-yield synthesis of porous carbons[2]

3.1 Breaking the trade-off between carbon yield and surface area

Bottom-up construction of porous carbons from small molecular precursors (*e.g.,* carbohydrates, carboxylic acids) offers a flexible and direct method to design bulk compositions and control porosity of final materials. The use of molecular precursor also ensures structural homogeneity in the obtained materials, showing distinct advantages over using macromolecule precursors. These materials serve as good model materials to study fundamental problems and exhibit promising performance in practical applications. Nonetheless, when starting from molecular precursors, conventional activation methods, using K and Na hydroxides as activation agents, suffer from low carbon yields (< 20%) and poor control over composition and porosity of the final materials, especially when targeting high SSAs (> 2000 $m^2 \cdot g^{-1}$). These issues arise due to intensive decomposition/evaporation/sublimation of molecular precursors and the formation of nanopores by etching processes.[1–3]

In **Chapter 2**, we showed that by heating solely CsAc between 500 and 800 °C, Cs ions effectively catalyze the condensation of acetate groups and facilitate the activation of carbon frameworks, yielding porous carbon with a carbon yield of 10% and an SSA of up to 2936 $m^2 \cdot g^{-1}$ at 800 °C, in contrast to much lower yields and SSAs in the cases of KAc and NaAc. However, the high cost of CsAc (about 100 $€ \cdot kg^{-1}$) and the suboptimal carbon yield (10%, due to the decomposition of acetates) largely hinder scale-up applications of this method. Further, the impact of Cs on the condensation and activation of carbon frameworks remains elusive, necessitating further investigation into the evolution of Cs species with temperature and their interactions with carbonaceous networks.

In **Chapter 3**, we further increase carbon yields to 25% while keeping high SSAs of about 3000 $m^2 \cdot g^{-1}$ through rational structural design of self-templating precursors, involving increasing the number of carbon atoms and introducing double bonds into precursor molecules. Meanwhile, the

---

[2] Results of this section are adapted from the original work with permission of the authors: Jiaxin Li, Yaolin Xu, Pengzhou Li, Antje Völkel, Fernando Igoa Saldaña, Markus Antonietti, Nieves López-Salas, Mateusz Odziomek, Beyond Conventional Carbon Activation: Creating Porosity without Etching using Cesium Effect, *Adv. Mater.* **2024**, 202311655

use of low-cost carboxylic acids (< 20 €·kg^{-1}) and Cs_2CO_3 (< 20 €·kg^{-1}) reduces the production cost and facilitates industrial applications of resulting carbon materials. Further, this chapter sheds light on the unconventional role of Cs species, which act as efficient electron injection and activating agents throughout the framework formation and pore development of carbon materials. Instead of conventional etching process, Cs ion intercalation is identified as the primary activation mechanism for pore formation. This chapter finally demonstrates the potential applications of porous carbons as cathodes in both aqueous Zn-ion capacitors and aprotic Na-ion capacitors showing high capacity and cycling stability.

3.2 Structures and microstructures of cesium carboxylates-derived carbon materials

Maleic acid (MA) is chosen as a model molecular precursor due to its easy availability from biomass and low cost.[4] With its four sp^2 carbon atoms and a C=C bond, MA is favorable for the formation of polymeric and, subsequent carbonaceous networks. However, direct pyrolysis of MA at atmospheric pressure does not result in any carbon material, as MA either sublimates, evaporates, and/or decomposes into gaseous products around 137 °C (***Figure 3.1a***). In comparison, the dicesium salt of MA, denoted as Cs_2MA (CsOOC-CH=CH-COOCs), produced porous carbon with a high carbon yield of 25% and an SSA of 3008 m^2·g^{-1} upon condensation at 800 °C (***Figure 3.1b*** and ***c***, ***Table 3.1***), surpassing other strategies as shown in ***Figure 3.1d***.[1,5–13] Simultaneously achieving a high carbon yield and a large SSA based on molecular precursors is uncommon, primarily because nanopores typically form at the expense of carbon atoms in a conventional activation process based on etching.[1–3,14,15] In addition, there is a competition between precursor decomposition/sublimation/volatilization and entering into the carbon network during heating. In comparison, using a monosalt precursor (HOOC-CH=CH-COOCs, Cs_1MA) gives a carbon yield of 13% and an SSA of 2481 m^2·g^{-1}, while dipotassium salt (K_2MA) only leads to a 4% carbon yield and an SSA of 1957 m^2·g^{-1}, much lower than that of Cs_2MA. The significant differences between Cs and K salts emphasize the impact of Cs on framework formation and pore development.

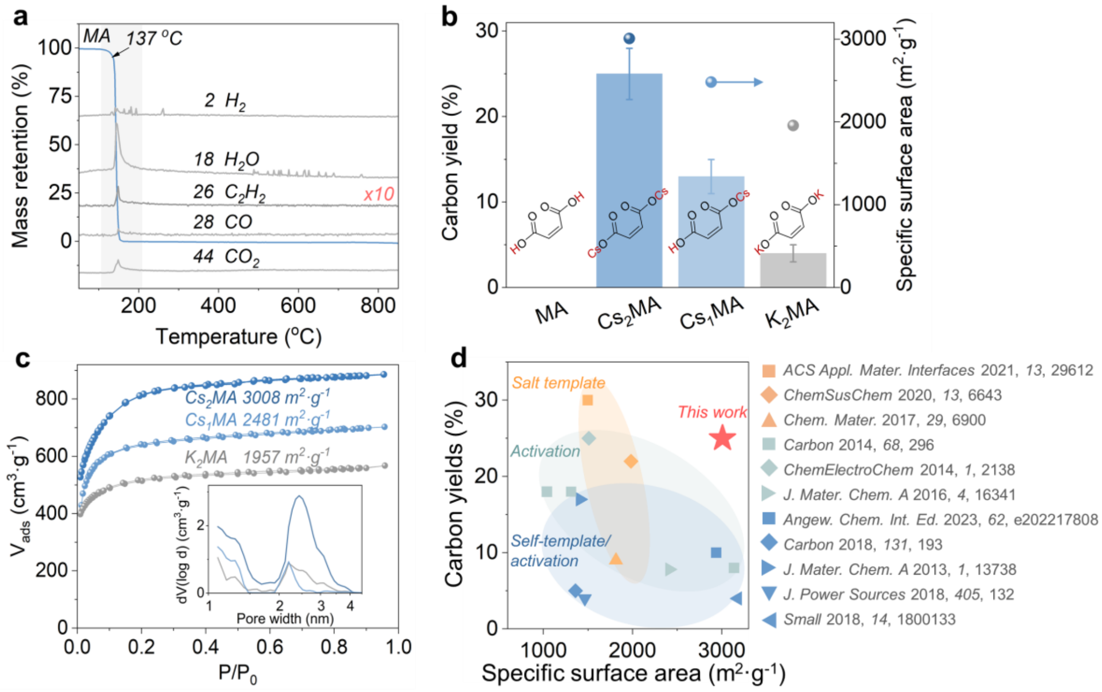

Figure 3.1. (a) TGA-MS curves of MA under helium; (b) carbon yields and SSAs; (c) N_2 sorption isotherms at 77 K (inset, pore size distributions) of porous carbons obtained from Cs_2MA, Cs_1MA, and K_2MA; (d) carbon yields and SSAs of porous carbons derived from Cs_2MA and other strategies starting from molecular precursors.

Table 3.1. Compositions and porosities of condensed products obtained at different conditions.

T (°C)	Precursor	Salt	C[a] (wt%)	H[a] (wt%)	O[a] (wt%)	Cs[b] (wt%)	SSA[c] ($m^2·g^{-1}$)	V_{Micro}[d] ($cm^3·g^{-1}$)	V_{Meso}[d] ($cm^3·g^{-1}$)	CO_2 uptake[e] ($mmol·g^{-1}$)	Carbon yield[f] (%)
800	Cs_2MA	-	92.9	0.6	4.8	0.3	3008	0.84	0.32	-	25
	Cs_1MA	-	88.5	1.1	9.4	0.1	2481	0.70	0.24	-	13
	K_2MA	-	87.7	1.1	11.2	-	1957	0.64	0.17	-	4
450	MA	Cs_2CO_3	83.6	3.0	16.4	0.1	891	0.30	0.10	4.0	28
500			85.0	3.7	15.1	0.1	1410	0.50	0.07	6.1	27
600			82.8	1.7	13.5	0.1	1988	0.72	0.05	9.0	26
700			87.1	1.5	11.5	0.1	2351	0.83	0.05	8.3	24
800			93.9	0.4	4.3	0.1	3066	0.88	0.38	8.1	22
800	Fumaric acid	Cs_2CO_3	92.9	0.5	5.2	0.1	2880	0.82	0.36	6.7	22
	Succinic acid		87.9	1.0	4.5	0.1	2710	0.67	0.64	5.7	10
	Acrylic acid		93.1	0.5	6.4	0.1	2604	0.88	0.12	9.8	18

[a] C, H, and O content were determined from the elemental combustion analysis. [b] Metal contents were measured from the ICP-OES. Since the content of C/H, O, and Cs was measured using different modes/methods, the mass ratio sum of all the above elements may not always equal 100%. [c] The SSAs were evaluated in P/P_0 from 0.05 to 0.25 using the BET equation. [d] The pore size distributions were calculated from N_2 adsorption/desorption isotherms at 77 K using the QSDFT method. [e] The CO_2 uptake was obtained at 273 K and 100 kPa. [f] The carbon yields were determined by comparing the final material mass to either the mass of the initial precursor or the mass of organic species in the self-templating precursor (Cs_2MA, Cs_1MA, or K_2MA).

However, Cs_2MA is not commercially available and must be synthesized. To simplify the process for non-chemists, we utilize the acidic properties of carboxylic acids. MA is a stronger acid (pK_{a1} of 1.9 and pK_{a2} of 6.1) than carbonic acid (pK_{a1} of 6.8 and pK_{a2} of 9.9). Mixing MA with Cs_2CO_3 will initiate a typical exchange reaction between the stronger acid (MA) and the salt of the weaker acid (Cs_2CO_3), generating the salt of a strong acid (Cs_2MA) and a weak acid (H_2CO_3). This reaction will take place between 100 and 200 °C, close to the melting points of MA (to be discussed later), while the generated H_2CO_3 instantly decomposes into H_2O and CO_2 leaving the reaction. Consequently, in the subsequent study, MA and Cs_2CO_3 are mixed in a mass ratio of 1:10 (corresponding to a molar ratio of 1:3.6, ensuring complete conversion of MA), heated between 450 and 800 °C, washed, and dried to obtain the resulting products. The products were named as MC-T, where T represents the condensation temperature.

The resulting carbonaceous materials showed notably higher carbon yields (28−22%) than those previously reported porous carbons derived from molecular precursors (***Figure 3.2a***). Elemental combustion analyses point out a significant decrease in oxygen content from 16.4 to 4.3 wt% and hydrogen from 3.0 to 0.4 wt% between MC450 and MC800 (***Figure 3.2a***), which correlates well with the reduction in the reaction yield. Importantly, the products obtained below 600 °C reveal a high oxygen content of 16.4−13.5 wt%, which can play an important role in the adsorption and energy storage/conversion applications. The amount of Cs is below 0.1 wt% for all products according to the results of ICP measurements. FT-IR spectrum of MC450 (***Figure 3.2b***) shows signals of C=O at 1690 cm^{-1}, C=C at 1560 cm^{-1}, and a broad band spanning 1300−950 cm^{-1} ascribed to C-O groups, indicating the formation of a carbon-oxygen framework. Notably, the spectrum of MC450 is flat at 3300−2700 cm^{-1}, the region related to C-H and O-H bonds. This implies the formation of a highly conjugated carbon framework, unusual for a temperature as low as 450 °C. At higher temperatures, the intensity of bands between 1700 and 900 cm^{-1} gradually weakens and eventually disappears at 800 °C, indicating the simultaneous heteroatom removal and progressing carbon condensation.

XRD patterns (***Figure 3.2c***) show broad and low-intensity (002) diffraction peaks, typical for turbostratic carbonaceous structures. The (002) peak of MC450 is centered at 22.1°, slightly shifts to a higher angle of 22.5° for MC600, and returns to a lower angle (21.1°) for MC800. This indicates that the structure first becomes more compact at 600 °C and then opens up again at 800 °C. The large intensity increase of low-angle scattering below 10° for MC700 and MC800 is characteristic of microporous materials with high SSAs.[16] The Raman spectra exhibit two broad bands typically denoted as D (breathing mode of sp^2 carbon atoms in aromatic rings at defect sites) and G bands (C=C bonds) (***Figure 3.2d***). While there is no noticeable difference in the shape or intensity of the D and G bands, the D band significantly shifts to lower wavenumbers from 1346 cm^{-1} for MC450 to 1330 cm^{-1} for MC600, followed by a shift back to 1348 cm^{-1} for MC800. Schuepfer *et al.* showed that the position of the D band is a good indicator of the lateral size of conjugated domains in disordered carbons.[17] This trend aligns with XRD findings that MC600 has the most compact and ordered structure.

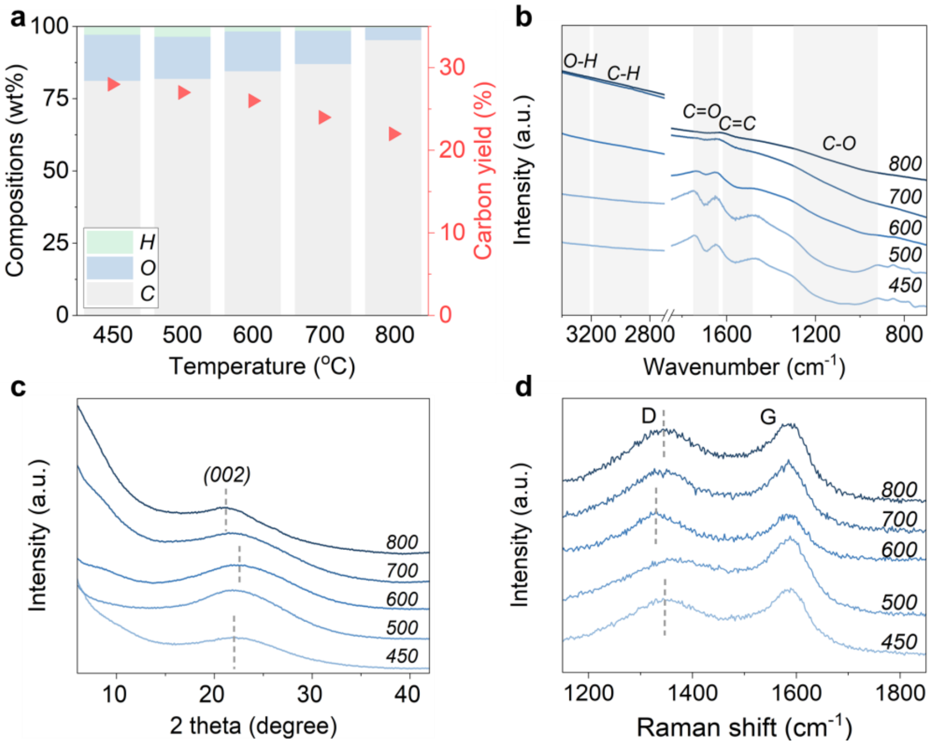

Figure 3.2. Chemical structures of porous carbons obtained from MA and Cs_2CO_3 at 600 and 800 °C. (a) Elemental compositions and carbon yields; (b) infrared spectra; (c) XRD patterns; (d) Raman spectra.

TEM images of MC600 and MC800 depict macroscopically homogeneous layers (***Figure 3.3***). The HR-TEM images of MC600 show a combination of disordered sp^2 carbon fringes and short but locally organized stacked graphitic layers that take random orientations to each other. The interlayer spacing is measured between 0.37 and 0.41 nm, consistent with that calculated value from XRD analysis (0.39 nm). The HR-TEM image of MC800 shows a more disordered structure with less pronounced local stacking, which is in line with XRD and Raman analysis.

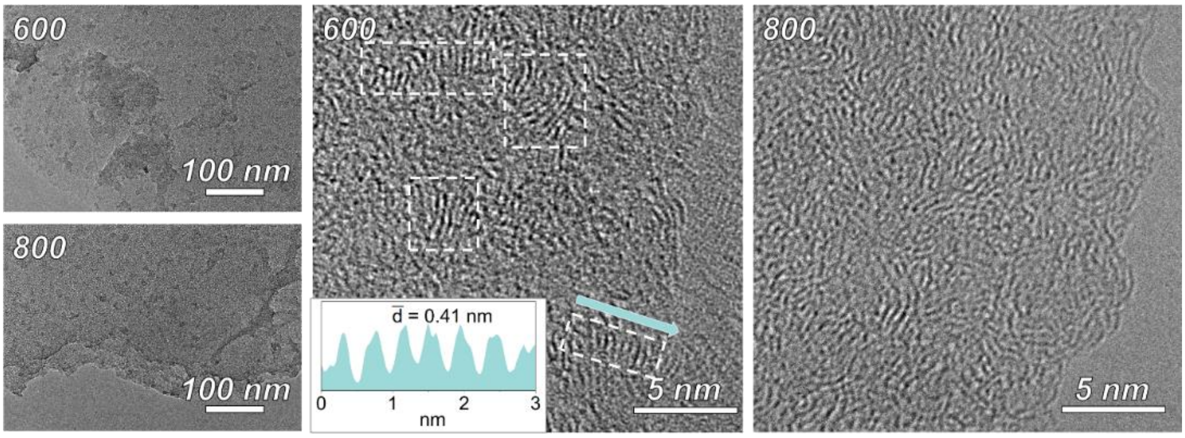

Figure 3.3. TEM and HR-TEM images of porous carbons obtained from MA and Cs_2CO_3 at 600 and 800 ºC.

N_2 sorption measurements were performed at 77 K to investigate the pore structure of the carbonaceous products (***Figure 3.4a***). The samples feature Type I(b) isotherms with a strong N_2 uptake at low relative pressures ($P/P_0 < 0.1$), typical for micropores, and a plateau above $P/P_0 = 0.2$.[18,19] The calculated Brunauer-Emmett-Teller (BET) SSA and micropore volume of samples between 450 and 800 ºC increases from 891 to 3066 $m^2 \cdot g^{-1}$ and from 0.30 to 0.88 $cm^3 \cdot g^{-1}$, respectively. The pore size distributions are depicted in ***Figure 3.4b*** and summarized in ***Table 3.1***. While the samples between 450 and 700 ºC show almost only microporosity (pore width < 2 nm), MC800 contains a second population of pores with sizes at 2−4 nm. Ar sorption measurements at 87 K with high resolution at low partial pressures (P/P_0 around 10^{-6}) were conducted to assess the micropore size distributions of the products (***Figure 3.4 c, d***). Between 450 to 700 ºC, the products exhibit an increase in ultramicropores (pore width < 0.7 nm) (***Figure 3.4e***). At 800 ºC, the ultramicropore volume decreases, and the volume of larger micropores (pore width > 1 nm) increases, possibly due to ultramicropore merging or expansion.

Moreover, the samples obtained from 450 to 600 ºC exhibit an increase in CO_2 uptake at 273 K, reaching 9.0 $mmol \cdot g^{-1}$ for MC600, and the amount of CO_2 adsorbed slightly decreases to 8.1 $mmol \cdot g^{-1}$ for MC800 (***Figure 3.4f***, summarized in ***Table 3.1***). These values are competitive to the reported top-in-class CO_2 adsorbents,[20–22] highlighting the potential of Cs-mediated porous carbons in CO_2 adsorption or further catalytic conversion. Such high uptakes originate primarily from very high micropore volumes, especially ultramicropores (pore width < 0.7 nm) which favor strong interactions between CO_2 molecules and neighboring pore walls.[23,24] Besides, the electron-rich oxygen sites can interact with electron-deficient carbon atoms in CO_2 molecules, promoting

CO_2 adsorption by Lewis acid-base interaction.[25–29] Therefore, MC600 shows the highest CO_2 uptake, due to its highest ultramicropore volume and maintained high oxygen content of 13.5 wt%.

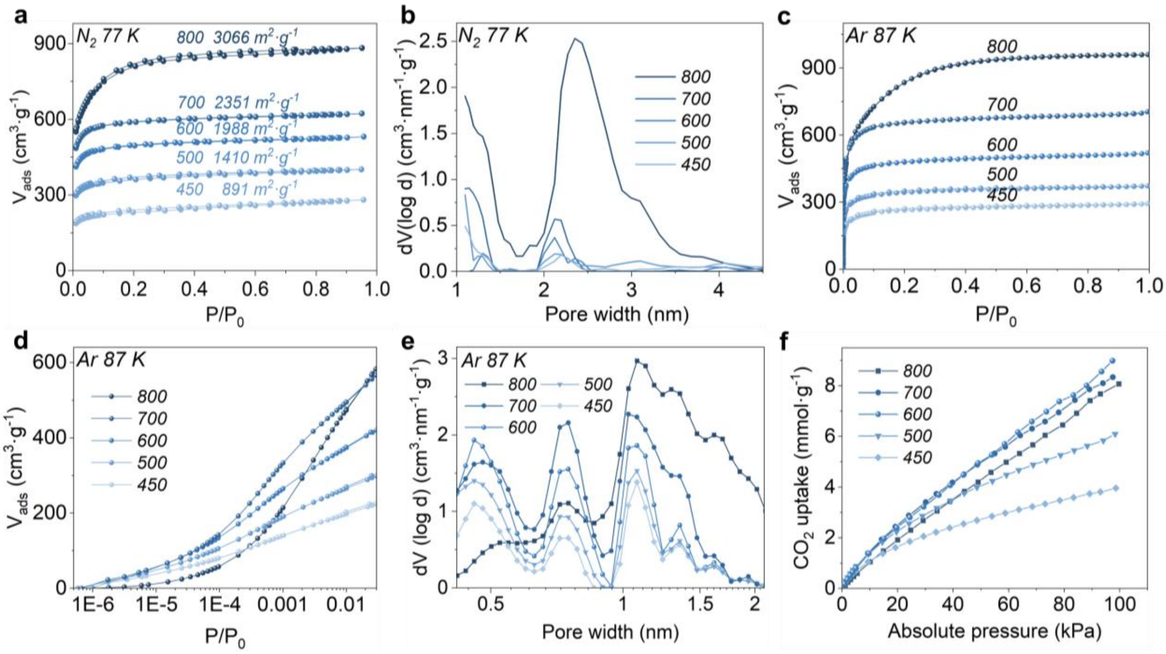

Figure 3.4. Gas physisorption measurements of porous carbons obtained from MA and Cs_2CO_3 between 450 and 800 °C. (a) N_2 sorption isotherms at 77 K; (b) pore size distributions and cumulative pore volumes calculated from N_2 sorption isotherms; (c) Ar sorption isotherms at 87 K; (d) the enlarged parts at low partial pressures; (e) micropore size distributions calculated from Ar sorption isotherms at 87 K; (f) CO_2 uptake at 273 K.

3.3 Thermodynamic transformation of Cs_2MA and Cs_2CO_3

To get further insights into the mechanism of the process and the structural rearrangements occurring, TGA-MS and *in situ* XRD were performed. MA: Cs_2CO_3 mixtures of 1:1 and 1:10 mass ratios were used to decouple the signals from *in situ* formed Cs maleate and bulk Cs_2CO_3. TGA curves of a 1:1 mixture (***Figure 3.5a***) show a mass loss of 44% between 115 and 150 °C, accompanied by the release of CO_2, CO, H_2O, and H_2. This is the overlapping decomposition of carbonic acid and the sublimation/decomposition of MA excess. Further mass loss at 230 °C with the generation of CO_2, H_2O, and H_2 indicates the onset of the decomposition of cesium maleate and condensation of organics, which continues up to 400 °C. At this stage, the evolution of CO_2 and H_2 occurs as a result of condensation and aromatization reactions. Notably, the most severe aromatization starts at about 570 °C and continues to about 785 °C with strong H_2 evolution. It is important to note that the mass loss from the carbon network at this temperature range is minimal, as indicated by the TGA, differential thermal gravimetric curve, and the calculated carbon yields.

At around 700 °C, the strong mass loss is related to the evaporation of Cs species with the helium flow, as discussed earlier in the case of CsAc.

In situ XRD patterns of the 1:1 mixture (***Figure 3.5b***) reveal the formation of Cs maleates at 200 °C with the disappearance of peaks related to MA and Cs_2CO_3. The decomposition of Cs maleate at 300 °C is signaled by the disappearance of the diffraction peaks. In the meantime, no crystalline phase of Cs is formed which might indicate the formed poorly crystalline phases are homogenously distributed within the formed carbonaceous network. There is a possibility that the formed oxide or metallic phase is molten as these are low melting point phases. Notably, no XRD peak is observed from 400 to 800 °C. The broad hump at around 18° is to be attributed to the Kapton window of the high-temperature chamber. During the cooling stage, several new peaks appear below 600 °C owing to the recrystallization of Cs oxides or carbonates. However, we could not unambiguously assign them due to the rich structural complexity of Cs oxides and carbonates.

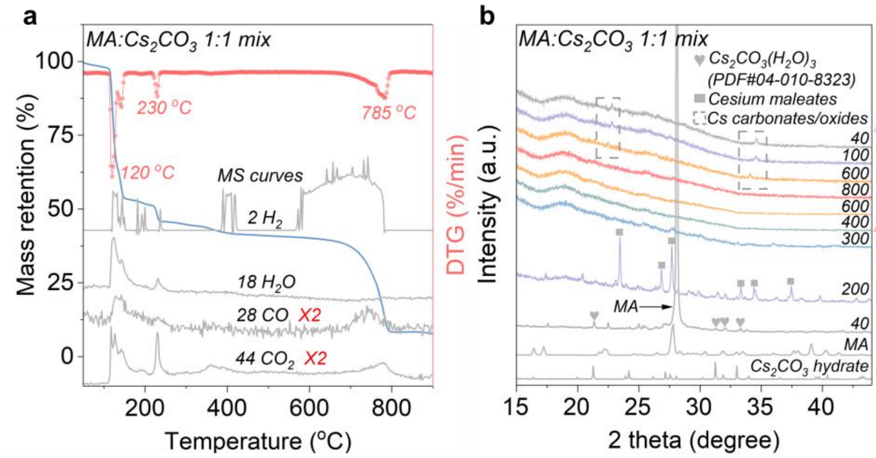

Figure 3.5. (a) TGA-MS curves under helium and (b) *in situ* XRD patterns of 1:1 mass ratio mixture of MA and Cs_2CO_3 under N_2. XRD patterns of Cs_2CO_3 and MA were provided for reference. Cs_2CO_3 is extremely hygroscopic and instantly converts into its hydrates in the air.

A similar TGA-MS pattern is observed for the 1:10 mixture (***Figure 3.6a***). However, the peaks corresponding to the evolution of carbon species are hidden due to the large excess of Cs_2CO_3. The onset of the most intense mass loss (about 77% in total) is at about 530 °C, which corresponds to the beginning of Cs_2CO_3 decomposition to Cs_2O and CO_2. Theoretically, the released CO_2 should only account for 13.5% of the mass of Cs_2CO_3, much lower than the real mass loss, which suggests that the *in situ* generated Cs_2O is not stable at this temperature. Cs_2O has been reported to undergo complex disproportionation reactions generating Cs_2O_2, CsO_2, and Cs metal.[30]

Therefore, the sharp mass loss is attributed to the evaporation of Cs oxides and metal (boiling point: 671 ºC) within the helium flow. The notable difference in the temperature onset of mass loss for Cs species evaporation between 1:1 (670 ºC) and 1:10 (530 ºC) ratio samples suggests that Cs_2MA might not decompose into carbonate but into other Cs species like Cs oxides, suboxides, and metal. These formed Cs species could potentially be stabilized within the carbon networks, as intercalated compounds. In the case of the *in situ* XRD experiment with a 1:10 mixture (***Figure 3.6b***), we can follow the transformation of bulk Cs_2CO_3 as its scattering cross-section is orders of magnitude higher than that of carbon. The peaks from crystalline Cs_2CO_3 remain visible up to 700 ºC, with a slight shift to lower angles due to the thermal expansion of the unit cell at high temperatures. At 800 ºC, no peak is observed due to Cs_2CO_3 melting and decomposition. Similar to the 1:1 mixture, the appearance of new peaks during cooling below 500 ºC is attributed to the recrystallization of Cs oxides or residual carbonates during cooling.

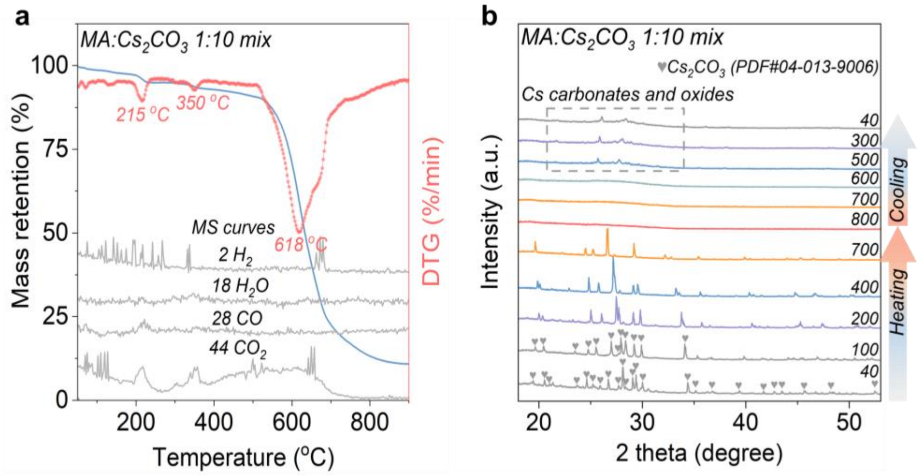

Figure 3.6. (a) TGA-MS curves under helium and (b) *in situ* XRD patterns of 1:10 mass ratio mixture of MA and Cs_2CO_3 under N_2.

3.4 The effect of Cs on condensation and activation

Based on the analysis above, we can summarize the effect of Cs on the formation of a porous carbonaceous framework. Initially, around 130 ºC, MA melts and reacts with Cs_2CO_3, forming cesium maleates (***Figure 3.7a***). As the temperature rises above 200 ºC, cesium maleates undergo complex polymerization, decomposition, cyclization, cross-linking, and concomitant aromatization reactions, which leads to the formation of a continuous oxo-carbon framework at temperatures as low as 400 ºC.

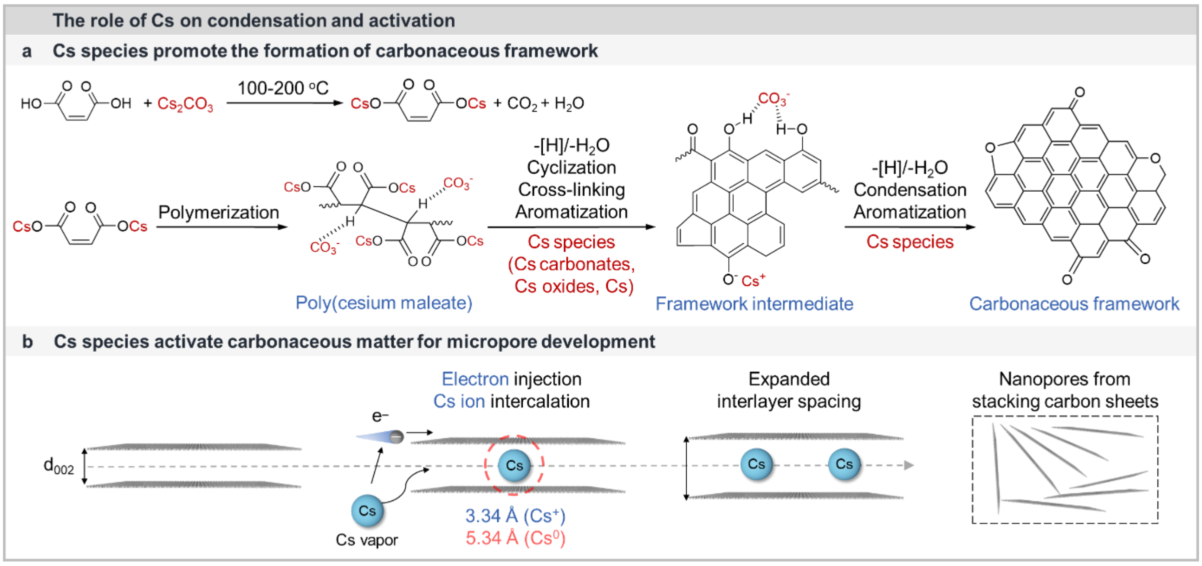

Figure 3.7. The role of Cs species in (a) promoting the formation of carbonaceous framework, and (b) injecting electrons and intercalating into graphitic layers to form slit nanopores. Diameters of Cs atom and ion are marked.

In the beginning, the oligomeric species of poly (cesium maleate) form due to the presence of a double bond within the MA molecule, which is confirmed by the matrix-assisted laser desorption/ionization-time of flight analysis (***Figure 3.8a***). Notably, at 400 ºC, the carbon framework is already highly conjugated as FT-IR analysis did not detect C-H and O-H groups (***Figure 3.8b***). This supports the catalytic effect of Cs ions on condensation, especially given that using K, Na, and Li does not yield the same effect. This is also supported by the optical photos of the suspensions containing condensed products obtained from MA and various alkali metallic carbonates (***Figure 3.8c***). MC300 is light yellow, which turns to dark brown for MC350, and MC400 is nearly colorless with visible black precipitates. Notably, the suspensions of MN and ML at 300 and 350 ºC are much lighter in color and lack precipitates. MK falls in between, showing noticeable color, and precipitates at 400 ºC. The trend suggests an increase in the degree of conjugation in the series from Li to Cs.

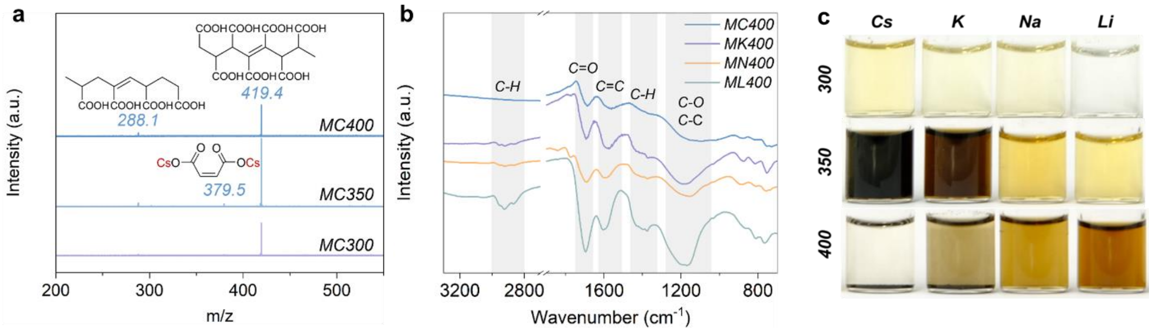

Figure 3.8. (a) Matrix-assisted laser desorption/ionization-time of flight analysis spectra of soluble species in deionized water extracted from the unwashed condensed products of 1:10 mass ratio mixture of MA and Cs_2CO_3 treated at 300, 350, and 400 °C; (b) infrared spectra of the condensed products obtained from MA and different alkali carbonates at 400 °C; (c) optical photos of the suspensions containing 10 mg of unwashed condensed products in 1 mL of deionized water.

Grasping the exact fate of Cs is difficult because Cs oxides and metals are highly reactive and have low melting points. During the condensation/crosslinking of the carbon network, Cs are homogeneously distributed as counter ions to oxygen functionalities and successively transformed into a mixture of poorly crystallized oxides, as typically happens to carboxylic salts.[26] Cs oxides are chemically not well-defined and undergo complex disproportionation reactions forming suboxides (*e.g.,* Cs_7O, Cs_4O, Cs_3O, and Cs_7O_2)[30–32] and even metallic Cs.[33,34] It is worth noting that such basic oxides easily capture CO_2-forming carbonates. All these Cs species are efficient electron-injection agents,[35] for instance, used in organic electronic devices due to their low work function.[36–38] It has been shown that oxidized Cs clusters have one of the lowest work functions, especially for Cs suboxides.[39] The layers of Cs oxides are deposited on different materials to decrease their work function.[40,41] Therefore, we speculate that, at elevated temperatures, Cs oxides can act as electron donors triggering faster polymerization, condensation reactions, and the aromatization of covalent networks. Meantime, the *in situ* formed clusters of Cs species serve as templates for creating the initial porosity.

Up to 600 °C, the carbon structure experiences further decomposition of oxygen functionalities and aromatization reactions releasing H_2. This process results in the formation of new pores (templated by Cs species) and graphitic domains, as evidenced by HR-TEM and XRD analyses. Beyond 600 °C, we observe a notable transformation: the graphitic domains diminish, and there is a shift in pore size distribution, with an increase in pores larger than 1 nm at the expense of smaller pores (pore width < 1 nm). We attribute this transformation to an intercalation mechanism.

As the temperature rises, Cs oxides/carbonates become more prone to form metallic species or suboxides. These Cs species have a remarkably high affinity for carbon, readily forming intercalation compounds such as CsC_8 and CsC_6. Notably, the formation energy of Cs intercalation compounds is significantly lower compared to other alkali metals, as documented in the literature.[42,43] These Cs species are capable of electron donation, inducing a negative charge on the carbonaceous layers and thereby causing repulsion between these layers. This effect increases the interlayer distance, facilitating the diffusion of Cs cations, which are sizably akin to the spacing in graphitic structures, as shown in ***Figure 3.7b***. Additionally, it is plausible that similar intercalation compounds may form through the interaction of Cs oxides with carbon.

Furthermore, at temperatures exceeding 500−600 °C, there is significant decomposition of carbonates into CO_2 and chemically undefined Cs oxides and suboxides,[30,40] which subsequently disproportionate into metallic Cs.[34] This process is corroborated by the pronounced mass loss of 77% observed in the TGA of a 1:10 mixture (attributed to evaporation of metallic Cs), as presented in Figure S6. The interlayer distances reported for Cs graphitic intercalation compounds typically range from 0.59 to 0.61 nm,[44,45] which are significantly larger than the interlayer spacing in MC600 (0.37−0.41 nm) determined by HR-TEM and the smallest fraction of ultramicropores (approximately 0.46 nm) identified by Argon sorption. At 800 ºC, the emergence of larger pores (pore width > 1 nm) at the expense of the smallest ones might serve as additional evidence of Cs intercalation. Besides, this micropore expansion could also be a result of the merging of the smallest pores, potentially occurring during the release of gases like CO or CO_2, especially considering the high oxygen loss from 11.5 to 4.3 wt% between 700 and 800 ºC.

This electron injection and ion intercalation mechanism is also supported by the discovery that Cs intercalation graphitic compounds have much higher electron density and in-plane electrical conductivity compared with pristine graphite.[46,47] Inspiringly, Zhu *et al.* recent study indicates that α-Li_3N significantly lowers the phase change temperature of graphite to 350 ºC due to electron injection from α-Li_3N into graphite.[48] This electron injection expands the interlayer spacing of graphite through increased Columbic repulsion among π electrons within graphitic layers. They also observed similar effects on promoting graphite phase transition with alkali metals like Li, Na, and K. These effects are primarily related to the low work function of Li_3N, Li, Na, and K.[48,49] Interestingly, Cs oxides and metal possess even lower work function values,[36] further supporting our proposal above.

The alkali metal intercalation mechanism has been already described for K. In the case of K, the presence of metallic K is postulated to occur by carbothermal reduction, *i.e.* it is coupled to C=O and CO_2 formation while the metallic K evaporates at temperatures above 800 °C.[50,51] For example, in the case of Cs, the mixture exhibits a distinct mass loss from *c.a.* 530 °C. In contrast, other mixtures initiate their mass loss above 700 °C, nearly over 200 °C higher than that required for Cs (***Figure 3.9a***).[52,53] This notable difference indicates that Cs_2CO_3 decomposes and Cs oxides/metal form at temperatures over 200 °C lower than others. This property significantly influences the activation process of carbon materials in the presence of Cs. At the same time, the formation of Cs suboxides may greatly facilitate the electron transfer and ion intercalation process. Besides, the Cs atom, being much bigger than the K atom, brings larger distortion into the carbon networks and results in higher SSAs.

This is exactly what we observed in the samples prepared between 450 and 800 °C. Cs-mediated carbons present higher SSAs (1410−3066 $m^2\cdot g^{-1}$) while retaining comparable or higher carbon yields (28−22%) than other alkali ion-mediated carbons (369−1439 $m^2\cdot g^{-1}$, 25−11%) from 450 to 800 °C (***Figure 3.9b***). This shows the remarkable effect of Cs species in boosting condensation and activation. Notably, MK800 presents a similar Type I(b) isotherm but a much lower sorption volume than that of MC800 (***Figure 3.9c***). This suggests that K species could act like Cs on condensation and activation but require higher temperatures. MN800 exhibits a combination of Type II and IV isotherms with an H3 hysteresis loop, indicating the existence of mesopores (pore width > 4 nm) and macropores. This is attributed to the lower miscibility of organics with Na_2CO_3, and the bigger salt clusters of Na_2CO_3 acting as templates to create additional mesopores due to an onset of phase de-mixing during condensation.[54]

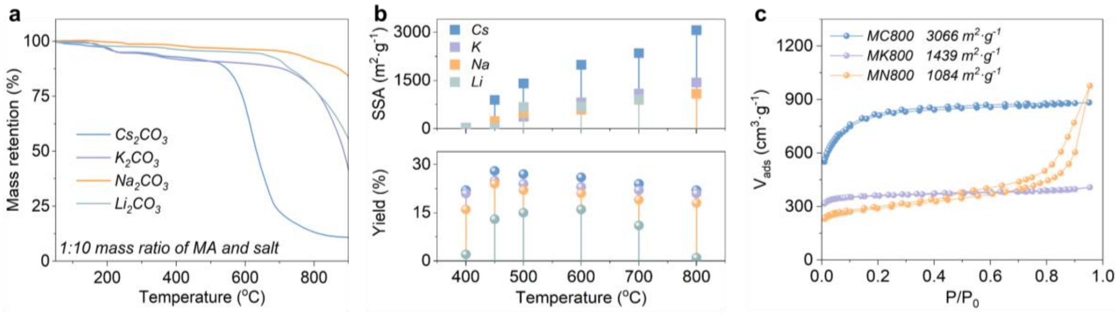

Figure 3.9. (a) TGA curves of 1:10 mass ratio mixtures of MA and various alkali metallic carbonates under helium; (b) carbon yield and SSA comparison of the condensation products obtained from MA and various alkali carbonates between 400 and 800 °C; (c) N_2 sorption isotherms at 77 K of MC800, MK800, and MN800.

Notably, the traditional activation process is inherently associated with chemical etching, wherein significant amounts of carbon atoms are taken away as the liberated gaseous carbon oxides using KOH, $ZnCl_2$, or steam at harsh temperatures. However, in this study, the reaction yields at temperatures of 450 and 800 °C are 28% and 22%, respectively, with oxygen content measured at 16.4 wt% and 4.3 wt%. This implies that the mass loss from 28% to 22% is primarily due to the liberation of CO_2 and CO from the carbonaceous networks. This phenomenon aligns with the thermal decomposition of oxygen-containing groups in carbonaceous materials [39] and occurs regardless of the presence of activating or templating agents.

To further validate this, MC450 was reheated at 800 °C in N_2. The treatment left carbon with 70% of the initial mass, resulting in a 20% overall carbon yield, similar to or slightly lower than that of MC800 (***Figure 3.10a***). Meanwhile, the SSA increases only to 1397 $m^2\cdot g^{-1}$ after thermal treatment, much lower than MC800 (3066 $m^2\cdot g^{-1}$) (***Figure 3.10b***). This indicates that Cs activation influences the porosity but not the yield. Therefore, we can speculate that Cs species do not engage in the conventional chemical etching of carbon structures, as is commonly observed with traditional activating agents such as KOH, NaOH, CO_2, or steam.[14,15]

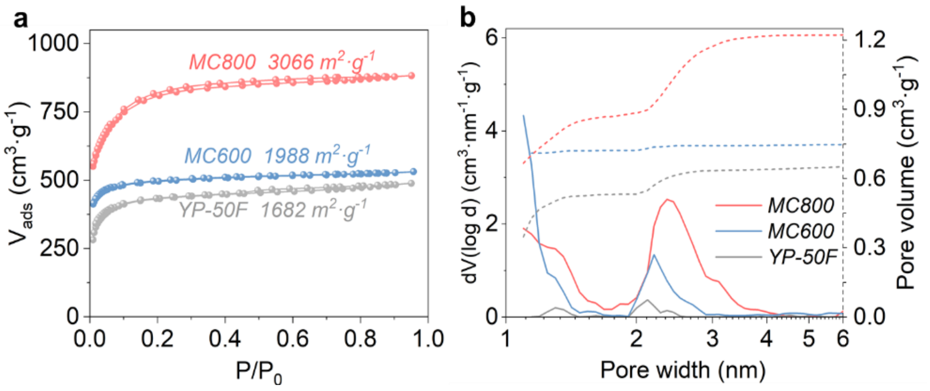

Figure 3.10. (a) Elemental compositions and overall carbon yields; (b) N_2 sorption isotherms at 77 K of MC450, MC450_800, and MC800. MC450_800 was obtained upon thermal treatment of MC450 at 800 °C in N_2 for 2 h.

3.5 Molecular design of porous carbons

The structures of molecular precursors play a crucial role in the yields and structures of the materials synthesized through bottom-up methods. To this end, we compared the yields, elemental compositions, and pore structures of carbon samples derived from the thermal condensation of fumaric acid, succinic acid, or acrylic acid as a precursor in the presence of Cs_2CO_3 (1:10 mass ratio) at 800 °C. CsAc-derived porous carbon is also added as a reference. Although fumaric acid has a higher melting point (T_m=287 °C) and weaker acidity (pK_{a1}=3.0, pK_{a2}=4.4) than that of MA (T_m=133 °C; pK_{a1}=1.9, pK_{a2}=6.1), the final carbons obtained from MA and fumaric acid exhibit almost identical yields and porosities (***Figure 3.11***). This similarity is likely influenced by ongoing isomerization reactions of fumaric acid during the heating stage, effectively generating the same active species as with MA. When the double bond is replaced by a single bond, as observed in succinic acid, the carbon yield decreases to 10%, even though the number of carbon atoms in the molecules remains the same. Meantime, the SSA is still high (2710 $m^2 \cdot g^{-1}$) but the pores are, on average, 1 nm larger, resulting in a higher contribution of mesopores. Removing one –COOH group, as in the case of acrylic acid, also leads to a lower carbon yield (18%) while maintaining a high SSA (2604 $m^2 \cdot g^{-1}$), but with a much lower contribution of mesopores. In the case of CsAc, the simultaneous removal of one –COOH and one double bond leads to an even lower carbon yield (10%) and an increase in the average pore size, with the formation of large mesopores of 10−40 nm. Minor changes in the molecule structure can influence the reaction pathway, and finally determine the yield, and more importantly, the porosities of the samples. It is worthwhile to mention that the selection of Cs salt is equally or even more important. For example, when treating a 1:10 mass ratio mixture of MA and CsCl at 800 °C, the yield is lower (10%) and only SSA of 1019 $m^2 \cdot g^{-1}$ is achieved. This implies the role of *in situ* generated Cs oxides and metal, all of which play a vital role in accelerating the condensation and activation processes.

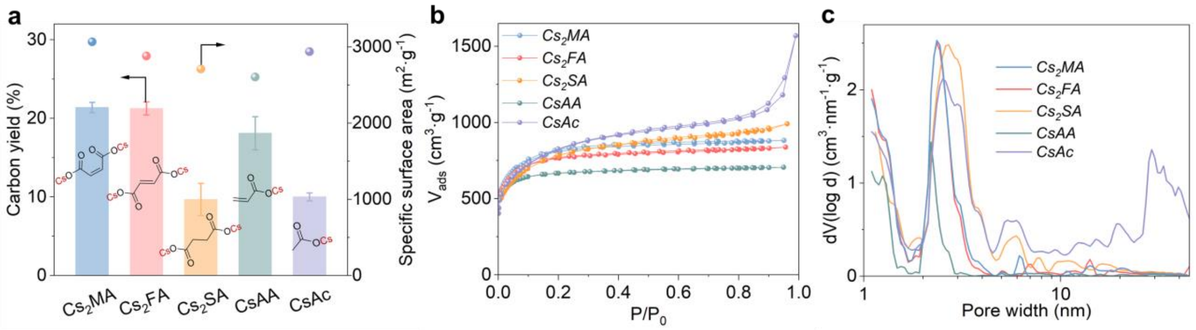

Figure 3.11. Molecular design of porous carbons. (a) Carbon yields and SSAs; (b) N_2 sorption isotherms at 77 K; (c) pore size distributions of porous carbons obtained from cesium salts of MA (Cs_2MA), fumaric acid (Cs_2FA), succinic acid (Cs_2SA), or acrylic acid (CsAA) or direct pyrolysis from CsAc at 800 °C.

3.6 Applications in Zn-ion and Na-ion capacitors

To showcase the potential applications of porous carbons, we fabricated Zn-ion capacitors with 2 M $ZnSO_4$ aqueous solution as an electrolyte, using MC800 for its high SSA of 3066 $m^2 \cdot g^{-1}$ and

MC600 for its high oxygen content (13.5 wt%) as cathodes. The commercial activated carbon YP-50F is used as a reference material for comparison (SSA of 1682 $m^2 \cdot g^{-1}$). The CV patterns of MC600 show a nearly rectangular shape with bumps at 10 $mV \cdot s^{-1}$ (***Figure 3.12a***). Despite its lower SSA, MC600 shows a larger cyclic voltammetry area than MC800, attributed to its higher functional oxygen content, which enhances interfacial contact with electrolytes and increases pseudocapacitance. Correspondingly, in Galvanostatic charge/discharge measurements, MC600 presents a higher specific capacity (capacitance) of 252 $mAh \cdot g^{-1}$ (567 $F \cdot g^{-1}$, based on a voltage window of 1.6 V) than that of MC800 (157 $mAh \cdot g^{-1}$, 356 $F \cdot g^{-1}$) (***Figure 3.12b***). Both, however, significantly outperform the commercial gold standard YP-50F (60 $mAh \cdot g^{-1}$, 135 $F \cdot g^{-1}$). The specific energy at the material level is very high at 204.8 $Wh \cdot kg^{-1}$, making it a strong competitor against standard faradaic battery cathodes. Even at a high current density of 10 $A \cdot g^{-1}$, MC600 maintains a specific capacity of 64 $mAh \cdot g^{-1}$ (144 $F \cdot g^{-1}$), corresponding to a specific energy of 51.2 $Wh \cdot kg^{-1}$. Notably, MC800 demonstrates high cycling stability with nearly 100% capacity retention after 100,000 cycles at 10 $A \cdot g^{-1}$ (***Figure 3.12c***), surpassing all the other top-in-class Zn-ion capacitors based on heteroatom-doped carbons, MXene, or metal oxides (***Figure 3.12d***).[55–65]

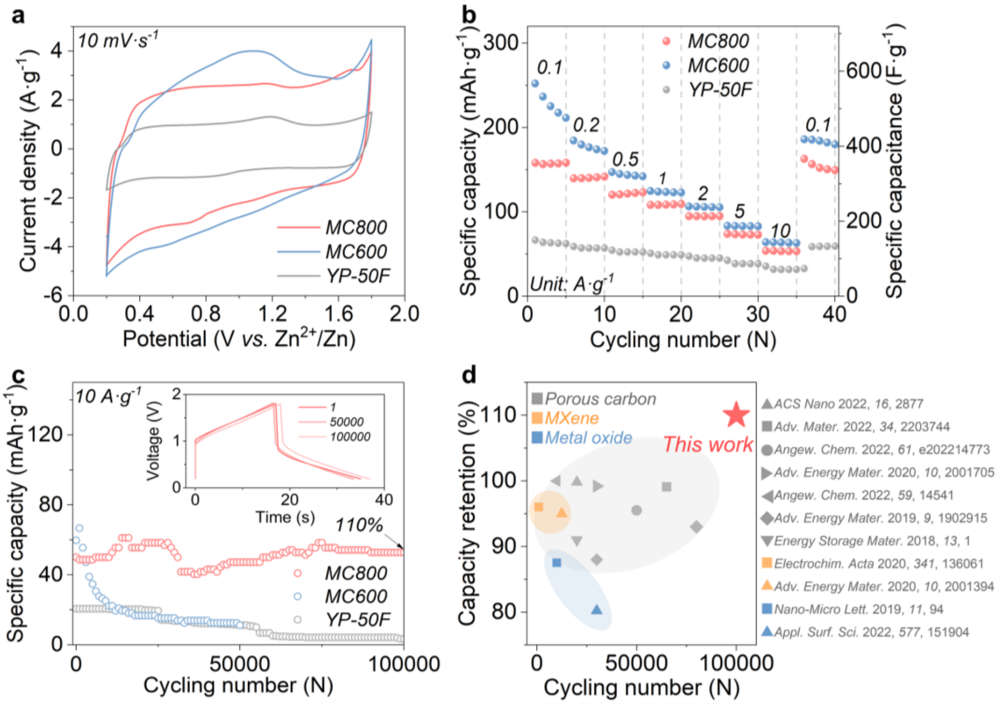

Figure 3.12. Electrochemical properties of Zn-ion capacitors based on MC800, MC600, or YP-50F as cathodes. (a) CV curves at 10 $mV \cdot s^{-1}$; (b) specific capacities and capacitances at different current densities; (c) cycling performance; (d) comparison of Zn-ion capacitors with the reported devices in literature.

Further, we evaluated the feasibility of MC800 and MC600 as porous cathodes of Na-ion capacitors in a half-cell configuration with Na foil as both the counter and reference electrode. The voltage window of 1.5−4.2 V *vs.* Na^+/Na was set in case of electrolyte decomposition or ion intercalation into the carbons. CV curves of MC800 exhibit a rectangle shape, indicative of electric double-layer behavior, overlaid with pseudocapacitive humps (***Figure 3.13a***). Different from their performances in Zn-ion capacitors, MC800 shows a higher specific capacity of 147 $mAh·g^{-1}$ than that of MC600 (115 $mAh·g^{-1}$) at 0.1 $A·g^{-1}$ and higher current densities (***Figure 3.13b***). We attributed this to the surface chemistry of MC800 of which the hydrophobic surface could have a better contact with electrolyte than that of MC600, thus unlocking more micropore surfaces that cannot be reached in the aqueous electrolyte. Besides, the mesoporous structure also provides fast ion transfer channels at high rates. Further, MC800 also delivers good cycling stability which can discharge/charge for 40,000 cycles at 10 $A·g^{-1}$ with a capacity retention of 25 $mAh·g^{-1}$ (***Figure 3.13c***). The high specific capacity and good cycling stability are comparable or even better than the reported performance of previous capacitors.[66–69] So far, our carbons have demonstrated the versatility and promising prospects for energy storage applications in various electrolyte systems.

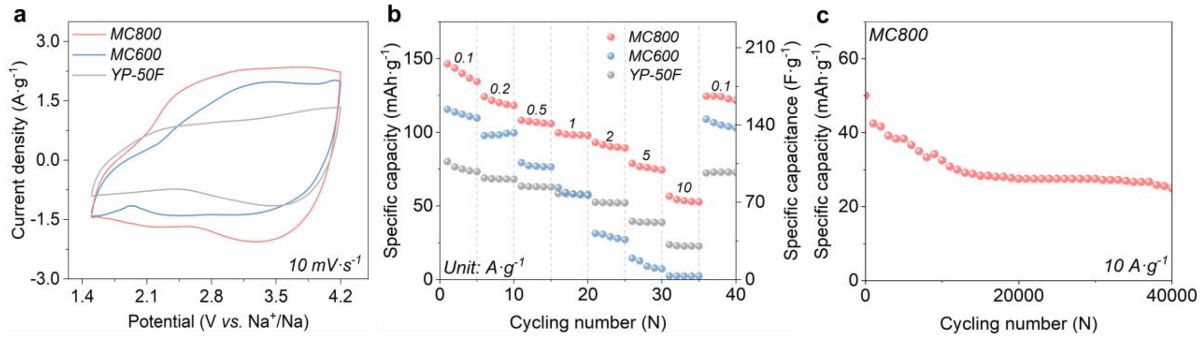

Figure 3.13. Electrochemical properties of Na-ion capacitors based on MC800, MC600, and YP-50F as cathodes. (a) CV curves at 10 $mV·s^{-1}$; (b) specific capacities and capacitances at varying current densities; (c) specific capacity with cycling number at 10 $A·g^{-1}$ of MC800.

In summary, in this chapter, we have introduced a straightforward and scalable approach for synthesizing porous carbons with high carbon yields exceeding 20% and high SSAs of *ca.* 3000 $m^2·g^{-1}$ through direct thermal treatment of Cs salts of low-cost carboxylic acids. Our study sheds light on the underlying reaction pathways and provides novel mechanistic insights into the “Cs effect” throughout the processes of framework formation and pore development in carbon materials. Cs species play different roles at different stages. Initially, they promote the condensation of organic species by accelerating dehydration processes. Subsequently, upon Cs reduction, they donate electrons to carbonaceous frameworks and intercalate into graphitic layers to form slit nanopores. Notably, the generated metallic Cs completely evaporated in the final synthesis stage through the gas phase, which could be potentially recycled from the condensation trap. The resulting porous carbons deliver high capacity and cycling stability as cathodes in both aqueous Zn-ion capacitors and aprotic Na-ion capacitors. Remarkably, the optimal performance of the materials is obtained at a relatively low synthesis temperature of 600 °C, contrasting with the higher temperatures required for commercial activated carbons (typically above 800 °C). Finally, the simplicity of both materials and procedures, coupled with the facile recovery of Cs salts, renders the entire process industrially viable and environmentally sustainable. Overall, our findings provide fresh insights into the unconventional roles of Cs in the traditional synthesis of porous carbons.

Reference

[1] S. Yu, H. Wang, C. Hu, Q. Zhu, N. Qiao, B. Xu, *J. Mater. Chem. A* **2016**, *4*, 16341.

[2] A. J. Romero-Anaya, M. Ouzzine, M. A. Lillo-Ródenas, A. Linares-Solano, *Carbon* **2014**, *68*, 296.

[3] X. Liu, M. Antonietti, *Carbon* **2014**, *69*, 460.

[4] R. Wojcieszak, F. Santarelli, S. Paul, F. Dumeignil, F. Cavani, R. V Gonçalves, *Sustain. Chem. Process.* **2015**, *3*, 9.

[5] I. K. Ilic, E. Lepre, N. López-Salas, *ACS Appl. Mater. Interfaces* **2021**, *13*, 29612.

[6] J. Kossmann, T. Heil, M. Antonietti, N. López-Salas, *ChemSusChem* **2020**, *13*, 6643.

[7] M. Sevilla, G. A. Ferrero, A. B. Fuertes, *Chem. Mater.* **2017**, *29*, 6900.

[8] M. Sevilla, L. Yu, C. O. Ania, M. M. Titirici, *ChemElectroChem* **2014**, *1*, 2138.

[9] J. Li, J. Kossmann, K. Zeng, K. Zhang, B. Wang, C. Weinberger, M. Antonietti, M. Odziomek, N. López-Salas, *Angew. Chem. Int. Ed.* **2023**, *62*, e202217808.

[10] M. Sevilla, G. A. Ferrero, N. Diez, A. B. Fuertes, *Carbon* **2018**, *131*, 193.

[11] M. Sevilla, A. B. Fuertes, *J. Mater. Chem. A* **2013**, *1*, 13738.

[12] S. Yu, N. Sun, L. Hu, L. Wang, Q. Zhu, Y. Guan, B. Xu, *J. Power Sources* **2018**, *405*, 132.

[13] Y. Zhang, Q. Ma, H. Li, Y. W. Yang, J. Luo, *Small* **2018**, *14*, 1800133.

[14] X. Y. Zhao, S. S. Huang, J. P. Cao, X. Y. Wei, K. Magarisawa, T. Takarada, *Fuel Process. Technol.* **2014**, *125*, 251.

[15] Q. Cao, K. C. Xie, Y. K. Lv, W. R. Bao, *Bioresour. Technol.* **2006**, *97*, 110.

[16] Y. Zhu, S. Murali, M. D. Stoller, K. J. Ganesh, W. Cai, P. J. Ferreira, A. Pirkle, R. M. Wallace, K. A. Cychosz,

M. Thommes, D. Su, E. A. Stach, R. S. Ruoff, *Science* **2011**, *332*, 1537.

[17] D. B. Schuepfer, F. Badaczewski, J. M. Guerra-Castro, D. M. Hofmann, C. Heiliger, B. Smarsly, P. J. Klar, *Carbon* **2020**, *161*, 359.

[18] K. A. Cychosz, R. Guillet-Nicolas, J. García-Martínez, M. Thommes, *Chem. Soc. Rev.* **2017**, *46*, 389.

[19] M. Thommes, K. Kaneko, A. V. Neimark, J. P. Olivier, F. Rodriguez-Reinoso, J. Rouquerol, K. S. W. Sing, *Pure Appl. Chem.* **2015**, *87*, 1051.

[20] G. Singh, J. Lee, A. Karakoti, R. Bahadur, J. Yi, D. Zhao, K. Albahily, A. Vinu, *Chem. Soc. Rev.* **2020**, *49*, 4360.

[21] A. C. Dassanayake, M. Jaroniec, *J. Mater. Chem. A* **2017**, *5*, 19456.

[22] J. Zhou, Z. Li, W. Xing, H. Shen, X. Bi, T. Zhu, Z. Qiu, S. Zhuo, *Adv. Funct. Mater.* **2016**, *26*, 7955.

[23] S. Khodabakhshi, M. Taddei, J. A. Rudd, M. J. McPherson, Y. Niu, R. E. Palmer, A. R. Barron, E. Andreoli, *Carbon* **2021**, *173*, 989.

[24] Z. Zhang, Z. P. Cano, D. Luo, H. Dou, A. Yu, Z. Chen, *J. Mater. Chem. A* **2019**, *7*, 20985.

[25] Y. Liu, J. Wilcox, *Environ. Sci. Technol.* **2012**, *46*, 1940.

[26] Y. Liu, J. Wilcox, *Int. J. Coal Geol.* **2012**, *104*, 83.

[27] X. Ma, L. Li, R. Chen, C. Wang, H. Li, S. Wang, *Appl. Surf. Sci.* **2018**, *435*, 494.

[28] B. Ashourirad, P. Arab, T. Islamoglu, K. A. Cychosz, M. Thommes, H. M. El-Kaderi, *J. Mater. Chem. A* **2016**, *4*, 14693.

[29] M. S. Shafeeyan, W. M. A. W. Daud, A. Houshmand, A. Shamiri, *J. Anal. Appl. Pyrolysis* **2010**, *89*, 143.

[30] A. Band, A. Albu-Yaron, T. Livneh, H. Cohen, Y. Feldman, L. Shimon, R. Popovitz-Biro, V. Lyahovitskaya, R. Tenne, *J. Phys. Chem. B* **2004**, *108*, 12360.

[31] C. Guéneau, J. L. Flèche, *Calphad* **2015**, *49*, 67.

[32] H. Okamoto, *J. Phase Equilibria Diffus.* **2010**, *31*, 86.

[33] W. Klemm, H. -J Scharf, *ZAAC - J. Inorg. Gen. Chem.* **1960**, *303*, 263.

[34] Y. Li, D. Q. Zhang, L. Duan, R. Zhang, L. D. Wang, Y. Qiu, *Appl. Phys. Lett.* **2007**, *90*, 012119.

[35] J. Zhao, Y. Cai, J. P. Yang, H. X. Wei, Y. H. Deng, Y. Q. Li, S. T. Lee, J. X. Tang, *Appl. Phys. Lett.* **2012**, *101*, 193303.

[36] Z. Liu, H. E. Wang, *Adv. Electron. Mater.* **2022**, *8*, 2101111.

[37] T. Li, Y. Rui, X. Wang, J. Shi, Y. Wang, J. Yang, Q. Zhang, *ACS Appl. Energy Mater.* **2021**, *4*, 7002.

[38] Z. Q. Xu, J. P. Yang, F. Z. Sun, S. T. Lee, Y. Q. Li, J. X. Tang, *Org. Electron.* **2012**, *13*, 697.

[39] H. G. Limberger, T. P. Martin, *Zeitschrift für Phys. D Atoms, Mol. Clust.* **1989**, *12*, 439.

[40] J. Huang, Z. Xu, Y. Yang, *Adv. Funct. Mater.* **2007**, *17*, 1966.

[41] T. R. B. A. H. Sommer, *J. Appl. Phys.* **1977**, *48*, 3547.

[42] Y. Liu, B. V. Merinov, W. A. Goddard, *Proc. Natl. Acad. Sci. U. S. A.* **2016**, *113*, 3735.

[43] G. Yoon, H. Kim, I. Park, K. Kang, *Adv. Energy Mater.* **2017**, *7*, 1601519.

[44] W. B. Li, S. Y. Lin, N. T. T. Tran, M. F. Lin, K. I. Lin, *RSC Adv.* **2020**, *10*, 23573.

[45] U. Mizutani, T. Kondow, T. B. Massalski, *Phys. Rev. B* **1978**, *17*, 3165.

[46] R. Matsumoto, N. Akuzawa, Y. Takahashi, *Mater. Trans.* **2006**, *47*, 1458.

[47] M. Inagaki, *Phys. Today* **1978**, *31*, 36.

[48] F. Pan, K. Ni, Y. Ma, H. Wu, X. Tang, J. Xiong, Y. Yang, C. Ye, H. Yuan, M. L. Lin, J. Dai, M. Zhu, P. H. Tan, Y. Zhu, K. S. Novoselov, *Nano Lett.* **2021**, *21*, 5648.

[49] F. Pan, K. Ni, T. Xu, H. Chen, Y. Wang, K. Gong, C. Liu, X. Li, M. L. Lin, S. Li, X. Wang, W. Yan, W. Yin, P. H. Tan, L. Sun, D. Yu, R. S. Ruoff, Y. Zhu, *Nature* **2023**, *614*, 95.

[50] E. Raymundo-Piñero, P. Azaïs, T. Cacciaguerra, D. Cazorla-Amorós, A. Linares-Solano, F. Béguin, *Carbon* **2005**, *43*, 786.

[51] R. Xue, Z. Shen, *Carbon* **2003**, *41*, 1862.

[52] L. Zhu, Y. Li, J. Zhang, X. Gan, Q. Li, T. Tang, Y. Chen, J. Zhu, N. Guo, L. Wang, S. Zhang, *Appl. Surf. Sci.* **2023**, *638*, 158051.

[53] H. J. Lee, D. Ko, J. S. Kim, Y. Park, I. Hwang, C. T. Yavuz, J. W. Choi, *ChemNanoMat* **2021**, *7*, 150.

[54] S. J. Yang, R. Rothe, S. Kirchhecker, D. Esposito, M. Antonietti, H. Gojzewski, N. Fechler, *Carbon* **2015**, *94*, 641.

[55] L. Wang, M. Peng, J. Chen, X. Tang, L. Li, T. Hu, K. Yuan, Y. Chen, *ACS Nano* **2022**, *16*, 2877.

[56] L. Wang, M. Peng, J. Chen, T. Hu, K. Yuan, Y. Chen, *Adv. Mater.* **2022**, *34*, 2203744.

[57] S. He, Z. Mo, C. Shuai, W. Liu, R. Yue, G. Liu, H. Pei, Y. Chen, N. Liu, R. Guo, *Appl. Surf. Sci.* **2022**, *577*, 151904.

[58] X. Shi, J. Xie, F. Yang, F. Wang, D. Zheng, X. Cao, Y. Yu, Q. Liu, X. Lu, *Angew. Chem. Int. Ed.* **2022**, *61*, e202214773.

[59] J. Yin, W. Zhang, W. Wang, N. A. Alhebshi, N. Salah, H. N. Alshareef, *Adv. Energy Mater.* **2020**, *10*, 2001705.

[60] H. Ma, H. Chen, M. Wu, F. Chi, F. Liu, J. Bai, H. Cheng, C. Li, L. Qu, *Angew. Chem. Int. Ed.* **2020**, *59*, 14541.

[61] S. Wu, Y. Chen, T. Jiao, J. Zhou, J. Cheng, B. Liu, S. Yang, K. Zhang, W. Zhang, *Adv. Energy Mater.* **2019**, *9*, 1902915.

[62] H. Wang, M. Wang, Y. Tang, *Energy Storage Mater.* **2018**, *13*, 1.

[63] P. A. Maughan, N. Tapia-Ruiz, N. Bimbo, *Electrochim. Acta* **2020**, *341*, 136061.

[64] X. Li, M. Li, Q. Yang, D. Wang, L. Ma, G. Liang, Z. Huang, B. Dong, Q. Huang, C. Zhi, *Adv. Energy Mater.* **2020**, *10*, 2001394.

[65] L. Dong, W. Yang, W. Yang, C. Wang, Y. Li, C. Xu, S. Wan, F. He, F. Kang, G. Wang, *Nano-Micro Lett.* **2019**, *11*, 94.

[66] Z. Xu, F. Xie, J. Wang, H. Au, M. Tebyetekerwa, Z. Guo, S. Yang, Y. S. Hu, M. M. Titirici, *Adv. Funct. Mater.* **2019**, *29*, 1903895.

[67] K. Wang, F. Sun, Y. Su, Y. Chen, J. Gao, H. Yang, G. Zhao, *J. Mater. Chem. A* **2021**, *9*, 23607.

[68] M. Liu, W. Cao, W. Song, J. Liu, X. Feng, Z. Li, Y. Cao, P. Wang, J. Niu, *J. Power Sources* **2022**, *541*, 231688.

[69] F. Wang, X. Wang, Z. Chang, X. Wu, X. Liu, L. Fu, Y. Zhu, Y. Wu, W. Huang, *Adv. Mater.* **2015**, *27*, 6962.

Chapter 4 Rational design of porous carbons for Zn-ion capacitor cathodes[3]

4.1 The role of pore size on the capacitive energy storage

Porous carbons are essential for capacitive energy storage due to their adjustable compositions, abundant porosities, and robust stability.[1–8] Pore size has been shown to significantly impact the electrochemical properties of supercapacitors,[9–13] as the non-planar electrochemical interfaces in nanopores (mainly micropores and mesopores) influence the degree of electrolyte confinement within the pores.[14] Small pore sizes allow ions to approach the carbon pore walls (possibly through partial desolvation), leading to more efficient screening of ionic charges and increased capacitance.[12] The maximum double-layer capacitance is obtained when the pore size matches the ion size, as ions cannot enter smaller pores while larger pore sizes increase the distance between the pore wall and ion center. However, small pore size may cause electrolyte depletion inside pores and sluggish ion dynamics due to steric hindrance of solvated ions and slow desolvation upon entering subnanometer pores.[13] Larger pores are crucial for accelerating ion transport within porous carbon networks. Typically, micropores are considered crucial for a high capacitance, while mesopores are connected with high rate capability. In macropores, electrolyte ion confinement can be ignored, allowing for the application of the classic electric double-layer model.

Aqueous Zn-ion capacitors have garnered increased attention recently due to their safety, low cost, high energy/power densities, and cycling stability. This is attributed to high theoretical capacity (820 $\mathrm{mAh \cdot g^{-1}}$) and low redox potential of −0.76 *vs.* standard hydrogen electrode of the Zn anode, rapid energy storage/release at the carbon cathode, and high ionic conductivity (up to 1 $\mathrm{S \cdot cm^{-1}}$) with the nonflammable and nontoxic aqueous electrolytes.[15–17] Recent studies have indicated that the carbon pore size influences electrochemical properties of Zn-ion capacitors,[18–21] but the understanding remains limited. In reported literature, the use of carbon materials that differ in pore structures, SSAs, and compositions makes it difficult to comprehend the real impact of porosity on the electrochemical properties.

In **Chapters 2** and **3**, we introduced a facile and controlled synthesis strategy for porous carbons, achieving both high yields (> 20%) and high SSAs (> 3000 $\mathrm{m^2 \cdot g^{-1}}$) through thermal treatment of

---

[3] Results of this chapter are adapted from the original work with permission of the authors: Jiaxin Li, Markus Antonietti, Patrice Simon, Mateusz Odziomek, Controlled Synthesis of Porous Carbons to Unravel the Role of Pore Size on Zn-Ion Capacitors, Manuscript in preparation, **2024**.

Cs salts of cheap carboxylic acids. Nonetheless, the resulting porous carbons are microporous, and lacking in mesopores. In **Chapter 4**, we present the use of uric acid (UA) to enhance the mesoporosity of CsAc-derived carbons. By adjusting the mass ratio of UA and CsAc, porous carbons are obtained with varying pore sizes while maintaining comparable compositions and SSAs. Using these micro-mesoporous carbons as model materials allows for a systematic investigation into the impact of pore size on the electrochemical performance of Zn-ion capacitors. This chapter aims to present an easily controlled material synthesis strategy, along with comprehensive insights into the impact of porosity on Zn-ion capacitors.

4.2 Synthesis and characterizations of porous carbons

UA was chosen as a modifier of the pore network, greatly enhancing the contribution of mesopores. The melting points of UA and CsAc are 300 and 194 ºC, respectively, with their decomposition temperatures falling within the range of 400 to 450 ºC, as indicated by TGA curves (***Figure 4.1***). Notably, the mixtures of UA and CsAc decompose at lower temperatures compared to the individual components alone, specifically at 320 and 170 ºC for mass ratios of 1:50 and 1:5. This phenomenon is possibly attributed to the weaker intermolecular interactions within the mixtures compared to those in the pure substances, which facilitates the melting and decomposition of mixtures. In subsequent experiments, UA and CsAc were mixed in mass ratios of 1:50 or 1:5, condensed at 800 ºC, followed by washings to remove residual Cs. The resultant samples are denoted as UC1:50 or UC1:5, with Cs content below 0.2 wt%. Commercial activated carbon YP-50F was included for reference purposes.

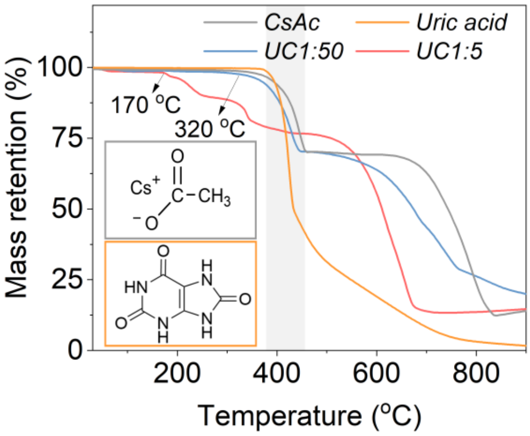

Figure 4.1. TGA curves of UA, CsAc, the 1:5 and 1:50 mass ratio mixtures of UA and CsAc.

The chemical structures of UC1:50 and UC1:5 were first characterized. Elemental combustion analysis (***Figure 4.2a***) indicates that UC1:50 and UC1:5 are chemically very similar, containing around 92 wt% of carbon, 3 wt% of oxygen, and 1 wt% of nitrogen. Their infrared spectra (***Figure 4.2b***) are typical for carbonaceous structures, with low-intensity broad absorption bands between 1200 and 1000 cm^{-1}, characteristic of highly conjugated oxygen and nitrogen functionalities. X-ray photoelectron survey spectra also confirmed their similar surface compositions (***Figure 4.2c***). Deconvolution of C 1s peak (***Figure 4.2d***) gives three main components centered at 284.6, 286.4, and 288.8 eV, corresponding to sp^2-C, C-O, and C=O bonds (that can come from both the material itself and adventitious carbon), respectively. Deconvolution of O 1s peak (***Figure 4.2e***) yields components centered at 531.8 and 533.3 eV, associated with C=O and C-O bonds. Importantly, the content and type of oxygen functionalities stay similar across all samples, including the reference YP-50F, minimizing the effect of the surface chemistry as a factor. XRD patterns of UC1:50 and UC1:5 (***Figure 4.2f***) exhibit a high-intensity slope at diffraction angles below 10° due to increased scattering on high surface area carbons.[22]

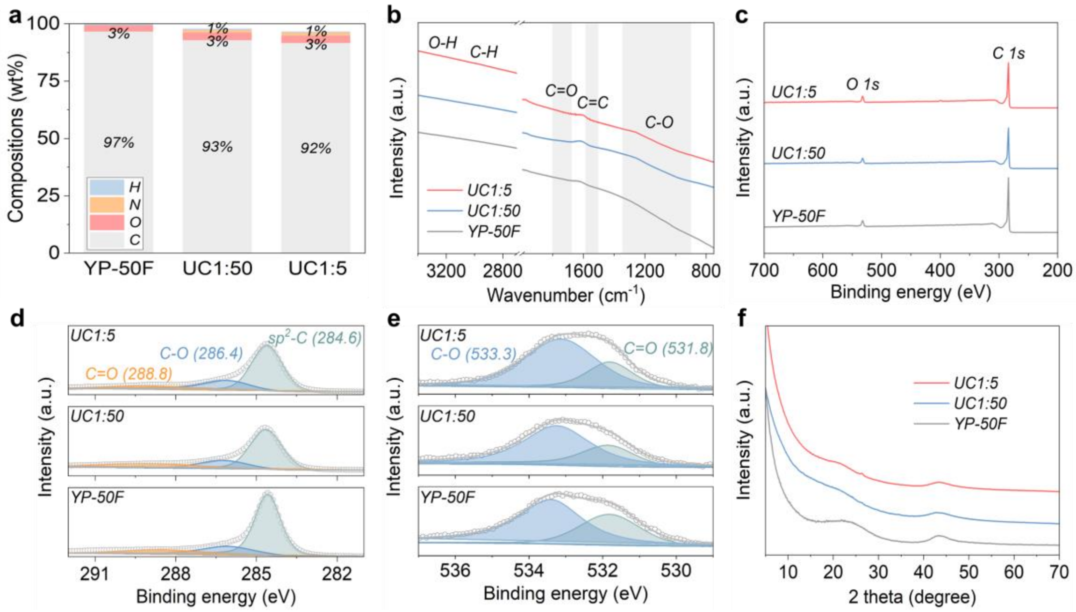

Figure 4.2. Chemical structures characterizations of UC1:5, UC1:50, and YP-50F. (a) Elemental compositions; (b) infrared spectra; (c) XPS survey spectra; high-resolution XPS (d) C 1s and (e) O 1s spectra; (f) XRD patterns.

Although UC1:50 and UC1:5 samples are chemically almost identical, they show different morphologies as revealed by SEM and TEM. UC1:50 exhibits colloidal-like structures that fuse, forming aerogel-like interconnected three-dimensional frameworks with visible voids ranging from 50 to 200 nm (***Figure 4.3a***). This morphology is typical in salt melt synthesis of porous carbon, where precursors dissolve, condense into carbonaceous matter, and precipitate from the ionic melt. TEM image of UC1:50 displays a uniform and continuous film. The HR-TEM image of UC1:50 shows a combination of disordered and locally ordered structures, featuring short but stacked lattices with interlayer spacing measured between 0.38 and 0.45 nm. In contrast, SEM images of UC1:5 exhibit a denser, void-free structure comprising smaller particles (***Figure 4.3b***). This suggests that a high mass ratio of UA accelerates carbon nucleation, particle aggregation, and phase separation from a continuous phase. TEM and HR-TEM images of UC1:5 have a strongly visible network of mesopores surrounded by curved, few-layer thick carbon structures.

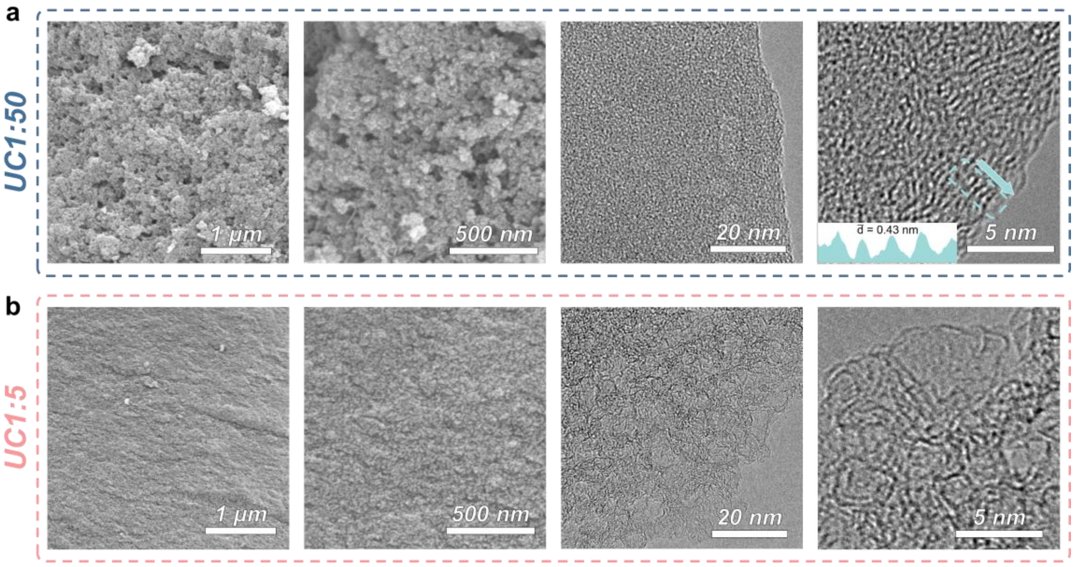

Figure 4.3. SEM, TEM, and HR-TEM images of (a) UC1:50 and (b) UC1:5.

Micropore analysis was conducted using Ar sorption at 87 K with high resolution at low pressures P/P_0 of 10^{-6} and validated by CO_2 sorption at 273 K, while mesopores were assessed through N_2 sorption at 77 K. The selection of Ar over N_2 for micropore analysis was based on its smaller kinetic diameter (Ar: 0.34 nm, N_2: 0.36 nm), faster diffusion rate at 87 K, and weaker interaction with surface functional groups.[23] The use of multiple techniques for pore structure measurement increases the confidence in the obtained results. Ar and N_2 sorption isotherms of UC1:50 (***Figure 4.4a, b***) exhibit a combination of Type I(b) and Type II isotherms. The steep uptake at low pressures ($P/P_0 < 0.1$) is characteristic of micropores, and the gradual increase in gas adsorption without a clear plateau near P/P_0 of 0.9 indicates the presence of macropores.[23,24] In comparison, UC1:5 displays a Type IV(a) isotherm with a continuous slope above P/P_0=0.2 and a Type H4 hysteresis loop in the P/P_0 range of 0.4−0.9, signifying the existence of significant amounts of mesopores with a broad pore size distribution.

QSDFT analyses of Ar or N_2 sorption isotherms show the presence of nanopores ranging from 0.7 to 4 nm in UC1:50, with notable maximum values at 0.9, 1.5, and 2.5 nm, while UC1:5 is rich in mesopores with pore widths from 3 to 12 nm (80% mesopores) (***Figure 4.4c, d***). These findings are consistent with TEM observations. Ar isotherms indicate that UC1:50 has a higher micropore volume of 1.12 $cm^3 \cdot g^{-1}$ than UC1:5 (0.68 $cm^3 \cdot g^{-1}$), whereas the mesopore volume is higher for UC1:5 (2.90 $cm^3 \cdot g^{-1}$) than UC1:50 (1.11 $cm^3 \cdot g^{-1}$) based on the results of N_2 isotherms. The pore size distributions above are in agreement with the results of CO_2 adsorption measurements at 273 K (***Figure 4.4e***). The highest CO_2 uptake of UC1:50 (8.3 $mmol \cdot g^{-1}$) at 100 kPa supports its highest micropore volume.[25] The BET SSA obtained from Ar isotherm of UC1:50 (3245 $m^2 \cdot g^{-1}$) is slightly lower than that of UC1:5 (3425 $m^2 \cdot g^{-1}$). For reference, YP-50F exhibits a Type I(b) isotherm typical for microporous materials, with 80% of pore sizes below 2 nm, a micropore volume (0.66 $cm^3 \cdot g^{-1}$), and a BET SSA (1783 $m^2 \cdot g^{-1}$), which are significantly lower than those of UC1:50 and UC1:5. The above chemical and textural information is summarized in ***Table 4.1***.

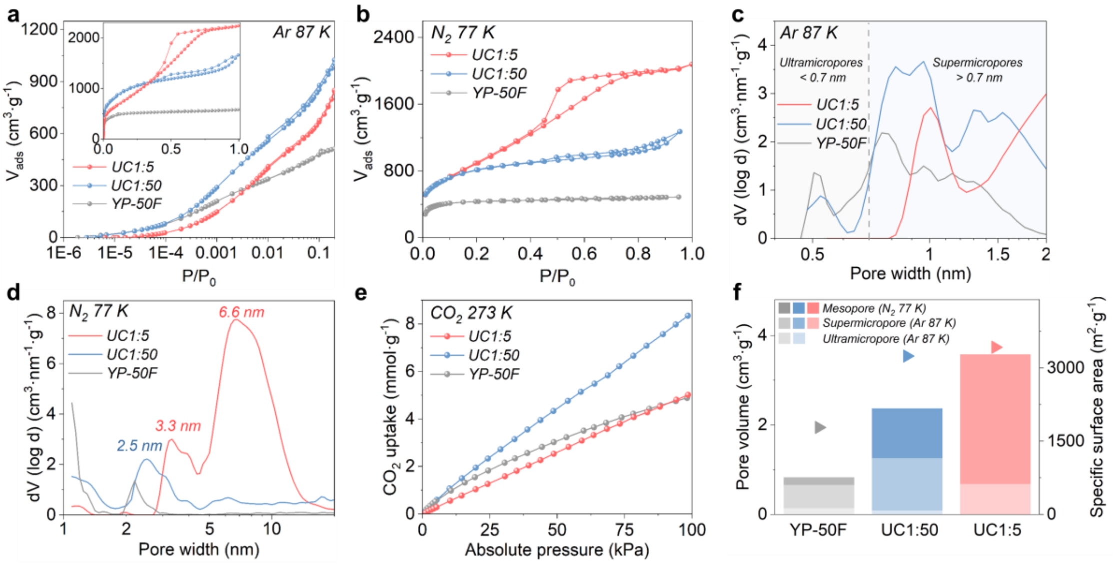

Figure 4.4. Gas sorption measurements of UC1:5, UC1:50, and YP-50F. (a) Enlarged figures of Ar sorption isotherms at 87 K with high resolution at low partial pressures (P/P_0 around 10^{-6}) (inset, Ar isotherms of P/P_0 from 10^{-6} to 1); (b) N_2 sorption isotherms at 77 K; (c, d) pore size distributions calculated from (c) Ar and (d) N_2 sorption isotherms; (e) CO_2 uptakes at 273 K; (f) comparison of ultramicropore, supermicropore, mesopore volumes, and BET SSAs.

Table 4.1. Compositions and porosities of condensed products obtained at different conditions.

Sample	C[a] (wt%)	O[a] (wt%)	H[a] (wt%)	N[a] (wt%)	Cs[b] (wt%)	$V_{0-0.7\ \mathrm{nm}}$[c] ($m^2 \cdot g^{-1}$)	$V_{0.7-2\ \mathrm{nm}}$[c] ($m^2 \cdot g^{-1}$)	S_{BET}[d] ($m^2 \cdot g^{-1}$)	$V_{2-50\ \mathrm{nm}}$[e] ($cm^3 \cdot g^{-1}$)	CO_2 uptake[f] ($mmol \cdot g^{-1}$)
UC1:5	91.6	3.2	0.5	1.4	0.2	0	0.68	3425	2.90	6.8
UC1:50	92.9	3.3	0.6	1.1	0.2	0.21	1.05	3245	1.11	8.3
YP-50F	96.6	2.8	0.6	0	0	0.25	0.41	1783	0.17	4.9

[a] Carbon, hydrogen, and nitrogen (C/H/N) and oxygen (O) content were determined through elemental combustion analysis in different modes. [b] Metal content was measured by ICP-OES. [c] Micropore volumes were calculated from Ar sorption isotherms at 87 K, using the QSDFT method for Ar adsorbed on carbon with slit pores. [d] SSAs were evaluated at P/P_0 (0.05−0.25) of Ar sorption isotherms at 87 K based on the BET equation. [e] Pore size distributions were calculated from N_2 sorption isotherms at 77 K using QSDFT for N_2 adsorbed on carbon with slit/cylindrical/sphere pore. [f] CO_2 uptake was obtained at 273 K and 100 kPa.

Overall, UC1:5 and UC1:50 present comparable elemental compositions and similar SSAs but differ significantly in the pore size distributions (***Figure 4.4f***). This distinction positions them as good candidates to investigate the impact of pore size in Zn-ion capacitors. In the aqueous electrolyte, ions, especially multivalent ones, are known to be highly hydrated due to their high charge density and high solvation free energy, leading to their larger hydrated ionic sizes than the corresponding bare ions.[26,27] The electrolyte (2 M $ZnSO_4$) contains Zn^{2+}, H^+, and SO_4^{2-} as possible charge carriers. Their hydrated ionic sizes are reported as 0.86 nm for $Zn(H_2O)_6^{2+}$, 0.28 nm for (H_3O^+), and 0.76 nm for SO_4^{2-} (3.1 H_2O), larger than their bare ions sizes of 0.15, 0.12, and 0.58 nm.[26–28] Specifically, Zn^{2+} concentration in the mild acidic electrolyte (pH=4.8) is typically several orders of magnitude higher than that of H^+.[29] For UC1:5, the majority of pores (3−12 nm) are much larger than the size of $Zn(H_2O)_6^{2+}$ (0.86 nm), favoring ionic diffusion. In comparison, UC1:50 contains a high ratio of nanopores of 0.7−4 nm (closely matching or exceeding the size of hydrated Zn^{2+}). YP-50F, being microporous with sizes from 0.5 to 2.5 nm, may necessitate (partial) desolvation of hydrated Zn ions for entry into ultramicropores.[14,30]

4.3 Electrochemical properties of Zn-ion capacitors

The influence of pore structure on ion storage and transfer was first investigated by Galvanostatic charge-discharge measurements of Zn-ion capacitors, comprising free-standing films of UC1:5, UC1:50, or YP-50F as cathode, Zn foil as anode, and glass fiber separator immersed in 2 M $ZnSO_4$ aqueous electrolyte in CR2032 coin cells. The mass loadings of active materials in the cathode were kept roughly the same at 1.6 $mg \cdot cm^{-2}$. UC1:50 demonstrates reversible specific capacities of 197, 164, 139, and 119 $mAh \cdot g^{-1}$ at 0.1, 0.2, 0.5, and 1.0 $A \cdot g^{-1}$, equivalent to capacitances of 443, 369, 313, and 268 $F \cdot g^{-1}$ (calculated based on a voltage window of 1.6 V), respectively (***Figure 4.5a***). At higher rates of 20, 50, and 100 $A \cdot g^{-1}$, discharge capacities of 71, 48, and 23 $mAh \cdot g^{-1}$ (160, 108, and 52 $F \cdot g^{-1}$) are retained. In comparison, UC1:5 delivers lower capacities of 145, 124, 109, 99 mAh·g^{-1} at 0.1, 0.2, 0.5, and 1.0 A·g^{-1} (***Figure 4.5b***), despite its slightly higher SSA than UC1:50. While UC1:5 exhibits a capacity decrease with increasing current density, it exceeds UC1:50 at around 50 A·g^{-1}. Both UC1:50 and UC1:5 outperform YP-50F, which collapses without any capacity output at 50 A·g^{-1} (***Figure 4.5c, d***). Finally, UC1:50 achieves a higher specific energy of 161.3 Wh·kg^{-1} and a lower specific power of 19.2 kW·kg^{-1}, compared with UC1:5 (117.2 Wh·kg^{-1} and 26.2 kW·kg^{-1}). YP-50F has the lowest specific energy and power (51.7 Wh·kg^{-1} and 6.2 kW·kg^{-1}) (***Figure 4.5e***).

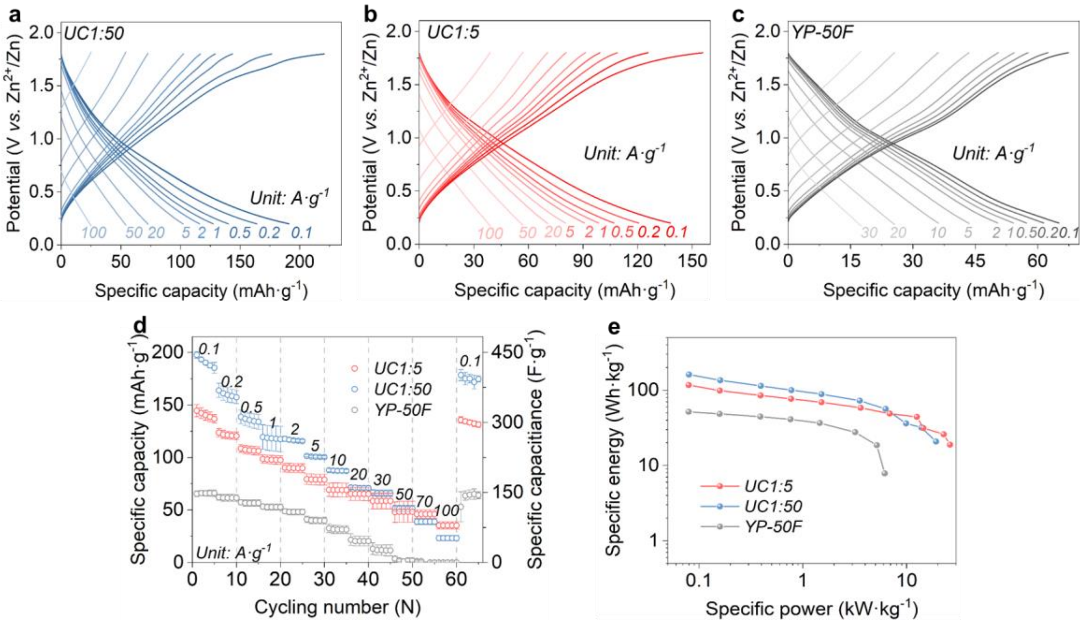

Figure 4.5. Electrochemical properties of Zn-ion capacitors based on UC1:5, UC1:50, and YP-50F. (a−c) Galvanostatic charge-discharge profiles at current densities from 0.1 to 100 A·g^{-1} (5th cycle); (d) rate capability at 0.1−100 A·g^{-1}. Both specific capacity (mAh·g^{-1}, left axis) and capacitance (F·g^{-1}, right axis) are provided for comparison with the literature. The error bars show the standard deviations for the results from four cells; (e) specific energy and power.

To reduce the influence of SSA differences among UC1:5, UC1:50, and YP-50F, the normalized capacities and capacitances by SSAs are provided as well (***Figure 4.6a***). Interestingly, below 10 A·g^{-1}, YP-50F shows comparable normalized capacities to UC1:5 and the discrepancy in normalized capacities between YP-50F and UC1:50 is less pronounced. As discussed earlier, UC1:50 comprises nanopores of 0.8−4 nm, UC1:5 features mesopores of 3−12 nm, and YP-50F has pores of 0.5−2.5 nm (***Table 4.1)***. Comprehensive analysis of structure and performance indicates that supermicropores and small mesopores (0.7−4 nm) contribute more to capacity in comparison with larger mesopores and ultramicropores at low current densities, as evidenced by the highest capacity of UC1:50. This is due to the main charge carrier, $Zn(H_2O)_6^{2+}$, reported to be 0.86 nm,[26] fitting well into pores of UC1:50, allowing for dense packing and efficient balancing of electrode charge by the adsorbed ionic species, as the ion centers get closer to the carbon surface for better charge storage (***Figure 4.6b***).[31] In comparison, hydrated Zn ions are more likely to pack loosely in the larger mesopores of UC1:5, with thicker hydration layers and larger effective ion sizes, leading to less efficient screening of electrode charge and lower capacitance. For YP-50F, hydrated Zn ions can enter supermicropores (and potentially ultramicropores requiring dehydration) at low current densities, explaining its higher normalized capacitances than UC1:5.

As the discharging/charging rate increases, the insufficient supply of charge carriers within pores limits charge screening at the electrolyte-electrode interfaces, highlighting the need for larger pores to enhance ion dynamics. Smaller pores may cause electrolyte depletion in pores due to sluggish ion transfer and desolvation issues, as evidenced by the significant capacitance fading of YP-50F at 30 $A \cdot g^{-1}$. While small mesopores (2−4 nm) ensure ion accessibility and surface utilization at low and moderate rates (0.1−30 $A \cdot g^{-1}$), larger mesopores of 4−12 nm become useful at practical currents, as supported by the higher capacity of UC1:5 above 50 $A \cdot g^{-1}$.

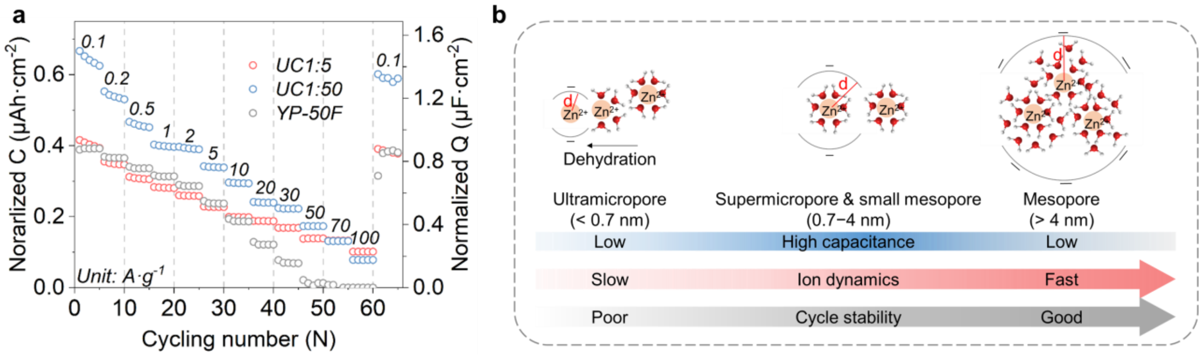

Figure 4.6. (a) Normalized capacity (C, left axis) and capacitance (Q, right axis) by SSA of each material; (b) d) illustration of $Zn(H_2O)_6^{2+}$ entering into pores with different sizes.

The cycling stability was assessed at 10 $A \cdot g^{-1}$ (***Figure 4.7***). UC1:50 and UC1:5 exhibit initial capacities of 81 and 56 $mAh \cdot g^{-1}$. After 0.29 million cycles, the capacity of UC1:50 decreases to 68 $mAh \cdot g^{-1}$ (84% capacity retention), followed by a sudden drop to 55 $mAh \cdot g^{-1}$ in subsequent cycles. UC1:5, however, shows 80% capacity retention over 0.6 million cycles (approximately 1 year). To the best of our knowledge, this marks a durability record for porous cathodes in Zn-ion capacitors, including porous carbons,[18,30,32–36] MXenes,[37–39] and metal oxides.[40,41] In stark contrast, YP-50F shows a capacity drop after 20,000 cycles and a collapse after 100,000 cycles.

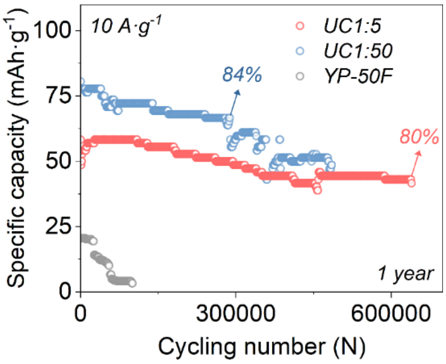

Figure 4.7. Cycling performance of UC1:5, UC1:50, and YP-50F at a current density of 10 A·g^{-1}.

The robust cycling stability of UC1:5 and UC1:50 over YP-50F is attributed to their larger pore sizes, which ensure rapid ionic diffusion. Particularly, larger mesopores of UC1:5 act as ion highways, balancing mass and electron transfer while buffering pore volume changes from ion sorption and the formation/dissolution of solid products like $Zn_4SO_4(OH)_6$ hydrates (ZHS) during discharging. XRD has confirmed the presence of ZHS (***Figure 4.8***), as a typical byproduct in Zn-ion systems with mildly acidic $ZnSO_4$ electrolytes, due to proton adsorption.[42–44] The pronounced capacity loss in YP-50F is likely attributed to micropore clogging by byproducts of electrolyte decomposition (*e.g.,* H_2 and ZHS) and/or structure collapse from continuous ion exchange and ZHS cycling.[45–47] This may reduce available surface area and hinder ionic diffusion. Besides, carbon oxidation, forming CO or CO_2, also blocks micropores.[48] The inevitable corrosion of Zn anode is also considered a possible reason for the capacity decay upon cycling.

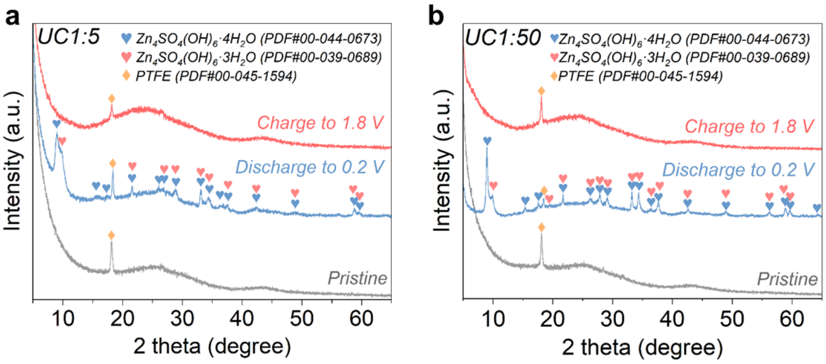

Figure 4.8. *Ex situ* XRD patterns of UC1:5 and UC1:50 discharging to 0.2 V and recharging to 1.8 V *vs.* Zn^{2+}/Zn.

4.4 Ion dynamics analysis

Then we further investigated ion dynamics within porous carbons based on a 3-electrode Swagelok cell including a carbon film as working electrode, Zn foil as counter electrode, and saturated calomel electrode (SCE) as reference electrode in 2 M $ZnSO_4$. The mass loadings of active materials were kept similar for all samples. The 3-electrode set-up ensures a stable reference potential and precise monitoring of potential evolution at the cathode.[49–51] The potential range at the carbon cathode, when operating in a Zn-ion capacitor at a voltage window of 0.2−1.8 V *vs.* Zn^{2+}/Zn, was measured between −0.8 and 0.75 V *vs.* SCE, applied for the following measurements.

Cyclic voltammetry (CV) tests were conducted with potential scan rates ranging from 5 to 200 $mV\cdot s^{-1}$. CV curves at 10 $mV\cdot s^{-1}$ of UC1:50 and UC1:5 (***Figure 4.9a, b***) exhibit similar capacitive quasi-rectangular shapes with a cathode peak at *ca.* −0.45 V (C1) and two anodic peaks at *ca.* −0.4 and *ca.* 0.2 V *vs.* SCE (A1, A2), indicating their comparable surface characteristics. YP-50F has a much smaller CV area and less visible A1 peak, attributed to its lower SSA and heteroatom content compared with UC1:50 and UC1:5 (***Figure 4.9c***). These CV results imply the contribution of electric double-layer capacitive and pseudo-capacitive processes to the charge storage. At a higher scan rate of 200 $mV\cdot s^{-1}$, CV curves are distorted, especially for YP-50F, indicating hindered ion transfer in the micropores. The ion adsorption dynamics were further assessed utilizing the relationship between peak current (*i)* and scan rate (*v)* through the equation $i = av^b$, where *a* and *b* are constants.[52] The *b* value of 0.5 signifies a diffusion-controlled redox process, while *b* value of 1 denotes a fast surface-controlled capacitive process. The *b*-values for cathodic/anodic peaks are close to 1 (***Figure 4.9d***), indicating a fast capacitive process than a slow diffusion process.

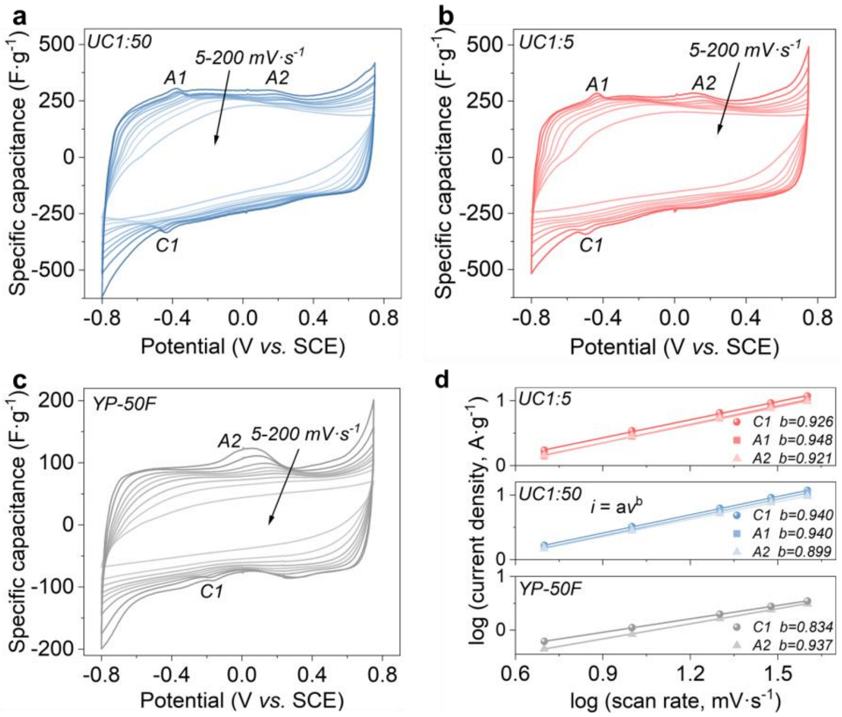

Figure 4.9. (a–c) CV curves at 5-200 mV·s^{-1} of (a) UC1:50, (b) UC1:5, and (c) YP-50F. (d) Plots of log(current density) *vs.* log(scan rate) of current response at peaks labeled in (a–c) and b values at scan rates of 5–40 mV·s^{-1}.

In situ electrochemical impedance spectroscopy (EIS) measurements were performed during discharging/charging (***Figure 4.10***). The Nyquist plots at various potentials exhibit high-frequency loops linked to charge transfer resistance (R_{ct}) at the electrode/electrolyte interfaces, followed by low-frequency slope lines describing ionic diffusion within porous carbon networks (Warburg impedance, Z_w).[49,54] During discharging, plots for UC1:50 remain constant from 0.75 to −0.4 V *vs.* SCE, and the loops enlarge and the lines exhibit a decreased slope from −0.4 to −0.8 V, indicating increased electronic and ionic transfer resistance (***Figure 4.10a***). [54,55] Reversible changes are observed during charging, with decreased R_{ct} and steeper slope lines from −0.8 to −0.4 V, while no significant change is noted above −0.4 V. This change in R_{ct} and Z_w between −0.8 and −0.4 V is associated with proton and ZHS activities. ZHS formation blocks pores, hindering charge transfer and ion diffusion, while its dissolution during charging frees up carbon pores and lowers these resistances. The relatively stable R_{ct} and Z_w values between −0.4 and 0.75 V relate to the adsorption/desorption of Zn^{2+} or SO_4^{2-}. Charge transfer resistance can possibly arises from specific bonding between ion and electrode surface, linked to ion solvation levels.[14]

Nyquist plots of UC1:5 show similar trends but lower resistances and less pronounced resistance changes than UC1:50 (***Figure 4.10b***), likely due to its larger mesopores can host more ZHS precipitation without serious micropore clogging. This evidences the effect of mesopores that reduce pore clogging and ensure ionic diffusion and charge transfer. YP-50F, in contrast, exhibits larger resistances between −0.8 and 0.4 V (***Figure 4.10c***), indicating micropore restricts access for hydrated ions, whereas lower resistances above 0.4 V are likely due to the inability of ions to desolvate and enter micropores at high potentials.

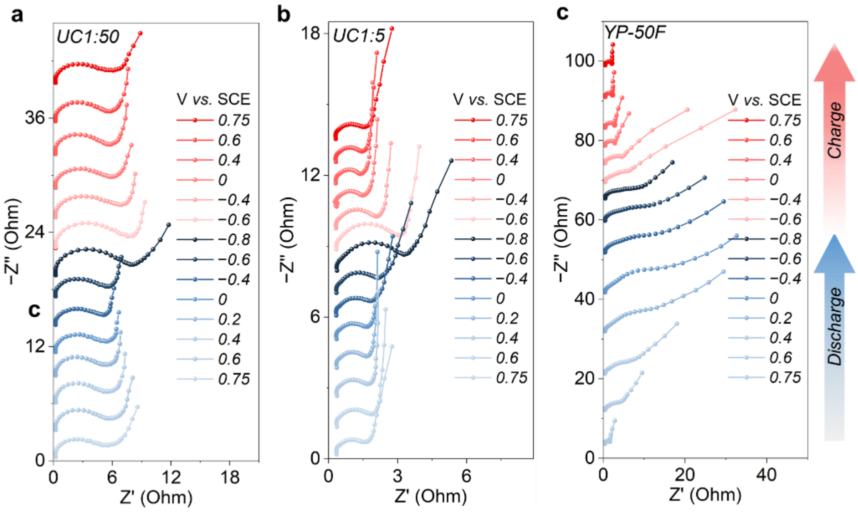

Figure 4.10. *In situ* EIS Nyquist plots of (a) UC1:50, (b) UC1:5, and (c) YP-50F recorded at different potentials.

The diffusivity of charge carriers (Zn^{2+}, H^+, or SO_4^{2-}) in the UC1:50, UC1:5, and YP-50F was further evaluated by the Galvanostatic intermittent titration technique (GITT, detailed in **Chapter 6**).[56,57] The ionic diffusion coefficients (D_{ion}) were determined by ***Equation 1***.

$$D_{ion} = \frac{4}{\pi t}\left(\frac{m_B V_m}{M_B S}\right)^2 \left(\frac{\Delta E_s}{\Delta E_t}\right)^2 \tag{1}$$

The formula incorporates t (current pulse duration in s), m_B (mass loading in mg·cm^{-2}), M_B (molar mass of carbon), V_m (molar volume of carbon), S (electrolyte-electrode contact area in cm^2), ΔE_s (the quasi-thermodynamic equilibrium potential difference before and after the current pulse in V), and E_t (potential difference during current pulse after eliminating the internal resistance drop in V). $L=(\frac{m_B V_m}{M_B S})$ is the ionic diffusion length (cm). The thickness of a compact electrode can be used as the ionic diffusion length.

UC1:50 and UC1:5 show constant ion diffusivity (D_{ion}) from 0.4 to −0.4 V vs. SCE and decreased D_{ion} below −0.4 V during discharging (***Figure 4.11***). This decline is associated with ZHS formation and hindered ionic diffusion in pores, while ion diffusivity recovers upon ZHS decomposition during charging. UC1:5 demonstrates higher D_{ion} (2×10^{-10}–1.5×10^{-7} cm^2·s^{-1}) than UC1:50 (1×10^{-10}–6×10^{-8} cm^2·s^{-1}), and significantly surpasses YP-50F (2×10^{-11}–4×10^{-8} cm^2·s^{-1}), indicating faster ion mobility in larger pores. Importantly, these D_{ion} values are competitive with reported cathode materials like carbons and MXenes for Zn-ion capacitors[58,59] and far exceed those in Zn-ion batteries (usually between 10^{-12} and 10^{-10} cm^2·s^{-1}).[28,60,61]

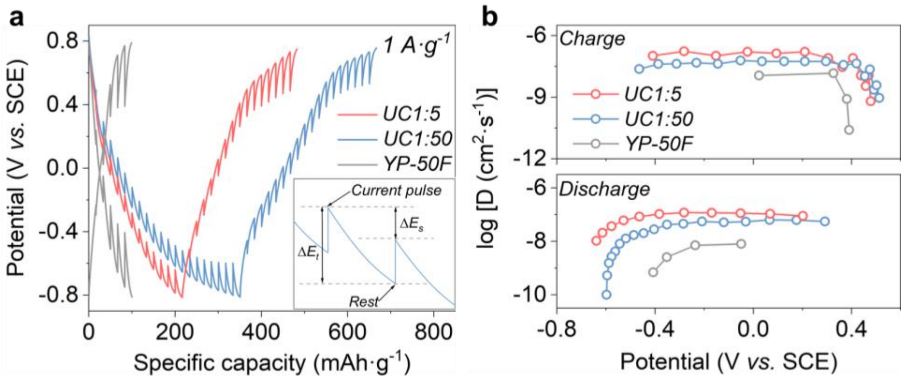

Figure 4.11. (a) Galvanostatic intermittent titration profiles of UC1:50, UC1:5, and YP-50F. Inset, the enlarged potential versus capacity profile of UC1:50; (b) calculated ionic diffusion coefficients D_{ion}.

4.5 Charge storage mechanism

To understand the comprehensive charge storage process of the Zn-ion capacitor, the electrochemical quartz crystal microbalance (EQCM) technique was used to analyze ionic and molecular fluxes on UC1:5, chosen for its good overall performance.[4] The principle of EQCM will be detailed in **Chapter 6**. Initial EQCM tests were performed in a 3-electrode EQCM cell including a bare Au-coated quartz resonator as working electrode, Zn as counter electrode, SCE as reference electrode, in 2 M $ZnSO_4$ electrolyte. The CV curve at 50 mV·s^{-1} shows multiple redox peaks accompanied by significant frequency change in the potential range of −0.8 and −0.2 V *vs.* SCE (***Figure 4.12a***), attributed to proton reduction/evolution and deposition/dissolution of ZHS on the Au surface. Meantime, no change in motional resistance change is observed (***Figure 4.12b***).

---

[4] The EQCM experiments were carried out in the lab of Prof. Patrice Simon at CIRIMAT, Université de Toulouse, CNRS, France.

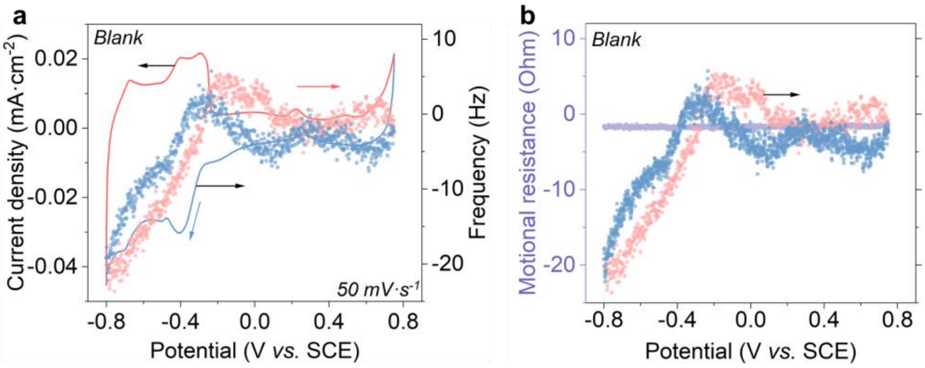

Figure 4.12. EQCM results of blank Au-coated quartz resonator in 2 M $ZnSO_4$ at a scan rate of 50 $mV \cdot s^{-1}$. (a) CV curve and corresponding frequency change; (b) frequency and motional resistance change.

Subsequently, UC1:5 was coated onto the Au-coated quartz resonator as a working electrode. The CV area of UC1:5 is much bigger than the blank, arising from the contribution of carbon to the current response (***Figure 4.13a***). During CV scans, the starting and ending points of the frequency and resistance loops always overlap, implying the electrode is under steady-state conditions. The motional resistance barely changes from 0.75 to −0.2 V, increases during reduction from −0.2 to −0.8 V, and decreases to the pristine value in the anodic scan (oxidation) (***Figure 4.13b***). This is in accordance with the observed frequency variations, albeit in the opposite direction. As discussed before, the resistance and frequency change at low potentials are correlated with ZHS precipitation/dissolution on the carbon. The validity of the gravimetric mode of EQCM measurements was confirmed by tracking $\Delta f/\Delta R$ during CV cycles, at an acceptable value of 7. This indicates a homogeneous and rigid coating of carbon on the surface of quartz crystal that does not detach from the crystal during measurements, allowing for the use of Sauerbrey's equation to convert the frequency change into mass change (***Equation 2***):[63]

$$\Delta m = -C_f \times \Delta f \tag{2}$$

where Δm ($ng \cdot cm^{-2}$) is the mass change of the coated quartz, C_f denotes the sensitivity factor of the crystal (6.98 $ng \cdot Hz^{-1}$), and Δf is the quartz resonance frequency (Hz). Hence, the electrode mass change (Δm) is negatively related to the change of quartz resonant frequency (Δf). Namely, a decrease in Δf indicates an increase in Δm and vice versa.

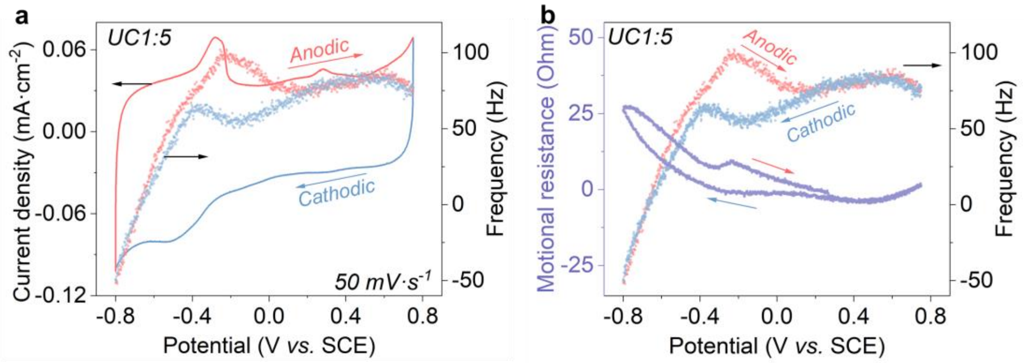

Figure 4.13. EQCM results of UC1:5 coted Au-quartz in a 2 M $ZnSO_4$ at a scan rate of 50 mV·s^{-1}. (a) CV and EQCM frequency response; (b) motional resistance and frequency change during polarization.

The potential of zero charge (PZC) of carbon signifies the potential at which the charge on the carbon surface is neutral, defining the border between regions where the negative/positive charge on the carbon surface is balanced with cations/anions for a potential more cathodic/anodic than PZC.[62] The PZC of UC1:5 is determined to be 0.3 V *vs.* SCE (***Figure 4.14***), reflecting its favorable interactions with SO_4^{2-} and identifying Zn^{2+} and H^+ as main charge carriers.

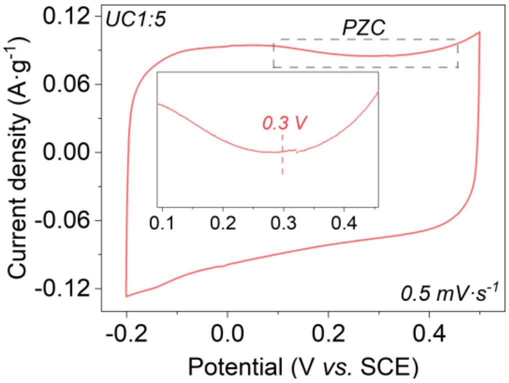

Figure 4.14. CV curves of UC1:5 at a low scan rate of 0.5 mV·s^{-1}. Inset, the enlarged profile.

Figure 4.15 shows the calculated change of electrode weight (Δm) *vs.* the charge passed in the electrode (ΔQ) during CV scans, where the arrow indicates scan directions. Faraday's law is applied to calculate the molecular weight from Δm−ΔQ plots (***Equation 3***),

$$\frac{\Delta m}{\Delta Q}=\frac{M_W}{nF} \tag{3}$$

where Δm represents the mass change of the electrode, ΔQ is the accumulated charges by integrating current with time (CV curves), n is the ion valence number, F is the Faraday constant (96,485 C·mol^{-1}), and M_w is the molecular weight. In this plot, the potential at 0.75/−0.8 V is taken as the origin of the charge ($\Delta Q=0$) for the cathodic/anodic scan. $\Delta m/\Delta Q$ is the slope of Δm-ΔQ plot, and n value of 1 is used here to calculate the normalized molecular weight per charge since Zn^{2+} or H^+ may participate in the charge storage.

During the cathodic scan, the charge storage mechanism at high potentials (0.75−0 V *vs.* SCE, Region I) can be explained by ion exchange (swapping of SO_4^{2-} for Zn^{2+}) and counter-ion adsorption (***Figure 4.15a***). Most likely, desorption of SO_4^{2-} leads to an initial mass decrease, followed by simultaneous SO_4^{2-} desorption and Zn^{2+} sorption, minimally affecting mass change, and hydrated Zn^{2+} adsorption then prompts a mass increase.[64] Between 0 and −0.4 V, the electrode mass turns to decrease at larger cathodic potentials, possibly due to dehydration of solvated Zn ions adsorbed on the carbon surface.[31] A recent study indicates that highly hydrated Zn^{2+} experience significant removal of the solvation shell, transitioning from Zn^{2+} (12.7 H_2O) to bare Zn^{2+} during cathodic polarization.[31] This process reduces effective ion size, enabling efficient screening of electrode charge by adsorbed ionic species and pronounced capacitance increase. At higher cathodic polarization (−0.4 to −0.8 V, Region III), the observed broad CV peak is primarily attributed to proton reduction, either by chemical adsorption on the carbon surface or interaction with oxygen functional groups like carbonyls. This results in a local pH increase and the precipitation of ZHS at the carbon, subsequently increasing both motional resistance and electrode mass. The average molar weight per charge at around −0.6 V *vs.* SCE is around 85 $g\cdot mol^{-1}$, roughly suggesting 1 proton reduction and 0.15 $Zn_4SO_4(OH)_6\cdot 4H_2O$ (M_w=532 $g\cdot mol^{-1}$) precipitation.

These processes progress reversibly during anodic scans (***Figure 4.15b***). During the oxidation sweep from −0.8 to −0.2 V *vs.* SCE (Region IV), the observed CV peak is accompanied by a drastic drop in mass and an increase in motional resistance, due to proton evolution and ZHS dissolution. The average mass change of 216 $g\cdot mol^{-1}$ can be interpreted into 1 proton evolution and 0.4 ZHS dissolution. The mass increase in region V is attributed to the solvation process of Zn^{2+} adsorbed at the carbon. No obvious mass change between 0 and 0.75 V corresponds to an ion exchange process (Zn^{2+} desorption and SO_4^{2-} adsorption). While EQCM has enhanced our understanding of the charge storage process, its limitation is measuring a single parameter (electrode mass), which depends on various factors such as cations, anions, solvents, and precipitation. This makes it difficult to identify and quantify the specific adsorbed ionic or molecules only from EQCM data, such as determining if Zn^{2+} is responsible for charge compensation at low potentials.

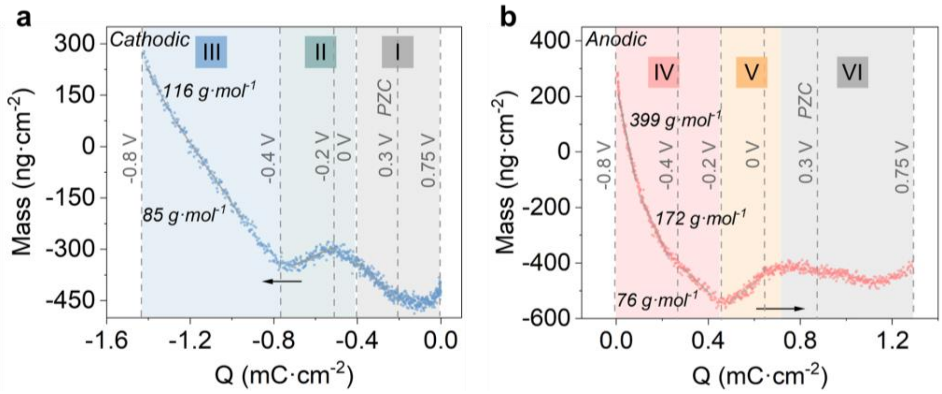

Figure 4.15. Electrode mass change (Δm) versus accumulated charge change (ΔQ) in the (a) cathodic and (b) anodic scans with three distinct regions shaded in different colors. The cut-off potentials of each scale are separated in vertical grey dashed lines.

Combining all the aforementioned findings, an overall charge storage mechanism is proposed as follows, where UC represents carbon. The hydrolysis by Zn^{2+} generates protons in the aqueous electrolyte, causing a mildly acidic electrolyte (pH=4.8). At high potentials, the adsorption/desorption of hydrated Zn^{2+}/SO_4^{2-} contributes to the electric double-layer capacitance. Dehydration of hydrated Zn^{2+} at middle potentials also leads to capacitance increase. At lower potentials, H^+ ions dominate as charge carriers, with their sorption affecting local pH near the carbon surface and leading to precipitation of ZHS. These processes reverse during charging.

$$Zn^{2+} + 2H_2O \rightleftharpoons Zn(OH)_2 + 2H^+$$

$$UC + Zn(H_2O)_n^{2+} \rightleftharpoons UC\|Zn(H_2O)_n^{2+}$$

$$UC\|SO_4^{2-} \rightleftharpoons UC + SO_4^{2-}$$

$$UC\|Zn(H_2O)_n^{2+} \rightleftharpoons UC\|Zn(H_2O)_x^{2+} + (n-x)H_2O$$

$$UC + H^+ + e^- \rightleftharpoons UC{\cdot}H$$

$$UC + H_2O + e^- \rightleftharpoons UC{\cdot}H + OH^-$$

$$4Zn^{2+} + 6OH^- + SO_4^{2-} + 4H_2O \rightleftharpoons Zn_4SO_4(OH)_6{\cdot}4H_2O\downarrow$$

In summary, to reveal the pivotal role of pore sizes on the Zn-ion capacitors, we developed a facile synthetic strategy to produce porous carbons with comparable surface chemistry but varying pore sizes, enriched in either supermicropores or mesopores, *via* simple adjustments of the ratio of molecule precursors. Using these carbons as model materials, we have identified pore size-dependent electrochemical behaviors. Supermicropores ensure a higher capacity (197 $mAh{\cdot}g^{-1}$), while mesopores contribute to higher rate performance and cycling stability with 80% capacity retention even after 0.6 million that outperform previously reported cathode materials. Further, comprehensive electrochemical analyses shed light on the charge storage mechanism. Our findings underscore the potential for tailored porous electrode design, aiming to optimize capacitive charge storage for high-performance metal-ion capacitors. Additionally, our study contributes fundamental insights into the charge storage mechanism of promising aqueous Zn-ion capacitors.

Reference

[1] K. Subramanyan, M. L. Divya, V. Aravindan, *J. Mater. Chem. A* **2021**, *9*, 9431.

[2] B. Li, J. Zheng, H. Zhang, L. Jin, D. Yang, H. Lv, C. Shen, A. Shellikeri, Y. Zheng, R. Gong, J. P. Zheng, C. Zhang, *Adv. Mater.* **2018**, *30*, 1705670.

[3] P. Cai, K. Zou, X. Deng, B. Wang, M. Zheng, L. Li, H. Hou, G. Zou, X. Ji, *Adv. Energy Mater.* **2021**, *11*, 2003804.

[4] D. Sui, M. Wu, K. Shi, C. Li, J. Lang, Y. Yang, X. Zhang, X. Yan, Y. Chen, *Carbon* **2021**, *185*, 126.

[5] B. L. J. Hardwick, *Johnson Matthey Technol. Rev.* **2018**, *62*, 134.

[6] L. F. Zhao, Z. Hu, W. H. Lai, Y. Tao, J. Peng, Z. C. Miao, Y. X. Wang, S. L. Chou, H. K. Liu, S. X. Dou, *Adv. Energy Mater.* **2021**, *11*, 2002704.

[7] J. Kim, M. S. Choi, K. H. Shin, M. Kota, Y. Kang, S. Lee, J. Y. Lee, H. S. Park, *Adv. Mater.* **2019**, *31*, 1803444.

[8] L. Wang, J. Pan, Y. Zhang, X. Cheng, L. Liu, H. Peng, *Adv. Mater.* **2018**, *30*, 1704378.

[9] J. Chmiola, G. Yushin, Y. Gogotsi, C. Portet, P. Simon, P. L. Taberna, *Science* **2006**, *313*, 1760.

[10] J. Chmiola, C. Largeot, P. L. Taberna, P. Simon, Y. Gogotsi, *Angew. Chem. Int. Ed.* **2008**, *47*, 3392.

[11] J. A. Fernández, S. Tennison, O. Kozynchenko, F. Rubiera, F. Stoeckli, T. A. Centeno, *Carbon* **2009**, *47*, 1598.

[12] C. Largeot, C. Portet, J. Chmiola, P. L. Taberna, Y. Gogotsi, P. Simon, *J. Am. Chem. Soc.* **2008**, *130*, 2730.

[13] K. Ge, H. Shao, P. L. Taberna, P. Simon, *ACS Energy Lett.* **2023**, *8*, 2738.

[14] S. Fleischmann, Y. Zhang, X. Wang, P. T. Cummings, J. Wu, P. Simon, Y. Gogotsi, V. Presser, V. Augustyn, *Nat. Energy* **2022**, *7*, 222.

[15] J. Yin, W. Zhang, N. A. Alhebshi, N. Salah, H. N. Alshareef, *Adv. Energy Mater.* **2021**, *11*, 2100201.

[16] L. Dong, W. Yang, W. Yang, Y. Li, W. Wu, G. Wang, *J. Mater. Chem. A* **2019**, *7*, 13810.

[17] D. Zhang, L. Li, Y. Gao, Y. Wu, J. Deng, *ChemElectroChem* **2021**, *8*, 1541.

[18] L. Wang, M. Peng, J. Chen, T. Hu, K. Yuan, Y. Chen, *Adv. Mater.* **2022**, *34*, 2203744.

[19] H. Ma, H. Chen, M. Wu, F. Chi, F. Liu, J. Bai, H. Cheng, C. Li, L. Qu, *Angew. Chem. Int. Ed.* **2020**, *59*, 14541.

[20] W. Jian, W. Zhang, X. Wei, B. Wu, W. Liang, Y. Wu, J. Yin, K. Lu, Y. Chen, H. N. Alshareef, X. Qiu, *Adv. Funct. Mater.* **2022**, *32*, 2209914.

[21] C. Zhao, Y. Lin, Q. Lin, Q. Liu, Y. Liu, Z. Liu, A. Ying, *Energy Storage Mater.* **2023**, *58*, 332.

[22] Y. Zhu, S. Murali, M. D. Stoller, K. J. Ganesh, W. Cai, P. J. Ferreira, A. Pirkle, R. M. Wallace, K. A. Cychosz, M. Thommes, D. Su, E. A. Stach, R. S. Ruoff, *Science* **2011**, *332*, 1537.

[23] K. A. Cychosz, R. Guillet-Nicolas, J. García-Martínez, M. Thommes, *Chem. Soc. Rev.* **2017**, *46*, 389.

[24] M. Thommes, K. Kaneko, A. V. Neimark, J. P. Olivier, F. Rodriguez-Reinoso, J. Rouquerol, K. S. W. Sing, *Pure Appl. Chem.* **2015**, *87*, 1051.

[25] P. I. Ravikovitch, A. Vishnyakov, R. Russo, A. V. Neimark, *Langmuir* **2000**, *16*, 2311.

[26] E. R. Nightingale, *J. Phys. Chem.* **1959**, *63*, 1381.

[27] Y. Marcus, *J. Chem. Soc., Faraday Trans.* **1993**, *89*, 713.

[28] Q. Guo, W. Li, X. Li, J. Zhang, D. Sabaghi, J. Zhang, B. Zhang, D. Li, J. Du, X. Chu, S. Chung, K. Cho, N. N. Nguyen, Z. Liao, Z. Zhang, X. Zhang, G. F. Schneider, T. Heine, M. Yu, X. Feng, *Nat. Commun.* **2024**, *15*, 2139.

[29] J. Huang, Z. Wang, M. Hou, X. Dong, Y. Liu, Y. Wang, Y. Xia, *Nat. Commun.* **2018**, *9*, 2906.

[30] H. Ma, H. Chen, M. Wu, F. Chi, F. Liu, J. Bai, H. Cheng, C. Li, L. Qu, *Angew. Chem. Int. Ed.* **2020**, *59*, 14541.

[31] K. Ge, H. Shao, E. Raymundo-piñero, *Nat. Commun.* **2024**, *15*, 1935.

[32] L. Wang, M. Peng, J. Chen, X. Tang, L. Li, T. Hu, K. Yuan, Y. Chen, *ACS Nano* **2022**, *16*, 2877.

[33] X. Shi, J. Xie, F. Yang, F. Wang, D. Zheng, X. Cao, Y. Yu, Q. Liu, X. Lu, *Angew. Chem. Int. Ed.* **2022**, *61*, e202214773.

[34] Y. Cao, X. Tang, M. Liu, Y. Zhang, T. Yang, Z. Yang, Y. Yu, Y. Li, J. Di, Q. Li, *Chem. Eng. J.* **2022**, *431*, 133241.

[35] W. Fan, J. Ding, J. Ding, Y. Zheng, W. Song, J. Lin, C. Xiao, C. Zhong, H. Wang, W. Hu, *Nano-Micro Lett.* **2021**, *13*, 59.

[36] J. Yin, W. Zhang, W. Wang, N. A. Alhebshi, N. Salah, H. N. Alshareef, *Adv. Energy Mater.* **2020**, *10*, 2001705.

[37] P. A. Maughan, N. Tapia-Ruiz, N. Bimbo, *Electrochim. Acta* **2020**, *341*, 136061.

[38] X. Li, M. Li, Q. Yang, D. Wang, L. Ma, G. Liang, Z. Huang, B. Dong, Q. Huang, C. Zhi, *Adv. Energy Mater.* **2020**, *10*, 2001394.

[39] J. Chen, H. Chen, M. Chen, W. Zhou, Q. Tian, C. P. Wong, *Chem. Eng. J.* **2022**, *428*, 131380.

[40] L. Dong, W. Yang, W. Yang, C. Wang, Y. Li, C. Xu, S. Wan, F. He, F. Kang, G. Wang, *Nano-Micro Lett.* **2019**, *11*, 94.

[41] S. He, Z. Mo, C. Shuai, W. Liu, R. Yue, G. Liu, H. Pei, Y. Chen, N. Liu, R. Guo, *Appl. Surf. Sci.* **2022**, *577*, 151904.

[42] L. Liu, Y. C. Wu, L. Huang, K. Liu, B. Duployer, P. Rozier, P. L. Taberna, P. Simon, *Adv. Energy Mater.* **2021**, *11*, 26.

[43] H. Liang, Z. Cao, F. Ming, W. Zhang, D. H. Anjum, Y. Cui, L. Cavallo, H. N. Alshareef, *Nano Lett.* **2019**, *19*, 3199.

[44] L. Wang, M. Peng, J. Chen, T. Hu, K. Yuan, Y. Chen, *Adv. Mater.* **2022**, *34*, 202203744.

[45] E. Marcerou, B. Daffos, P. L. Taberna, P. Simon, *Electrochim. Acta* **2023**, *472*, 143399.

[46] E. Pameté, L. Köps, F. A. Kreth, S. Pohlmann, A. Varzi, T. Brousse, A. Balducci, V. Presser, *Adv. Energy Mater.* **2023**, *13*, 2301008.

[47] M. He, K. Fic, E. Frackowiak, P. Novák, E. J. Berg, *Energy Environ. Sci.* **2016**, *9*, 623.

[48] P. Ratajczak, K. Jurewicz, P. Skowron, Q. Abbas, F. Béguin, *Electrochim. Acta* **2014**, *130*, 344.

[49] B. Zhang, L. Wang, Y. Zhang, X. Wang, Y. Qiao, S. G. Sun, *J. Chem. Phys.* **2023**, *158*, 054202.

[50] M. Gaberšček, *Nat. Commun.* **2021**, *12*, 19.

[51] S. Wang, J. Zhang, O. Gharbi, V. Vivier, M. Gao, M. E. Orazem, *Nat. Rev. Methods Prim.* **2021**, *1*, 41.

[52] T. Brezesinski, J. Wang, S. H. Tolbert, B. Dunn, *Nat. Mater.* **2010**, *9*, 146.

[53] X. Pu, D. Zhao, C. Fu, Z. Chen, S. Cao, C. Wang, Y. Cao, *Angew. Chem. Int. Ed.* **2021**, *60*, 21310.

[54] W. Choi, H. C. Shin, J. M. Kim, J. Y. Choi, W. S. Yoon, *J. Electrochem. Sci. Technol.* **2020**, *11*, 1.

[55] N. Ogihara, S. Kawauchi, C. Okuda, Y. Itou, Y. Takeuchi, Y. Ukyo, *J. Electrochem. Soc.* **2012**, *159*, A1034.

[56] Y. Zhu, C. Wang, *J. Phys. Chem. C* **2010**, *114*, 2830.

[57] Z. Song, H. Li, W. Liu, H. Zhang, J. Yan, Y. Tang, J. Huang, H. Zhang, X. Li, *Adv. Mater.* **2020**, *32*, 2001001.

[58] L. Ye, M. Liao, K. Zhang, M. Zheng, Y. Jiang, X. Cheng, C. Wang, Q. Xu, C. Tang, P. Li, Y. Wen, Y. Xu, X. Sun, P. Chen, H. Sun, Y. Gao, Y. Zhang, B. Wang, J. Lu, *Nature* **2024**, *626*, 313.

[59] K. Yang, L. Hu, Y. Wang, J. Xia, M. Sun, Y. Zhang, C. Gou, C. Jia, *J. Mater. Chem. A* **2022**, *10*, 12532.

[60] M. Liao, J. Wang, L. Ye, H. Sun, Y. Wen, C. Wang, X. Sun, B. Wang, H. Peng, *Angew. Chem.* **2020**, *132*, 2293.

[61] T. Wei, Q. Li, G. Yang, C. Wang, *Adv. Energy Mater.* **2019**, *9*, 1901480.

[62] E. Zhang, Y. C. Wu, H. Shao, V. Klimavicius, H. Zhang, P. L. Taberna, J. Grothe, G. Buntkowsky, F. Xu, P. Simon, S. Kaskel, *J. Am. Chem. Soc.* **2022**, *144*, 14217.

[63] Y. Ji, Z. W. Yin, Z. Yang, Y. P. Deng, H. Chen, C. Lin, L. Yang, K. Yang, M. Zhang, Q. Xiao, J. T. Li, Z. Chen, S. G. Sun, F. Pan, *Chem. Soc. Rev.* **2021**, *50*, 10743.

[64] A. C. Forse, C. Merlet, J. M. Griffin, C. P. Grey, *J. Am. Chem. Soc.* **2016**, *138*, 5731.

Chapter 5 Conclusion and outlook

5.1 Conclusion

The presented thesis aims to describe the synthesis, characterizations, and applications of porous carbon obtained from Cs salts of low-cost molecular precursors as the sole self-templating precursors. The synthesis mechanisms of porous carbons are systematically discussed, with an emphasis on the role of Cs in the construction of carbon frameworks and the formation of pore structures. The obtained porous carbons have demonstrated promising applications as electrodes of capacitive energy storage devices. The influences of composition and porosity on the capacitive energy storage are also analyzed.

Chapter 2 shows that the use of CsAc as a single precursor produces highly porous carbons, upon thermal treatment, with a yield of 10%, specific surface area of the order of 3000 $m^2 \cdot g^{-1}$, and pore volume approaching 2 $cm^3 \cdot g^{-1}$. In contrast, the use of KAc only achieves a 4% yield and a specific surface area of around 2000 $m^2 \cdot g^{-1}$, while no solid carbonaceous products are obtained with LiAc, NaAc, or $Zn(Ac)_2$ as the precursors. Detailed studies on the synthetic mechanism unravel that acetate groups activated by Cs transform into very active ketene species, which immediately condense to polyketones building the carbonaceous networks around *in situ* formed Cs carbonate. The *in situ* generated Cs species have multiple roles: (a) promoting the formation of carbonaceous networks, (b) acting as a structural directing agent and (c) porogen agent. As a demonstration, the final carbons show extremely high CO_2 uptake corresponding to 38 wt% of the material itself and a high specific capacitance of 374 $F \cdot g^{-1}$ (calculated based on a voltage window of 1 V) in the supercapacitor. Overall, this work is an example of how one can use the tools developed in organic chemistry to synthesize porous carbons. In other words, this work replaces traditional brute-force carbonization with organic solid-state chemistry, giving access to controlled synthesis of porous carbons with decent yield and defined structures.

Chapter 3 presents the use of Cs salts of carboxylic acids as precursors to produce highly porous carbons with a high yield of up to 25% and a specific surface area of 3008 $m^2 \cdot g^{-1}$, through direct thermal treatment. Importantly, the in-depth studies into reaction mechanism reveal unconventional roles of Cs in the condensation and activation of carbon frameworks. The *in situ* formation of Cs compounds (such as Cs carbonates, oxides, or metal) with low work functions, fosters electron transfer to the carbonaceous networks, most likely forming the charged graphitic-like structures accommodating positively charged Cs ions, analogous to well-known Cs graphite intercalation compounds (*e.g.,* CsC_8). This intercalation process with Cs significantly contributes to the formation of slit pores without decreasing the carbon yields, in a stark contrast to etching process in the case of Na and K compounds. The lower activation temperature (at least 200 ºC lower than for K) preserves heteroatom functionalities in the resulting porous carbons, favoring for capacitive energy storage. Finally, the obtained porous carbons exhibit an impressive capacity of 252 $mAh \cdot g^{-1}$ (equivalent to 567 $F \cdot g^{-1}$, calculated based on a voltage window of 1.6 V) and cycling stability surpassing 100,000 cycles in aqueous Zn-ion capacitors, outperforming other capacitive materials that require complex synthetic processes. Overall, these findings further underscore the potential of applying the principles from organic chemistry, specifically the "Cs effect", to the synthesis of carbon materials, moving away from traditional carbonization methods towards organic solid-state chemistry. The simple preparation protocol yields high-performance materials for electrochemical energy storage.

Chapter 4 shows the use of uric acid as a mesopore enhancer for microporous carbons derived from CsAc to produce a series of porous carbons with similar compositions and specific surface areas but adjustable pore structures. These obtained porous carbons have demonstrated excellent performance in aqueous Zn-ion capacitors, with a high capacity of 197 $mAh \cdot g^{-1}$ (equivalent to 567 $F \cdot g^{-1}$ based on a voltage window of 1.6 V) high capacity retention at 100 $A \cdot g^{-1}$, and superior cycling stability of over 0.6 million cycles. Systematic electrochemical measurements indicate that supermicropores contribute to high capacity, while mesopores enhance rate capacity and cycling stability. The charge storage mechanism involves a combination of processes including proton adsorption/desorption coupled with the precipitation/dissolution of zinc hydroxysulfate hydrate and the electric double-layer capacitance within the carbon nanopores. Overall, this work provides a facile and controlled material synthetic strategy for porous carbonaceous materials, serving as model materials for the investigation of the impact of pore sizes in the capacitive energy storage.

In conclusion, this thesis provides a facile synthetic strategy for porous carbons with high specific surface areas (1000–3000 $m^2 \cdot g^{-1}$), tunable micro-/meso-pore structures, and adjustable elemental compositions. The method is versatile, with the potential for adaptation and modification to synthesize functional carbons for diverse applications. The synthetic mechanism is investigated using up-to-date characterization techniques, which highlights the potential of ignored Cs in condensation and activation of porous carbonaceous materials. The study of these materials demonstrates their broad applicability in capacitive energy storage and beyond. These results correspond to our initial motivation and will contribute to the conscious use of metal salts to mediate the structures and properties of carbonaceous materials toward a sustainable society.

5.2 Outlook

5.2.1 Synthetic mechanism analysis by advanced characterizations

In **Chapters 2** and **3**, we proposed that the decomposition of Cs salts forms Cs oxides and metal, which may inject electrons into organic/carbonaceous frameworks and intercalate into graphitic layers to promote the formation of carbon frameworks and the development of porous structures. However, due to the high instability of Cs oxides and metal in the air and the amorphous state at high temperatures, we have failed to provide direct experimental evidence to support this hypothesis. So far, we are still exploring methods like *in situ* synchrotron X-ray techniques or *in situ* transmission electron microscopy. However, much effort is still needed to produce reliable experimental results due to the complexity of the pyrolysis process and the challenging reaction conditions involving high temperature and inert gas protection. More advanced characterizations will help understand the synthesis process.

5.2.2 Extensive applications of porous oxo-carbons

This thesis mainly focuses on the characterizations and applications of highly porous carbons synthesized at 600−800 °C in the context of capacitive energy storage due to their large specific surface areas and rich microporous structures. However, it is crucial to realize that, for specific applications like anode materials in Li/Na-ion batteries or cathode materials of metal-air batteries, microporous structures are not necessary and may even impede performance. The porous carbons obtained at lower temperatures like 400 °C exhibit lower surface areas and retain higher oxygen content, which may perform better as battery electrodes. Such low synthetic temperature is also favorable for low energy consumption. Moreover, high oxygen content holds the potential to stabilize metal atoms, being promising catalytic cathodes in metal-air batteries and electrodes in electrochemical catalytic conversion.

5.2.3 Increase carbon yield and recycle metal

As is commonly known, the cost of raw materials and the yield of final products influence the overall cost of final products, thereby influencing their industrial viability. This thesis focuses on the utilization of molecular precursors, enhancing carbon yields to 25% while keeping high SSAs of around 3000 $m^2 \cdot g^{-1}$. There is still a possibility to further increase the carbon yield through the rational design or more appropriate selection of molecular precursors. Besides, the synthesis can be easily extended to encompass a diverse range of heteroatom-rich carbons by using precursors containing other heteroatoms (*e.g.,* nitrogen, phosphorus, sulfur, and boron). Finally, it is necessary to recover Cs species and convert them back into Cs salts, to further reduce the production cost and make the whole process more sustainable and economical. Further investigation should seek methods to recycle Cs salts, particularly in the context of large-scale production of porous carbons.

5.2.4 Explore more possibilities on the porous carbon synthesis

This thesis has presented a research framework on carbon materials, applying tools from organic chemistry to carbon science, with Cs element as an example. It is worth noting that numerous metals or non-metallic elements remain unexplored in the synthesis of carbon materials, although they have implemented significant influences in other fields like organic or polymer chemistry. This inspires us to keep an open mind, cooperate extensively, and borrow research strategies from other fields to solve problems in the field of carbon materials.

Chapter 6 Appendix

6.1 List of abbreviations

Table 6.1 List of abbreviations of characterization techniques and special terms.

Abbreviation	Full name
TGA-MS	thermogravimetric analysis-coupled with mass spectrometry
ECA	elemental combustion analysis
ICP-OES	inductively coupled plasma-optical emission spectrometry
FTIR	Fourier-transform infrared spectroscopy
PXRD	powder X-ray diffraction
XPS	X-ray photoelectron spectroscopy
MALDI-TOF	matrix-assisted laser desorption/ionization time-of-flight
SEM	scanning electron microscopy
EDX	energy dispersive X-ray spectroscopy
HR-TEM	high-resolution-transmission electron microscopy
BET	Burner–Emmett–Teller method
SSA	specific surface area
PSD	pore size distribution
QSDFT	quenched-solid density functional theory
NLDFT	non-local density functional theory
IUPAC	international Union of Pure and Applied Chemistry
Q_{st}	specific heat of adsorption
V_{meso}	mesopore volume
V_{micro}	micropore volume
V_{total}	total pore volume
CV	cycle voltammetry
GCD	Galvanostatic charge/discharge
EIS	electrochemical impedance spectra
GITT	Galvanostatic intermittent titration technique
RHE	reversible hydrogen electrode
SCE	saturated calomel electrode
µm	micrometer
nm	nanometer
at%	atomic percentage
wt%	weight percentage

6.2 Applied methods

Thermogravimetrical analysis (coupled with mass spectroscopy) (TGA-MS)

TGA is a type of analytical technique to study the thermal stability and transition of material at increasing temperature. During TGA, a sample is subjected to controlled temperature increases, and the resulting mass loss or gain is recorded in either an inert or synthetic air atmosphere as a function of temperature. TGA was performed from 30 to 1000 °C in a NETZSCH TG 209 F1 Libra device at a heating rate of 10 $K \cdot min^{-1}$ in a Pt crucible either with N_2 or synthetic air atmosphere.

When TGA is coupled with a mass spectrometer, the released gas decomposition products can also be identified. TGA-MS measurements were performed using a thermo microbalance TG 209 F1 Libra (Netzsch, Selb, Germany) coupled with a Thermostar MS (Pfeiffer Vacuum; Asslar/Germany) with an ionization energy of 75 eV. Samples were heated at 2.5 $K \cdot min^{-1}$ from 30 to 900 °C in a helium flow of 10 $mL \cdot min^{-1}$. Data were recorded and analyzed by the Proteus (6.0.0 to 8.0.0) and Quadstar (7.03, MID modus) software package. Antje Voelkel performed the measurements.

Elemental combustion analysis (ECA)

ECA is an analysis method used to determine the elemental composition of a sample, particularly for organic compounds. For analysis of C/H/O/N, the sample is burned in the excess of oxygen atmosphere up to 1000 °C, leading to the conversion of all carbon to CO_2, hydrogen to H_2O, nitrogen to NOx, and S to SO_2. The produced gases are then separated by a gas chromatography column and quantified using a thermal conductivity detector. To measure oxygen, the sample is pyrolyzed in a furnace and then passed through a chemical trap that absorbs all impurities into the gas chromatography column and finally into the thermal conductivity detector for detection. EA measurements in this thesis were performed using a vario MICRO cube CHNOS Elemental Analyzer in the CHNS mode or O mode. Antje Voelkel performed the measurements.

Inductively coupled plasma-optical emission spectroscopy (ICP-OES)

ICP-OES is used for the quantitative analysis of the content of metal in the sample. In ICP-OES, a high-temperature inductively coupled plasma is used to ionize the atoms in the sample, and the resulting ions emit characteristic light when they return to their ground state. The emitted light is then dispersed and detected by an optical spectrometer. The emission intensity is characteristic for each element analyzed and can be directly correlated to its concentration *via* a calibration curve, allowing for the identification and quantification of elements present in the sample ICP-OES measurements in this thesis were conducted using an ICP-OES Optima 8000 Perkin Elmar. Multi-Element-Standards have been used for calibration. Before the measurements, 10 mg of product is put in a 50 mL tube with 167 µL HNO_3 (63 vol%) and 333 µL HCl (36.5 vol%) overnight to dissolve the metal ions. Jessica Brandt performed the measurements.

Fourier transform-infrared spectroscopy (FT-IR)

Infrared spectroscopy measurements are based on the absorption of specific wavelengths by molecules when irradiated with electromagnetic radiation, corresponding to the energy needed for a transition. Here the electromagnetic radiation is in the mid-infrared range from 4000 to 400 cm^{-1}. Vibrational and vibrational-rotational transitions can be detected if the requirements of a change in dipole are fulfilled. This technique enables structural clarification and semi-quantitative evaluation. The spectra are typically shown as the transmission of radiation versus the wavenumber. A signal is observed when the sample absorbs light during a molecular transition. In an FTIR setup, a beam containing multiple frequencies is directed into a Michaelson interferogram, and the data is obtained by processing through applying Fourier transformation. The measurements in this thesis have been performed on a Thermo Scientific Nicolet iD5 spectrometer.

Powder X-ray diffraction (PXRD)

PXRD measurements are based on the interaction between an X-ray beam and electrons of atoms in the sample. It is a widely used characterization method for crystalline materials. X-ray is generated in an X-ray tube upon bombardment of copper with high-energy electrons, resulting in the radiation of a continuous X-ray spectrum. The generated monochromatic X-rays are then directed towards the sample. At the sample elastic and inelastic interactions occur. Inelastic interactions cause coherent scattering, forming the basis for all diffraction experiments. If the wavelength (λ) of the radiation is in the range of the distance of the diffraction lattice, diffraction occurs. Positive interference exists only at specific diffraction angles (θ). Bragg's Law provides the mathematical description of the interlayer spacing (d_{hkl}) of the atomic planes and the wavelength (λ) concerning θ (***Equation 1***).

$$n\lambda = 2d_{hkl}\sin\theta \tag{1}$$

Positive interferences (positive n) lead to reflections in the diffractogram, giving characteristic diffraction patterns of the material. *Ex situ* XRD patterns were recorded on a Smartlab Studio II powder X-ray diffractometer (with Cu Kα radiation in the 2θ range from 5° to 70°). *In situ* XRD patterns were collected using a Bruker D8 powder X-ray diffractometer with a high-temperature chamber (Anton Paar HTK 1200N) under a constant flow of N_2 (flow rate: 0.5 sccm).

Raman spectroscopy

Raman spectroscopy is a technique used to study vibrational, rotational, and other low-frequency modes in a system. The mechanism of Raman scattering involves the inelastic scattering of light by molecules. A monochromatic light source, often a laser, is directed onto a sample. The incident photons interact with the molecules in the sample. Most of the incident photons undergo elastic scattering, Rayleigh scattering, where the scattered photons have the same energy as the incident photons. However, a small fraction of the incident photons undergo inelastic scattering, known as Raman scattering. In this process, the scattered photons have different energies than the incident photons due to the exchange of energy with molecular vibrations, rotations, or electronic transitions. The energy difference between the incident and scattered photons corresponds to the energy of a molecular vibration or rotation. The resulting Raman spectrum provides information about the vibrational and rotational modes of the molecules in the sample. The difference in energy between the incident and scattered photons is called the Raman shift. It is expressed in wavenumbers (cm^{-1}) and corresponds to the vibrational frequencies of the molecular bonds. Raman spectra were recorded on the Alpha300R with a 532 nm laser excitation wavelength in this thesis.

X-ray photoelectron spectroscopy (XPS)

XPS is a non-destructive surface analysis (sample depth of *ca.* 3−10 nm) technique. The analysis occurs in an ultra-high vacuum and provides valuable information about the surface composition and chemical state of the elements. In a typical experiment, the sample is irradiated with X-ray photons (of energy h*υ*), and an electron from the core level is ejected with the kinetic energy (K.E.). This phenomenon is called the photoelectric effect. The Einstein equation (***Equation 2***) gives the correlation to the binding energy (B.E.) of the ejected electron.

$$K.E. = h\nu - B.E. - \phi \tag{2}$$

With Φ as the work function and B.E. as the binding energy of the ejected electron, which is characteristic of each element. Additional information about the specific chemical binding motifs can be obtained due to the dependency of the fine structure of the element on its surroundings.

XPS measurements in this thesis were performed on a ThermoScientific Escalab 250 Xi. A micro-focused, monochromated Al Kα X-ray source (1486.68 eV) and a 400 µm spot size were used in the analysis. Samples were prepared using carbon tape. LiCl was added to each sample to calibrate the binding energies towards Li. ThermoScientific Avantage software was used to analyze the resulting spectra. Measurements were performed in TU Berlin.

Gas/vapor physisorption measurements

The term “adsorption” refers to the enrichment of one or more components at the interface between a solid (the adsorbent) and a fluid. The fluid in its free state is termed adsorptive, while in the adsorbed state, it is referred to as the adsorbate. In general, it is distinguished between chemisorption and physisorption. In chemisorption, the formation of covalent bonds occurs and thus a higher enthalpy is involved. Physisorption involves attractive dispersion forces, short-range repulsive forces, and specific molecular interactions. Physisorption is widely used as an analytical tool for the characterization of porous solids and powders.

Nitrogen and argon physisorption

Nitrogen is a commonly chosen adsorbate for physisorption measurements due to its low cost, inert nature, and ability to form multilayer adsorption on the material's surface. Nitrogen adsorption refers to the process of adsorbing nitrogen gas onto the surface of a solid material, typically conducted at 77 K and atmospheric pressure, ensuring weak van der Waals interactions and facilitating multilayer formation. This allows the qualitative and quantitative determination of the surface area, pore volume, and pore size. In a typical measurement, the adsorbate is dosed into a sample cell and the gas uptake is recorded in dependence of the relative pressure. The relative pressure is increased up to $P/P_0=1$ to obtain the adsorption isotherm and then the pressure is lowered to get the desorption isotherm. The obtained isotherms are classified according to IUPAC recommendations, and the types give information about the pore width of material with micropore (pore width < 2 nm), mesopore (pore width of 2−50 nm), and macropore (pore width > 50 nm).

Figure 6.1 shows the different isotherms. Reversible **Type I isotherm** is concave to the P/P_0 axis and the amount adsorbed approaches a limiting value (governed by the accessible micropore volume). The steep uptake at low relative pressures is a result of enhanced solid-gas interactions in the narrow micropores (micropore filling). A Type I isotherm is typical for microporous materials with subdivision into Type I(a) for the filling of narrow micropores (pore width < 1 nm) and Type I(b) for micropores and possibly narrow mesopores (1−2.5 nm). Reversible **Type II** isotherm can be seen for non-porous or macroporous materials. It shows unrestricted monolayer-multilayer adsorption up to high relative pressures. Point B signifies the point when the monolayer is completed. If this point is more gradual, a simultaneous monolayer and multilayer formation takes place. **Type III** isotherms occur when adsorbent-adsorbate interaction is weak. The adsorption is based on clustering of the adsorbate around favorable sites on the surface. Mesoporous materials show **Type IV** isotherms. If a hysteresis is present, it is a **Type IV(a)** isotherm, as a consequence of capillary condensation in pores wider than 4 nm. The vapor-liquid phase transition is delayed due to nucleation, which does not occur in the desorption. If the mesopores are smaller than 4 nm, this effect does not occur and a reversible **Type IV(b)** isotherm is obtained. A **Type V** isotherm indicates a not entirely covered surface. Small amounts are adsorbed at low relative pressures and more filling is happening at higher relative pressures by nucleation growth. This is observed for water adsorption on hydrophobic microporous and mesoporous adsorbents. The reversible stepwise **Type VI** isotherm is representative of layer-by-layer adsorption on a highly uniform nonporous surface.

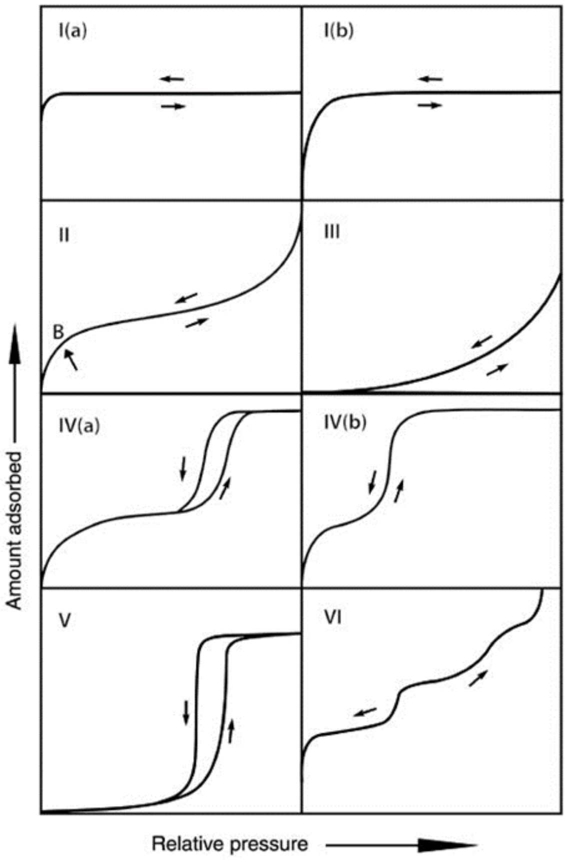

Figure 6.1. Classification of physisorption isotherms according to IUPAC recommendations.

Evaluation of the surface area of porous materials is commonly performed by the Brunauer-Emmett-Teller (BET) model by transforming the physisorption isotherm into a “BET-plot” and applying the BET-equation (***Equation 3***).

$$\frac{\frac{p}{p_0}}{V_{ads}(1-\frac{p}{p_0})} = \frac{1}{V_{mono}C} + \frac{C-1}{V_{mono}C}(p/p_0) \tag{3}$$

With V_{ads} being the total adsorbed volume, V_{mono} the monolayer volume, and C the adsorption constant. V_{mono} is obtained by a linear relation. The range is usually restricted to a part of the isotherm within P/P_0 of 0.05−0.25 where monolayer formation is assumed. In the case of microporous materials, this range may vary due to a different mechanism *i.e.,* micropore filling and monolayer adsorption overlap. In this case, the criteria for the proper selection of the range to consider are as follows: (a) the adsorbed amount of gas has to increase with increasing relative pressure, and (b) a positive intercept of the linear region.

The specific BET surface area (S_{BET}) is then calculated following ***Equation 4***.

$$SSA_{BET} = \frac{V_{mono}\sigma_{N2}N_A}{m} \tag{4}$$

With σ_{N2} being the cross-section of a nitrogen molecule (0.162 nm^2), N_A the Avogadro constant, and m as the mass of the adsorbent.

The isotherms serve also information about the pore size distribution. Mesopore size analysis with the Barrett-Joyner-Halenda (BJH) method is one of the basic methods. It is based on the Kelvin equation (***Equation 5***), which correlates the relative pressure, at which pore condensation in a cylindrical pore occurs and the radius r of the meniscus of the condensed liquid.

$$\ln\left(\frac{p}{p_0}\right) = -\frac{2\gamma V_m \cos\varphi}{rRT} \tag{5}$$

With γ as the surface tension of the bulk fluid, V_m as the ideal gas volume, φ the wetting angle, R the ideal gas constant, and T the temperature. This method is restricted to cylindrical pores with a diameter above 2.5 nm and is not valid for narrow mesopores. Other methods like the semi-empirical Dubinin-Radushkevich or Horvath-Kawazoe method for the determination of the micropore size and distribution were developed. However, these methods are not applicable when also mesopores are present. Another method is the t-plot method. Within this method, the adsorbed volume is plotted as a function of the film thickness, and every deviation from the point of origin is ascribed to the presence of micropores. The α_a-method further extends this method by a nonporous reference. The most recent model is the density functional theory (DFT). It is suitable for the determination of micro- and mesoporous materials and to overcome the limitations of the BJH method.

It is important to highlight here, that all gas sorption results are derived from idealized theoretical models and the obtained values might contain errors. The theories are based on carbon materials, which should draw attention when applying the models to the materials in the present thesis containing oxygen. Before all physisorption experiments, the samples were degassed at 150 °C for 20 hours under a high vacuum. Nitrogen physisorption experiments were performed at 77 K on a Quadrasorb apparatus (Quantachrome Instruments). The surface area was determined by using multipoint BET model in the relative pressure below 0.2 using the Rouquerol criteria. The values were obtained after applying the method in the linear region with the best correlation.

CO_2 physisorption

As described earlier, nitrogen sorption is suitable for micro-, meso-, and macropore analysis but has limitations in the analysis of narrow micropores due to kinetic restrictions and diffusion issues. Using CO_2 as a test gas can be a useful alternative for micropore analysis. Firstly, due to the relatively high absolute temperatures and pressures compared with nitrogen and argon adsorption at cryogenic temperature (77 and 87 K), CO_2 can more easily access ultramicropores at 273 K. Secondly, the kinetic diameter of CO_2 is 0.33 nm, smaller than that of N_2 (0.36 nm) and argon (0.34 nm). Because of the enhanced kinetics, utilizing CO_2 adsorption experiments at 273 K allows one to perform a micropore size characterization (pore width < 1 nm) in a few hours, much faster than adsorption experiments at cryogenic temperatures. However, CO_2 has a quadrupole moment and interacts with polar functionalities. In the case of pure carbon materials, this is usually no issue. However, for materials containing a high amount of nitrogen or oxygen, the existing models cannot be applied. Still, the isotherms can give useful information about the micropores and polarity of the materials.

The strength of the adsorbate-adsorbent interactions can be expressed by the heat of adsorption (Q_{st}), which is obtained by CO_2 sorption measurements at two different temperatures (usually 273 K and 298 K) and applying the Clausius-Clapeyron equation (***Equation 6***) for a specific amount adsorbed.

$$\ln\frac{p_2}{p_1} = \frac{(T_2 - T_1)Q_{st}}{RT_1T_2} \tag{6}$$

With p for the pressure, T for temperature (*i.e.,* T_1=273 K, T_2=298 K), and R for the universal gas constant. When considering the material for gas sorption, also the selectivity to adsorb gas in common conditions, *i.e.*, CO_2 diluted in nitrogen (like in air), needs to be considered. The ideal adsorbed solution theory (IAST) is commonly used as a selectivity parameter. CO_2 and N_2 isotherms at 298 K are measured and the adsorbed amounts at specific pressures are used to calculate the $IAST_{CO2/N2}$ with ***Equation** 7*.

$$S_{IAST} = \frac{q_{CO2}/q_{N2}}{p_{CO2}/p_{N2}} \tag{7}$$

With q for the amount adsorbed at pressure (p). To imitate a more realistic situation the commonly used pressure for N_2 is 0.85 kPa and for CO_2 15 kPa. As the name already implies this method is also based on idealization and the assumptions are, that the solution is ideal and in equilibrium with the gas phase. CO_2 sorption experiments were performed on the Quadrasorb apparatus at 273 K and 298 K. Before measurement, samples were degassed at 150 °C for 20 h under vacuum.

Vapor adsorption

Water vapor sorption experiments can be used to obtain information on the hydrophilicity of the surface of materials. Due to the high dipole moment of water, it has strong interactions with high enthalpy with polar surfaces. Measurements were performed on a Quantachrome Autosorb IQ apparatus at 298 K. Before measurement, samples were degassed at 150 °C for 20 h under a vacuum.

Electron microscopy

Electron microscope measurements are based on the interaction between an electron beam and the sample in a high vacuum. The electrons are generated in an electron gun, accelerated by an electromagnetic field, and focused through a series of electromagnetic lenses onto the sample. When the electron beam hits the sample, different types of interactions occur (***Figure 6.2***). With the different electron microscope techniques, different interactions are important and detected.

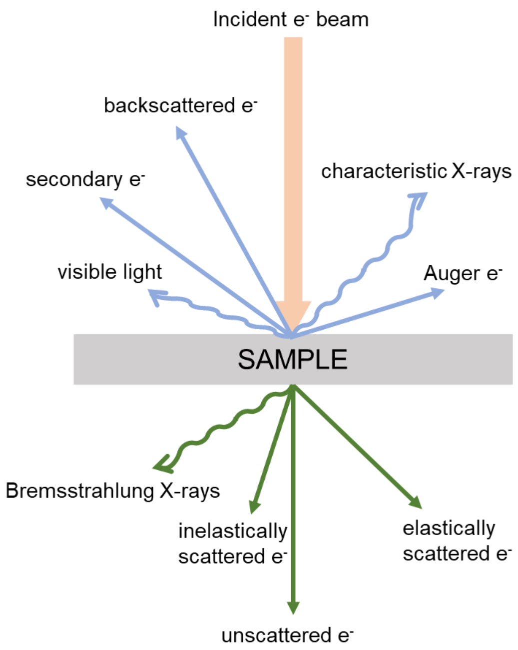

Figure 6.2. Different types of interactions between the electron beam and a sample.

Scanning electron microscopy (SEM)

In SEM measurements, secondary and backscattered electrons are detected for imaging. Secondary electrons are crucial for the analysis of the morphology and topography of the samples as they are emitted close to the surface and have low energy. Backscattered electrons, emitted from deeper regions of the sample, produce images where heavier atoms appear brighter. The data presented in this thesis was recorded on an LEO 1550-Gemini microscope operating at 3−20 kV. All samples were sputtered with an approximately 10 nm thick film of an 80% gold/20% palladium mixture to increase the conductivity of the surface.

Transmission electron microscopy (TEM)

In TEM measurements, electrons are transmitted through a very thin film (preferably < 100 nm) of the sample and detected. TEM and STEM modes of the microscope use different condenser lens settings: in TEM mode the illumination is parallel whereas in STEM mode the beam is finely focused and scans across the specimen. Aberration correctors improve the resolution, making HR-TEM or HR-STEM imaging at the atomic scale possible, which is crucial for studying materials with single atoms and nanoclusters to prove their presence. By processing HR-TEM images and applying FFT, one can learn about the local crystallographic structure of the materials at the atomic and nanoscale by choosing different areas of the sample during image processing. On the other hand, selected area electron diffraction (SAED) is obtained from large areas of the specimen and used for determining the average crystallographic structure of the materials.

Besides all the imaging capabilities, TEM is also an analytic technique. Energy-dispersive spectrometry (EDS) and EELS give qualitative and quantitative information about chemical elements present in the material. In EDS, characteristic X-rays are detected, and in EELS inelastically scattered electrons. EELS is also sensitive to different chemical bonding present in the structure. Before TEM and STEM observations, samples were sonicated in ethanol for 15 min and the obtained suspension was drop-casted to a Cu grid with lacey carbon support and dried for 15 min. Studies were performed using a double Cs corrected JEOL JEM-ARM200F (S)TEM operated at 80 kV and equipped with a cold-field emission gun and a high-angle silicon drift.

Cycle voltammetry (CV)

The electrode reaction kinetics were studied *via* CV measurements, utilizing the relationship between peak current density (i) and scan rate (v) following this equation:

$$i = a \cdot v^{b} \tag{8}$$

where a and b are constants. For analytical purposes, it can be transformed into

$$\log(i) = b\log(v) + \log(a) \tag{9}$$

where b is the slope of $\log(i)$ *vs.* $\log(v)$ curve. A b value close to 0.5 suggests a dominant diffusion process, while b proximity to 1 indicates a rapid capacitive response. Peaks C1, A1, and A2 were chosen as the key indicators for kinetic analyses of the Zn-ion capacitor. Further, the capacitive contribution is quantified by separating the current (i) at a fixed potential (V) into capacitive effect (k_1v) and diffusion-controlled processes ($k_2v^{0.5}$), according to the below equation:

$$i = k_1v + k_2v^{0.5} \tag{10}$$

which can be rearranged as

$$i/v^{0.5} = k_1v^{0.5} + k_2 \tag{11}$$

where i, k_1v, and $k_2v^{0.5}$ denote the current response, capacitive contribution, and ionic diffusion contribution, respectively. The k_1 value can be obtained by fitting $i/v^{0.5}$ *vs.* $v^{0.5}$ plots.

Electrochemical tests were performed using the Biologic MPG-2 Galvanostatic/potentiostat at room temperature (20−30 ºC).

Galvanostatic intermittent titration technique (GITT)

The diffusion kinetics of ions within the carbonaceous materials were analyzed by the Galvanostatic intermittent titration technique (GITT). GITT measurement was carried out at a current density of 1 $A \cdot g^{-1}$ with a constant current pulse of 10 min and an open-circuit relaxation for 3 h. The diffusion coefficients are calculated at each step according to the following equation:

$$D_{ion} = \frac{4}{\pi t}\left(\frac{m_B V_m}{M_B S}\right)^2 \left(\frac{\Delta E_s}{\Delta E_t}\right)^2 \tag{12}$$

where t is the duration of current pulse (s), m_B is the mass loading ($mg \cdot cm^{-2}$), M_B is the molar mass, V_m is the molar volume, and S is the electrolyte-electrode contact area (cm^2). ΔE_s is the quasi-thermodynamic equilibrium potential difference before and after the current pulse (V), while ΔE_t is the potential difference (V) during a charge/discharge current pulse after eliminating the internal resistance drop. $L = (\frac{m_B V_m}{M_B S})$ is the ion diffusion length (cm). For compact electrodes in this case, it can be considered as the thickness of the electrode measured by the spiral micrometer.

Electrochemical quartz crystal microbalance (EQCM)

For sample preparation of EQCM, Bio-Logic 1 in. diameter Au-coated quartz crystals (oscillating frequency f_0, 9 MHz) were spraying coated by a spray gun with a suspension containing 90 wt% of active material (UC1:5 or UC1:50) and 10 wt% of carboxymethyl cellulose binder in deionized water (1 $mg \cdot mL^{-1}$). The mass loading of active material was around 20−30 $ng \cdot cm^{-2}$. The coated quartz was dried in a vacuum oven at 80 ºC overnight before use. The coated quartz crystal was used as the working electrode in a 3-electrode cell (PTFE holder), together with a SCE reference electrode, and a polished Zn foil as a counter electrode in 2 M $ZnSO_4$ electrolyte. EQCM measurements were carried out using a Maxtek RQCM system combined with Autolab PGSTAT101. For the EQCM results, the electrode mass change was calculated based on the Sauerbrey equation

$$\Delta m = -C_f \times \Delta f \tag{13}$$

where Δm ($g \cdot cm^{-2}$) is the mass change of coated quartz, C_f is the sensitivity factor of the crystal ($ng \cdot cm^{-2} \cdot Hz^{-1}$), and Δf is the quartz resonance frequency (Hz). In this experiment, C_f was 6.98

$ng\cdot cm^{-2}\cdot Hz^{-1}$ (the area of the Au crystal electrode: 1.27 cm^2). Blank experiments were performed using pristine Au-coated quartz in the same set-up. For consistent results, several cycles were run before starting EQCM measurements, to obtain stable reproducible electrochemical signals. By plotting the electrode weight change during polarization *vs.* charge (Q), the molar weight of adsorbed/desorbed species can be calculated according to Faraday's law in Equation, assuming a 100% faradic efficiency: $\Delta m/\Delta Q=M/nF$, where ΔQ is the charge passed through the electrode in coulomb, M is the molar weight of the adsorbed/desorbed ions, F is the Faraday constant (96485 $C\cdot mol^{-1}$), and n is the valence number of the ion.

6.3 Experimental section

6.3.1 List of used chemicals

Table 6.2. List of used chemicals in this thesis.

Chemicals	Chemical formula	Supplier	Purity grade
cesium acetate	CsAc	Thermo Scientific	99.5%, for analysis
potassium acetate	KAc	Alfa Aesar	99%
sodium acetate	NaAc	Alfa Aesar	99%
lithium acetate	LiAc	Alfa Aesar	99%
maleic acid	$C_4H_4O_4$	Thermo Scientific	99.5%, for synthesis
uric acid	$C_5H_4N_4O_3$	Roth	≥ 99%
fumaric acid	$C_4H_4O_4$	Acros organics	≥ 99%
succinic acid	$C_4H_6O_4$	Sigma Aldrich	≥ 99.0%
acrylic acid	$C_3H_4O_2$	Sigma Aldrich	≥ 99%
cesium carbonate	Cs_2CO_3	Thermo Scientific	99.5%, for analysis
potassium carbonate	K_2CO_3	Thermo Scientific	99.5%
sodium carbonate	Na_2CO_3	SERVA	99%
lithium carbonate	Li_2CO_3	Alfa Aesar	99.0%
hydrochloric acid	HCl	Merck	37%
sulfuric acid	H_2SO_4	Roth	98%
polytetrafluoroethylene	PTFE	Sigma-Aldrich	60 wt% dispersion in H_2O
zinc sulfate heptahydrate	$ZnSO_4\cdot 7H_2O$	Sigma-Aldrich	ACS reagent, 99%
cesium hydroxide monohydrate	$CsOH\cdot H_2O$	Thermo Scientific	99.5%, for analysis

6.3.2 Materials synthesis

CsAc-derived porous carbons. In a typical synthesis, 10 g CsAc was placed in a nickel crucible with a lid, transferred to a Muffle furnace, and heated at 400/450/500/600/700/800 °C for 2 h (heating ramp: 1 $°C\cdot min^{-1}$) in N_2 atmosphere (flowing rate: 3.5 sccm), and naturally cooled down to 30 ºC. The carbonized products were then ground and transferred to 1 M HCl (300 mL), stirred with a magnet overnight, and filtered by a Bucher funnel. The above procedures were repeated two times. The collected powders were then rinsed with deionized water and dried at 60 ºC for 3 h. For control experiments, KAc, NaAc, LiAc, and $Zn(Ac)_2$ were calcined, washed, and dried in the same way. The yields of carbons are calculated by dividing the mass of carbons by the mass of acetate.

Cesium maleate-derived porous carbons. Cesium maleates (Cs_2MA and Cs_1MA) were synthesized by mixing $CsOH·H_2O$ and MA in a molar ratio of 2:1 or 1:1 in deionized water. The aqueous solutions were then subjected to slow evaporation at 60 ºC to obtain the crystals. Similarly, K_2MA was synthesized using KOH and MA. Cs_2MA, Cs_1MA, or K_2MA was directly used as a self-templating precursor, ground in an agate molar, transferred to a nickel crucible with a lid, heated at 800 °C for 2 h (heating ramp: 1 $°C·min^{-1}$) under N_2 atmosphere (flow rate: 3.5 sccm) in a muffle oven, and then naturally cooled down to room temperature (20−30 ºC). The resulting condensed products were washed twice with 1 M hydrochloric acid aqueous solution, rinsed with deionized water, and dried at 60 ºC in an oven for 4 h to obtain the condensed products. For the typical carbon synthesis from molecular precursors, 1 g of MA and 10 g of Cs_2CO_3 were mixed, ground, and transferred to a nickel crucible as the starting materials. Fumaric, succinic, or acrylic acids were also used as molecular precursors. K_2CO_3, Na_2CO_3, Li_2CO_3, or CsCl were also used as replacements for Cs_2CO_3 following the same procedures. The products obtained from MA and various alkali carbonates were labeled as MX-T, X represents the first letter of alkali metal and T represents the synthesis temperature. The carbon yields were calculated by dividing the mass of collected samples (after washing and completely drying) by the mass of organic parts in self-templating precursors or the mass of molecular precursors.

Hierarchical porous carbons derived from CsAc and uric acid. UA and CsAc at mass ratios of 1:5 (2 and 10 g) or 1:50 (0.2 and 10 g) were mixed and ground together in a mortar. The mixture was then transferred to a nickel crucible, thermally treated at 800 ºC (heating rate: 1 $°C·min^{-1}$) for 2 hours under a N_2 atmosphere (flowing rate: 3.5 sccm), and naturally cooled down to 30 ºC. Then, the treated products were ground, washed twice using a 1 M hydrochloric acid solution, rinsed with deionized water, and finally dried in an oven at 60 ºC for 4 h. The products obtained from the 1:5 or 1:50 mass ratio mix of UA and CsAc were labeled as UC1:5 and UC1:50, respectively.

6.3.3 Electrode preparation and device assembly

Firstly, 40 mg of carbon powders were mixed with 5 mg of Super P conductive carbon black, and 50 µL of a 10 wt% polytetrafluoroethylene solution in 2 mL of ethanol. The mixture was sonicated for 2 hours to achieve a homogeneous dispersion. The resulting ink was then poured onto a glass plate, purged with air to accelerate ethanol evaporation, and mixed by two razor blades to obtain a rubber-like consistency. The consistency was dried in an oven at 60 °C overnight and subsequently rolled into a uniform thin sheet in a piece of aluminum foil by a roll mill, punched into free-standing disks (10 mm in diameter, 1.6 ± 0.2 mg·cm^{-2} in mass loading of active materials), and vacuum-dried overnight. For the 3-electrode Swagelok cell, a piece of carbon film was used as the working electrode, a Zn foil as the counter electrode, a saturated calomel electrode (SCE) as the reference electrode, 2 M $ZnSO_4$ in deionized water as the electrolyte, and a piece of glass fiber filter paper (Whatman GF/A) as the separator. For the 2-electrode Zn-ion capacitor assembly, a piece of carbon film was stacked with 2 pieces of glass fiber separators, incorporating 100 µL of 2 M $ZnSO_4$ as the electrolyte, and paired with a Zn foil in a stainless-steel coin cell (CR 2032). For the 2-electrode Zn-ion capacitor assembly, a piece of carbon film was stacked with 2 pieces of glass fiber separators, incorporating 100 µL of 2 M $ZnSO_4$ as the electrolyte, and paired with a Zn foil in a stainless-steel coin cell (CR 2032). Similarly, Na-ion capacitor was assembled by stacking a piece of electrode film, 2 pieces of separator (16 mm in diameter) with 100 µL 1 M sodium hexafluorophosphate ($NaPF_6$) in vinyl carbonate: dimethyl carbonate (50: 50 vol%) with 5 wt% fluoroethylene carbonate as electrolyte, and a Na metal (12 mm in diameter) in a 2032 coin-type cell. The supercapacitor was assembled by using two pieces of electrode films sandwiching a piece of glass fiber (12 mm in diameter) with 30 µL 1 M H_2SO_4 as electrolyte in a Swagelok cell.

6.3.4 Electrochemical measurements

Cyclic voltammetry, Galvanostatic charge-discharge, and electrochemical impedance spectroscopy were performed using a Biologic MPG-2 Galvanostatic/potentiostat at room temperature (25 °C). In the measurement of 2-electrode coin cells, a working voltage window of 0.2−1.8 V *vs.* Zn^{2+}/Zn was applied to prevent parasitic reactions such as water splitting. *In situ* electrochemical impedance spectroscopy tests were performed at different potentials with an AC voltage of 10 mV amplitude within a frequency range of 200 kHz to 10 mHz. Device-specific capacity (Q in $mAh \cdot g^{-1}$) and capacitance (C in $F \cdot g^{-1}$) were determined from Galvanostatic charge-discharge curves by the following equations:

$$Q = I \times \Delta t / m \tag{14}$$

$$C = Q/U = I\int V dt / 2(m \times \Delta V) \tag{15}$$

where I (A), Δt (s), $\int V dt$ ($V \cdot s$), m (g), and ΔV (V) are discharge current, discharge time, the integral area under charge/discharge curve, the mass of active material in each cathode, and discharge voltage change excluding the internal resistance drop, respectively. The specific energy ($Wh \cdot kg^{-1}$) and specific power ($W \cdot kg^{-1}$) of devices were calculated from the equations:

$$E_{Cell} = I\int V dt / 3.6m \tag{16}$$

$$P_{Cell} = E_{Cell} \times 3600 / \Delta t \tag{17}$$

6.4 List of publications and author contributions

Publications related to this thesis:

1. **J. Li**, J. Kossmann, K. Zeng, K. Zhang, B. Wang, C. Weinberger, M. Antonietti, M. Odziomek, N. López-Salas, When High-Temperature Cesium Chemistry Meets Self-Templating: Metal Acetates as Building Blocks of Unusual Highly Porous Carbons, *Angew. Chem. Int. Ed.* **2023**, *135*, e202217808;
2. **J. Li**, Y. Xu, P. Li, A. Völkel, F. Igoa Saldaña, M. Antonietti, N. López-Salas, M. Odziomek, Beyond Conventional Carbon Activation: Creating Porosity without Etching Using Cesium Effect, *Adv. Mater.* **2024**, 202311655;
3. **J. Li**, M. Antonietti, P. Simon, M. Odziomek, Controlled Synthesis of Porous Carbons to Unravel the Role of Pore Size on Zn-Ion Capacitors, Manuscript in preparation, **2024**;

Other publications during PhD study:

4. **J. Li**, M. Antonietti, M. Odziomek, Controlled Condensation of Ordered Carbon Structures at Low Temperatures *via* Cesium Effect, Manuscript in preparation, **2024**;
5. C. Mark Pelicano, **J. Li**, M. Cabrero-Antonino, V. Strauss, I. Silva, L. Peng, N. V. Tarakina, H. García, M. Antonietti, Rational Design of a Carbon/Potassium Poly(heptazine imide) Heterojunction for Enhanced Photocatalytic H_2 and H_2O_2 Evolution, *J. Mater. Chem. A*, **2024**, 12, 475.

Author contribution statement

For the research work presented in this thesis, Dr. Mateusz Odziomek, Dr. Nieves Lopez-Salas, and Prof. Markus Antonietti directed the projects, discussed the data, and revised the manuscripts. Jiaxin Li conceived the ideas, conducted the experiments, analyzed the data, and wrote the manuscripts. Dr. Yaolin Xu, Dr. Janina Kossmann, Prof. Patrice Simon, Dr. Fernando Igoa Saldaña, Prof. Ke Zeng, Prof. Philipp Adelhelm, Pengzhou Li, Kun Zhang, Antje Völkel, and Prof. Bingjie Wang provided support in materials synthesis, characterizations, mechanism analyses, and manuscript revision. All authors discussed the results and commented on the manuscripts. All the content in this thesis is not included in any doctoral thesis of anyone else.

6.5 List of presentations

1. Oral report: Cesium-Mediated Porous Carbon for Electrochemical Energy Storage, E-MRS 2023 Fall Meeting, Warsaw, Poland, 09.2023;
2. Poster: Cesium-Mediated Porous Carbon for Electrochemical Energy Storage, 7th International Conference on Multifunctional, Hybrid and Nanomaterial, Genoa, Italy, 10.2022;
3. Poster: Cesium-Mediated Porous Carbon for Na-ion and Zn-ion Capacitors, Sodium Battery Symposium (SBS 3), Berlin, Germany, 09.2022.

Acknowledgment

First of all, I would like to express my deepest appreciation to my senior supervisor, Prof. Dr. Markus Antonietti, for providing me with the precious opportunity to study and research at the Max-Planck Institute of Colloids and Interfaces. His generous scientific support and guidance on the direction of my research as well as his passion for scientific research have been enough to keep me motivated throughout my research. Besides, his humor and generosity, passion for life, have enriched my understanding of how an accomplished scientist can be. I have aspired to become a researcher like him who can strike a good work-life balance well.

My sincerest special acknowledgment goes to my supervisors Dr. Nieves López-Salas and Dr. Mateusz Odziomek. Nieves served as my first supervisor during my first year of Ph.D. before she moved to Paderborn University. Despite my lack of knowledge of porous carbons at the beginning, she explained to me everything with patience. Nieves gave me many cares about my academic and personal life and helped me to quickly adapt to an unfamiliar life in a foreign country. Mateusz became my second supervisor afterwards. His generosity, tolerance, patience, wisdom, and dedication to scientific research have provided me with endless encouragement and support throughout my research journey. Discussions with him have always been constructive and enjoyable, leaving me filled with knowledge and optimism after each scientific conversation. I feel that he seems to know all the basic principles of material synthesis, chemical reactions, and characterization techniques like a mobile Wiki, which inspires me to keep learning and being professional like him. Beyond scientific inspiration, he also guided me on various aspects of life.

I am also thankful to Prof. Philipp Adelhelm from Humboldt-Universität zu Berlin for accepting me as an associated Ph.D. student in his battery group. He is very responsible, enthusiastic, and friendly. He explained the detailed enrollment and graduation procedures with patience, invited me to his group meeting, academic conference, and Christmas party, connecting me with his group. I am fortunate to have them as my supervisors and sincerely express my infinite gratitude for their support. They will serve as permanent role models in my future life.

I am also grateful to Prof. Patrice Simon for providing me with the valuable opportunity to study in his group as a visiting student. Actually, I know his name six years ago when I started my bachelor thesis on microcapacitors. Back then, I could never have imagined having the opportunity to work in his group and engage in face-to-face discussions with him. I am impressed by his solid knowledge on electrochemistry.

I would like to thank all the collaborators. Without their assistance in experiments and discussions, I would never have completed my research. Special thanks to Janina for being a perfect mentor and role model during the first year of my Ph.D. She is quite efficient, organized, and intelligent. She not only taught me to synthesize materials, operate instruments, and analyze data, but also shared many soft skills like making plans, summaries, and presentations. I also thank Prof. Ke Zeng for teaching me about polymers and carbon materials, Dr. Yaolin Xu from Helmholtz-Zentrum Berlin für Materialien und Energie for kind help on XRD experiments and paper revisions, my dear friends Pengzhou and Kun from Fudan University for XPS, NMR, and TEM, and my kind office neighbor Zihan for solid technique support. Special thanks to Changjiang, Moritz, Hui, and Yanan from Philipp group for their kind and friendly support. I also appreciate Kangkang, Liyuan, and Jero from the Patrice group for their assistance.

I am profoundly thankful to Jessica for helping me order and measure ICP, Antje Völkel for TGA-MS and ECA measurements, Katharina for gas sorption measurements, Dr. Nadezda V. Tarakina, Dr. Hannes Zschiesche, Bolortuya Badamdorj, and Heike Runge for SEM and TEM measurements. I would also like to thank all the colleagues at MPIKG (Sol, Ibrahim, Enrico, Janina, Chun, Xinyue, Mahima, Orestis, Rémi, Zeen, Roza, Sasha, Christian, Yang, Gaofeng, Jun, and many others). I am truly grateful for the cherished memories with them, especially many talks, and parties at Chez Briel, coffee corners, and canteen. I would like to thank my committee members, paper reviewers, and the readers/audience at my poster or oral presentations during conferences. Your valuable problems, suggestions, and advice have played a crucial role in enhancing the quality of my projects.

Besides, I extend my gratitude to the friends I met in Europe through activities such as hiking, badminton, concerts, talk shows, and photography (Kun, Ye, Zhuqing, Yiyang, and many others). Thank you all for enriching my life beyond academic life. The memories we created together during Tour du Mont Blanc, Kungsleden, many walks around Berlin, and more, will remain cherished. I also found endless joy in playing badminton at TU Berlin. Lastly, my deep gratitude goes to my family for giving me the warmest support throughout my study in Germany.

Erklärung zur selbstständigen Arbeit

Die vorliegende Arbeit wurde im Zeitraum zwischen September 2021 und März 2024 am Max-Planck-Institut für Kolloid- und Grenzflächenforschung unter der Leitung von Prof. Dr. Dr. h.c. durchgeführt. Markus Antonietti.

Ich erkläre, dass ich die Dissertation selbstständig und nur mit den angegebenen Hilfsmitteln angefertigt habe. Ich habe mich nicht anderweitig um einen Doktorgrad im Promotionsfach beworben und verfüge nicht über einen entsprechenden Doktorgrad. Die Promotionsordnung der Mathematisch-Naturwissenschaftlichen Fakultät, veröffentlicht im Amtsblatt der Humboldt-Universität zu Berlin Nr. 42/2018 vom 11.07.2018, habe ich zur Kenntnis genommen.

Declaration of independent work

The present work was carried out during the period between September 2021 and March 2024 at the Max Planck Institute of Colloids and Interfaces under the supervision of Prof. Dr. Dr. h.c. Markus Antonietti.

I declare that I have completed the thesis independently using only the aids and tools specified. I have not applied for a doctor’s degree in the doctoral subject elsewhere and do not hold a corresponding doctor’s degree. I have taken due note of the Faculty of Mathematics and Natural Sciences Ph.D. Regulations, published in the Official Gazette of Humboldt-Universität zu Berlin no. 42/2018 on 11/07/2018.

Jiaxin Li

Golm-Potsdam 08.04.2024